COMPACT, DIVERSE AND EFFICIENT: GLOBULAR CLUSTER BINARIES AND GRAVITATIONAL WAVE PARAMETER ESTIMATION CHALLENGES

CARL-JOHAN OLOF HASTER

A thesis submitted to the
University of Birmingham
for the degree of
DOCTOR OF PHILOSOPHY

Astrophysics and Space Research
School of Physics and Astronomy
College of Engineering and Physical Sciences
University of Birmingham
April 2016

Acknowledgements

It is my sincere pleasure to thank the following people: Min bror Erik, mamma Kerstin och pappa Lars-Olof, utan ert stöd och hjälp hade jag aldrig vågat tro att detta hade varit möjligt. My supervisors Ilya Mandel and Alberto Vecchio for their mentorship, support and endless patience; Christopher Berry, Walter Del Pozzo, Will Farr, John Veitch, Alberto Sesana and David Stops for providing both interesting discussions and answers to my many questions. Fabio Antonini, Katie Breivik , Sourav Chatterjee, Ben Farr, Vicky Kalogera, Tyson Littenberg, Fred Rasio and Carl Rodriguez for making my months in Chicago both fun, interesting and memorable. All my friends in the ASR group at Birmingham, especially Jim Barrett, Charlotte Bond, Daniel Brown, Mark Burke, Chris Collins, Sam Cooper, Sebastian Gaebel, Anna Green, Kat Grover, Maggie Lieu, Hannah Middleton, Chiara Mingarelli, Sarah Mulroy, Trevor Sidery, Rory Smith, Simon Stevenson, Daniel Töyrä, Alejandro Vigna-Gómez and Serena Vinciguerra for years of fun and adventures; The members of the CBC group, and specifically the Parameter Estimation subgroup, for all their help. I would also like to thank Alberto Sesana and Jonathan Gair for their great skill and patience as the examiners for my PhD viva.

Several of the chapters in this thesis were the result of collaborations and benefited from discussions with several people. Chapter 2 was based on work done in collaboration with Fabio Antonini, Ilya Mandel and Vicky Kalogera [108], and benefited from discussions with Sourav Chatterjee, Jonathan Gair, James Guillochon, Fred Rasio and Alberto Sesana. Chapter 3 was based on work done in collaboration with Zhilu Wang, Christopher Berry, Simon Stevenson, John Veitch and Ilya Mandel [110] and benefited from discussions with Michael Pürrer, Tom Callister and Tom Dent. Chapter 4 was based on work done in collaboration

with Ilya Mandel and Will M. Farr [109], and benefited from discussions with Christopher Berry, Walter Del Pozzo, Alberto Vecchio, John Veitch, Richard O'Shaughnessy and Chris Pankow.

My work has been supported by a studentship from the University of Birmingham and the Center for Interdisciplinary Exploration in Astrophysics at Northwestern University.

Abstract

Following the first detection of gravitational waves from a binary coalescence the study of the formation and evolution of these gravitational-wave sources and the recovery and analysis of any detected event will be crucial for the newly realised field of observational gravitational wave astrophysics.

This thesis covers a wide range of these topics including simulating the dense environments where compact binaries are likely to form, focusing on binaries containing an intermediate mass black hole (IMBH). It is shown that such binaries do form, are able to merge within a ~ 100 Myr simulation, and that the careful treatment of the orbital evolution (including post-Newtonian effects) implemented here was crucial for correctly describing the binary evolution. The later part of the thesis covers the analysis of the gravitational waves emitted by such a binary, and shows it is possible to identify the IMBH with high confidence, together with most other parameters of the binary, despite the short-duration signals and assumed uncertainties in the available waveform models. Finally a method for rapid parameter estimation of gravitational wave sources is presented and shown to recover source parameters with comparable accuracy using only a small fraction $\sim 0.1\%$ of the computational resources required by conventional methods.

Contents

List of Figures

Chapter 1

Introduction

The scientific field of observational gravitational wave astrophysics was, a century after the initial theoretical predictions [82, 83], initiated by the observation of the coalescence of a system of binary black holes named GW150914 [22]. Although there were indirect observational evidence of emission of gravitational waves from the orbital evolution of binary pulsar systems [119, 251, 130], GW150914 was the first direct probe into the dark realm of strong-field gravitational physics. This observation had not been possible without the design, construction and commissioning of the laser interferometer detectors of Advanced LIGO [aLIGO; 13] which performed their first observational run, O1, between September 12, 2015 and January 19, 2016. Together with the future detectors of Advanced Virgo [AdV; 27], KAGRA [221] and LIGO India [122], aLIGO will form a global network of gravitational wave observatories operating in the Hz to kHz frequency range, sensitive to some of the most energetic events in the universe. One of the primary sources for gravitational waves detectable by such a network are the coalescences of compact objects in binary systems (CBCs). This includes binaries containing either only neutron stars (BNS), black holes (BBH) or a combination (NSBH).

1.1 Formation and evolution of compact binaries

Previous observations of compact objects have been done in the electromagnetic spectrum, e.g. both black holes and neutron stars as members of x-ray binaries [141] and neutron stars also as radio pulsars [143]. These observations have been used to inform models for estimated coalescence rates, which can then be converted into predictions of rates of detected events in aLIGO. Even after the observation of GW150914 the estimated rates of BBH coalescences is uncertain [$2-400\mathrm{Gpc}^{-3}\mathrm{yr}^{-1}$ from 23], and the non-detection of NSBH or BNS systems *so far* in aLIGO leaves the estimated rates at their pre-O1 state [$0.6 - 1000\,\mathrm{Gpc}^{-3}\mathrm{yr}^{-1}$ and $10 - 10^4\ \mathrm{Gpc}^{-3}\mathrm{yr}^{-1}$ respectively, from 17], these estimations are however expected to change after the final search results from O1 have been published.

An interesting feature among the observed compact objects are that there appears to be a "mass gap" between the heaviest observed neutron star [at just above $2M_\odot$, see 133] and the lightest black hole [at $\sim 4 - 5.5M_\odot$, 179, 85, depending on the assumed mass distibution]. There are however arguments for whether the gap is physical [48, and indicative of specifics within supernova engines] or caused by observational selection effects [131]. While future observations of gravitational waves from CBCs with components near or inside the mass gap will give the final verdict on its existence, they will also provide information about the underlying formation and evolution of compact objects [154, 140].

1.1.1 Binary formation from stellar evolution in the galactic field

It has been observed that a majority of stars massive enough to form compact objects are found in binary systems [205, 127]. These observations, combined with models for stellar evolution (both of the individual stars and their binary interactions [124, 244, 191, and see Figure 1.1]), can then be used for large scale simulations of realistic populations of compact binary systems [46, 44, 76–78, 222, 47] [and see 45, for the implications specific to the formation of GW150914]. In addition to the "conventional" BBH formation paths for stellar binaries in a galactic

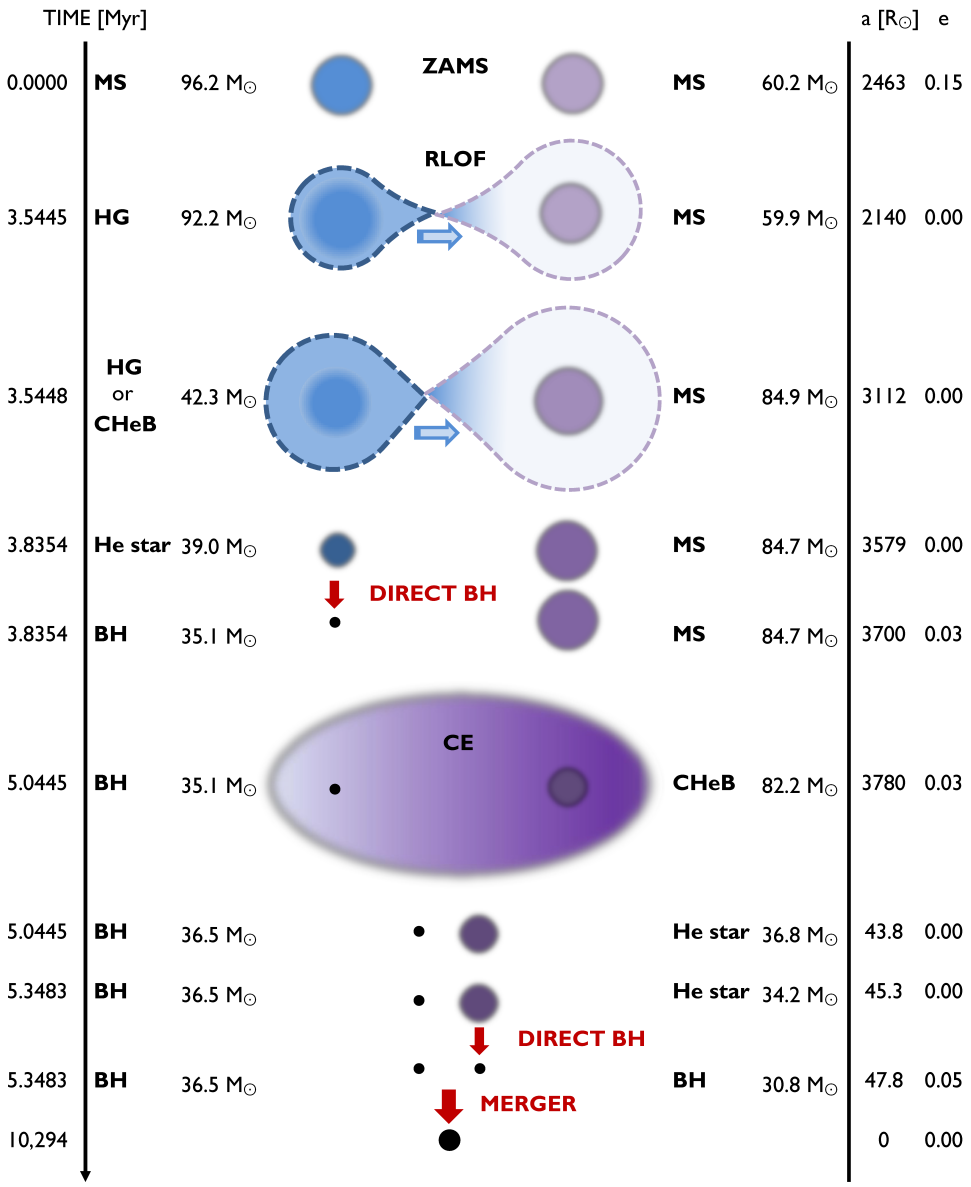

Figure 1.1 After the formation of a binary containing two massive stars, the pair experiences stable mass transfer through the overflow of the Roche lobe for the system. The initially most massive star undergoes core-collapse into a black hole after which an additional mass transfer phase forms a common envelope that, through dynamical friction, hardens the binary further. After the second star forms a black hole, through another core-collapse, the orbital evolution of the binary becomes dominated by emission of gravitational waves which leads to an inspiral and a subsequent merger. Figure reproduced from [45]

field population described in Figure 1.1 recent studies have suggested another formation method. There the helium formed in the stellar core is homogeneously mixed throughout the star, through its rapid rotation, keeping the star compact throughout its lifetime. This formation channel could therefore more easily give rise to more massive black holes than the "normal evolution" path [152, 75, 157, and see Figure 1.2].

1.1.2 Dynamical binary formation in dense stellar environments

Where the formation of binary compact objects through stellar evolution in the galactic field is found to be highly dependant on the specific modelling of the binary interactions of the evolving stars, it is also possible to produce CBCs in dense stellar environments, such as globular clusters, where the formation is dominated by the much more clearly understood gravitational dynamics, an example is shown in Figure 1.3. Simulations which include both a treatment of stellar evolution and a realistic description (size, mass and number of particles) of globular clusters have primarily been performed using Monte Carlo methods [79, 80, 171, 170, 202, 198, 67] but comparisons against more computationally intensive direct N-body simulations have shown excellent agreement [203] [and see 200, for the implications specific to the formation of GW150914].

1.2 Gravitational wave sources

1.2.1 General relativity

Gravitational waves, labelled here as h, can be regarded as a small time-varying perturbation on the flat Minkowskian metric, η, to give a total metric g with components, for spacetime coordinates μ, ν, given as

$$g_{\mu,\nu} = h_{\mu,\nu} + \eta_{\mu,\nu} \tag{1.1}$$

which is observed as a dimensionless transverse strain in the local spacetime. This strain h is to leading order determined by the second time derivative of the

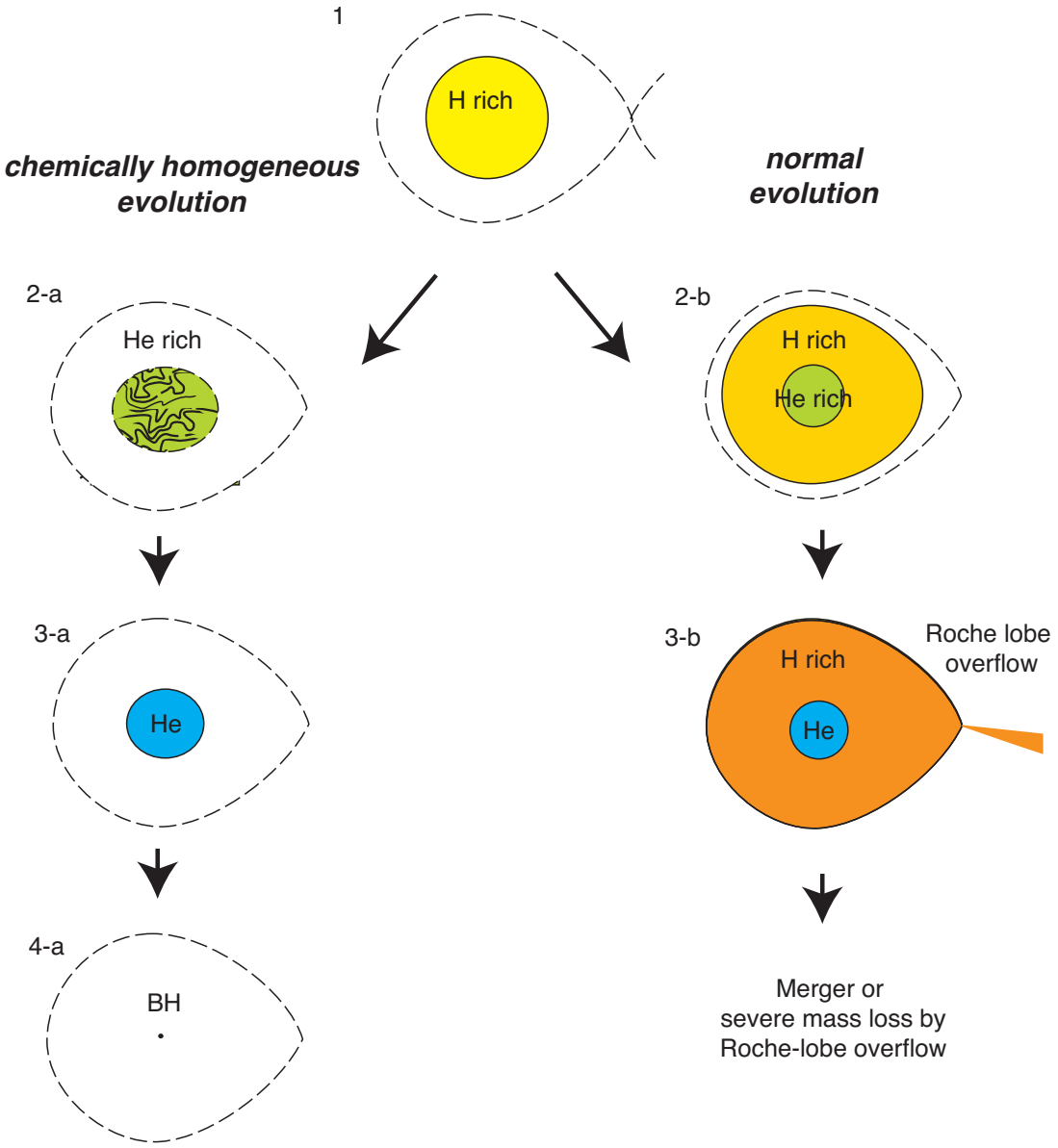

Figure 1.2 Comparing the "normal evolution" for a massive star (as also shown in Figure 1.1) against chemically homogeneous evolution where rapid stellar rotation and tidal effects induces mixing of the helium in the core into the entire star. This suppresses stellar expansion, and thus Roche overflow and mass transfer, leading to the possible formation of more massive black holes compared to in "normal evolution". Figure reproduced from [152]

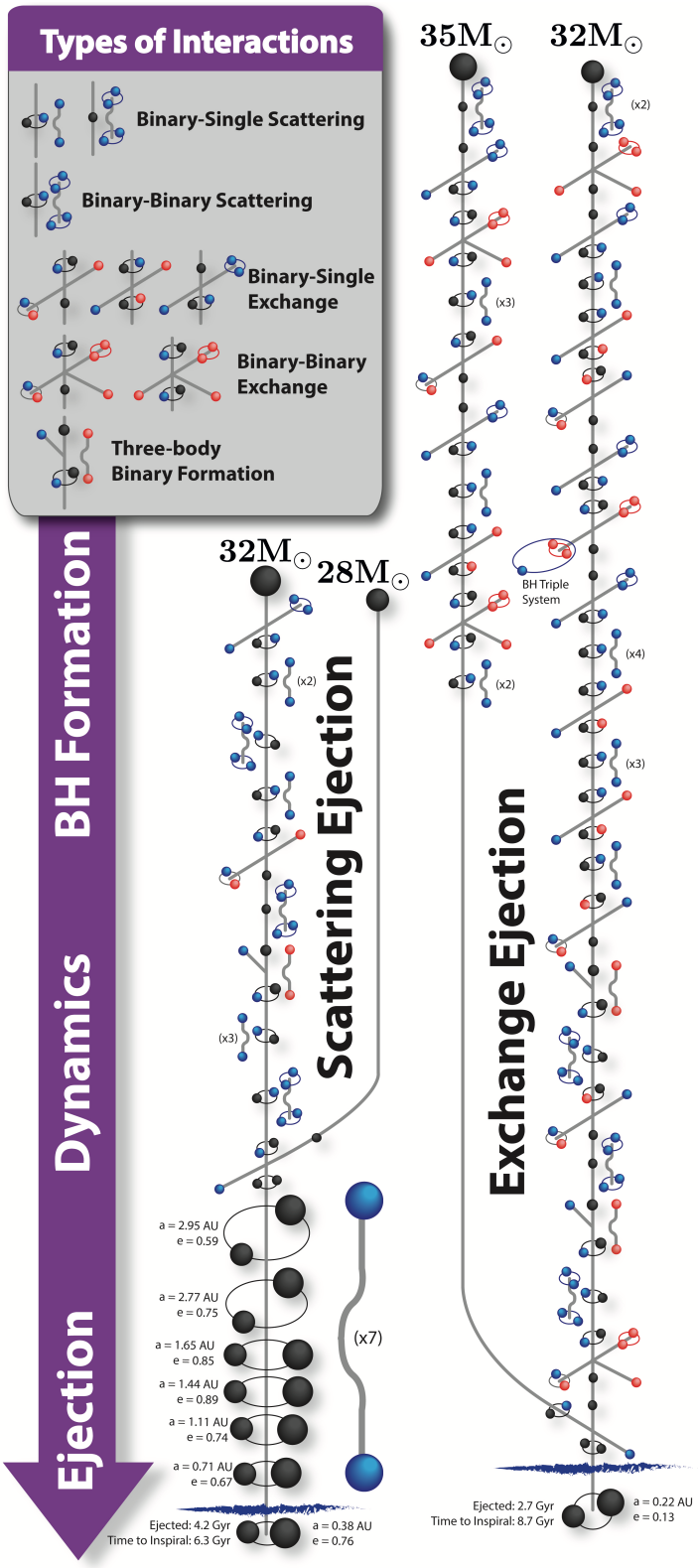

Figure 1.3 Showing two examples of dynamical formation of two binary black hole systems, including all scattering and exchange events with both single and other binary objects. Figure reproduced from [200]

mass quadrupole moment Q of a gravitational wave source (monopole and dipole radiation are, in general relativity, forbidden by conservation of energy and linear momentum respectively) as given by [210]

$$h \simeq -\frac{G}{2c^4}\left(\ddot{Q}_{ij} - \frac{1}{3}\delta_{ij}\ddot{Q}_{kk}\right)\frac{n_i n_j}{r} \tag{1.2}$$

where i, j, k are the three spatial coordinates, $\vec{n}$ a unit vector pointing along the line of sight, r is the distance to the source and dots represent derivatives with respect to time. At leading order, the luminosity from a source emitting gravitational waves, defined as an accelerated asymmetric mass distribution, is

$$L = \frac{1}{5}\left\langle \dddot{Q}_{jk}\dddot{Q}_{jk}\right\rangle , \tag{1.3}$$

where the angle brackets denote a time average over several wavelengths. For a source with characteristic mass, size, timescale and velocity M, R, T and v respectively Equation 1.3 can be simplified to

$$L \sim \frac{1}{5}\dddot{Q}^2 \sim \frac{1}{5}\left(\frac{MR^2}{T^3}\right)^2 \sim \frac{1}{5}\left(\frac{Mv^3}{R}\right)^2 . \tag{1.4}$$

or in terms of its Schwartzchild radius $R_s = 2GM/c^2$,

$$L \sim \frac{L_P}{20}\left(\frac{R_s}{R}\right)^2\left(\frac{v}{c}\right)^6 , \tag{1.5}$$

which further shows that gravitational waves will be most efficient for compact ($R \sim R_s$) and relativistic ($v \sim c$) objects. The constant L_P in Equation 1.5 is the Planck luminosity

$$L_P = \frac{c^5}{G} = 3.6 \times 10^{52}\ W , \tag{1.6}$$

which is the maximum luminosity possible under general relativity, corresponding to all mass-energy in an object, Mc^2, being released in an instant and leaving in a light-travel time R/c. As an example, GW150914 had a peak luminosity of $\sim 10^{-3} \times L_P$ which is brighter then the combined luminosity in the visible band from all electromagnetic sources in the Universe [22].

As shown in Equation 1.2, h depends only on the transverse components of the

trace-free $\ddot{Q}$ resulting in gravitational waves, as given by general relativity, only consisting of the transverse polarisations (a) and (b) from Figure 1.4. One of the other distinctions between observations of gravitational waves and other forms of astronomy is that gravitational waves are observed as amplitude variations, as opposed to power fluctuations. These amplitudes, as indicated in Figure 1.4, will induce periodic variations in the distance between objects where the maximum difference occurs for mutually perpendicular directions. In order to most effectively measure this differential length most modern gravitational wave detectors have implemented a laser Michelson interferometer, an example of which is shown in Figure 1.5. The dominating scale for a source which emits gravitational waves is set by the dimensionless orbital velocity $\nu \equiv v_{\rm orb}/c = GM_{\rm tot}f_{\rm gw}/c^3$. This leads to a fundamental degeneracy between total mass $M_{\rm tot}$ and $f_{\rm gw}$ making shifts in mass indistinguishable from redshifts of the $f_{\rm gw}$ (e.g. from cosmology) [117], this is discussed further in subsection 3.3.1. As the amplitude of h has a $1/r$ scaling (from Equation 1.2), this means that a gravitational wave inherently contains distance information but leaving the redshift as a model dependent free parameter.

1.2.2 Modelling compact binary coalescenses

The coalescence of a compact binary is a unique probe into strong field gravitation allowing unprecedented tests of general relativity [233]. The stringent framework provided by general relativity allows for the construction of accurate and verifiable models for the emitted gravitational waves from a compact binary coalescence.

1.2.2.1 Inspiral

During the initial phase of the coalescence the binary components are inspiraling in an orbit around their common center of mass. In this phase it is possible to represent the emitted gravitational wave amplitude to leading order as

$$\begin{aligned} h_0^{\rm inspiral} =& \frac{4\eta M_{\rm tot} G}{rc^2}\nu^2 \\ \approx& 10^{-23}\,\frac{1{\rm Mpc}}{r}\,\left(\frac{\mathcal{M}_c}{M_\odot}\right)^{5/3}\,\omega^{2/3} \end{aligned} \tag{1.7}$$

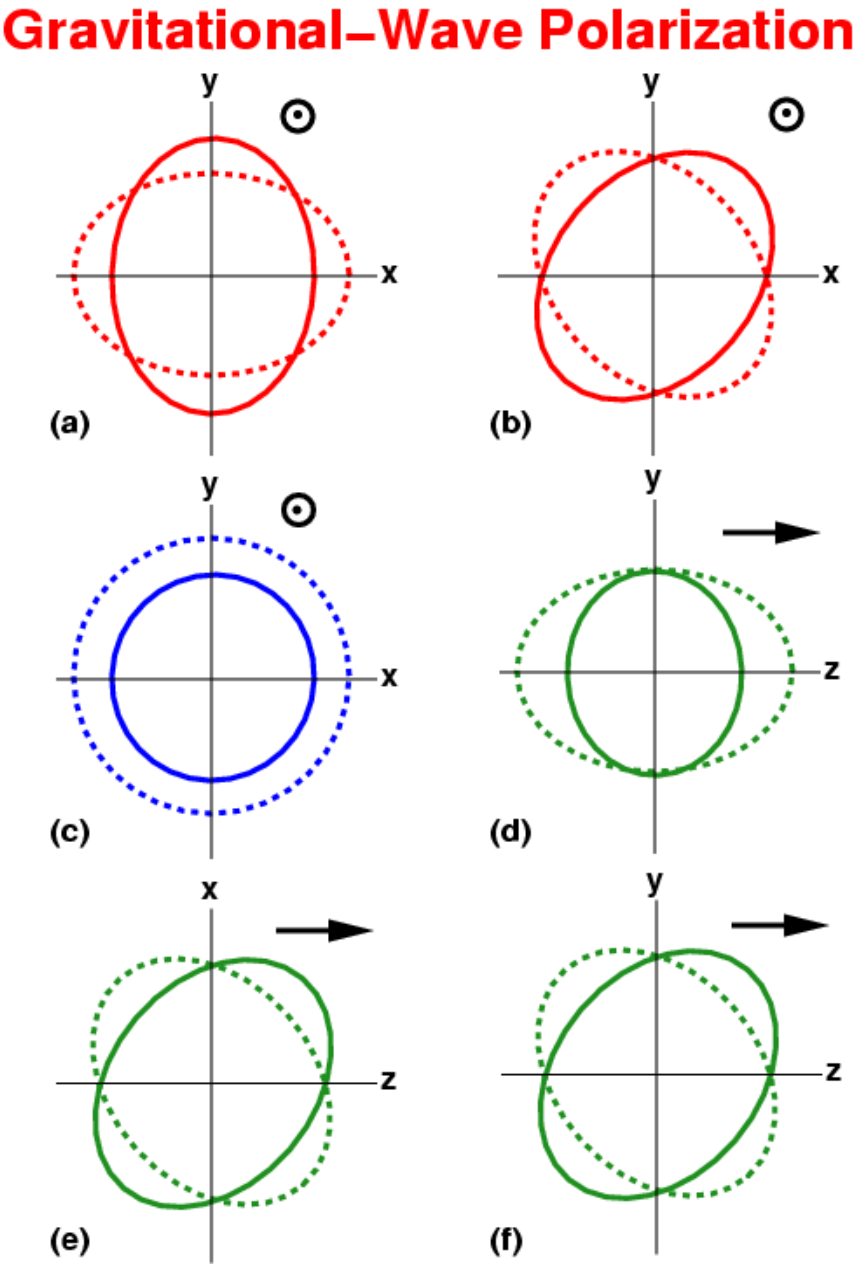

Figure 1.4 The six polarisation modes allowed in any metric theory of gravity for waves travelling in the $+z$ direction. The ellipses shown represent the displacement of each mode on a ring of test particles. In general relativity only the transverse (a) and (b), plus and cross respectively, are allowed. For massless scalar–tensor theories of gravity (c), the transverse breathing mode, can be present and for massive scalar–tensor theories the longitudinal mode (d) can also be included (but suppressed relative to (c) by a factor (λ/λ_C) where λ is the wavelegth of the gravitational radiation and λ_C is the Compton wavelength of the massive scalar). Finally, more general metric theories can also include the additional longitudinal vector modes (e) and (f). Figure reproduced from [253].

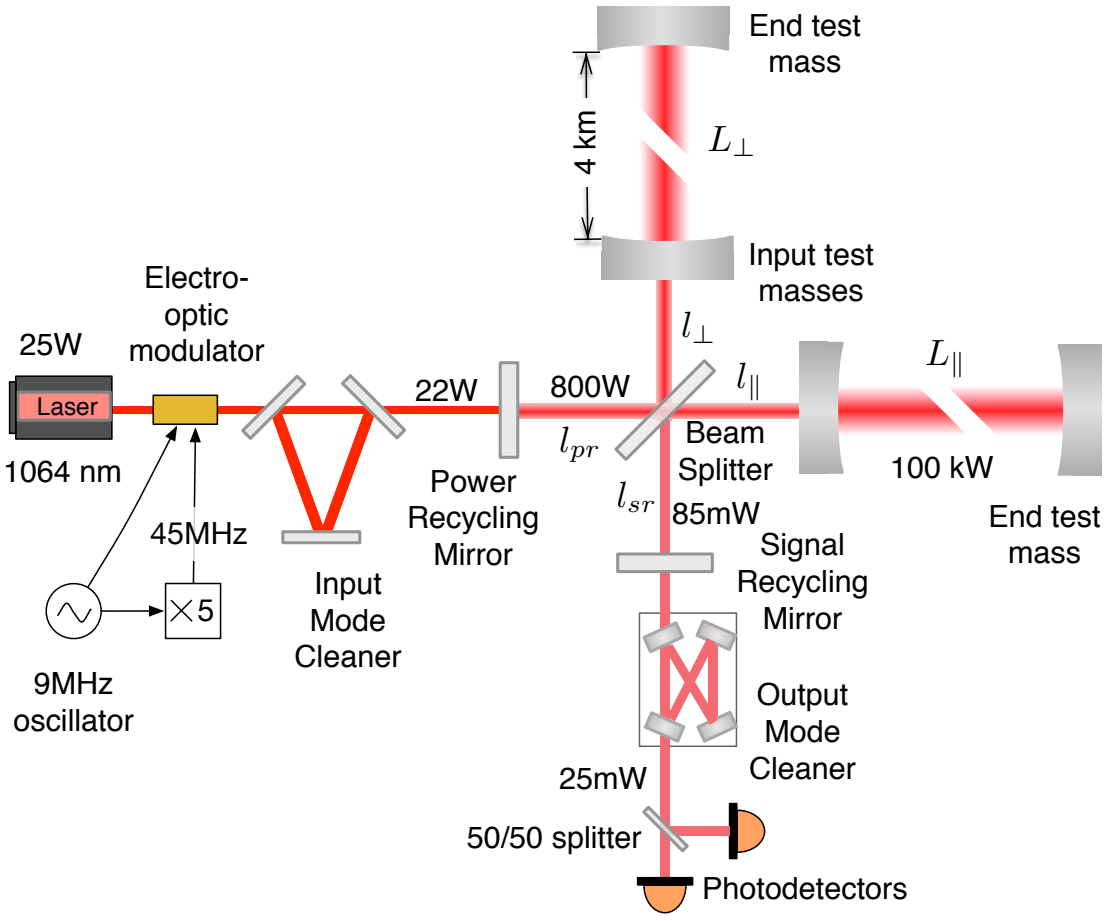

Figure 1.5 The layout of an aLIGO Michelson interferometer showing all optical cavities included in the design, and the associated circulating optical power in each cavity. A passing gravitational wave will introduce a difference between the two arm cavities of order $\delta l = L_\parallel - L_\perp$. The inclusion of the arm cavities enhances the optical power in the arms by a factor $G_{\rm arm} \simeq 270$. Figure reproduced from [229].

where $\eta = (m_1 m_2)/M_{\rm tot}^2$ is the symmetric mass ratio, $\mathcal{M}_c = (m_1 m_2)^{3/5}(M_{\rm tot})^{-1/5}$ is the chirp mass (for a binary with component masses m_1 and m_2) and ω is the angular frequency [147, 70]. Due to the spatial symmetry of a CBC, the emitted gravitational wave frequency $f_{\rm gw}$ is twice the orbital frequency, i.e. $\omega = \pi f_{\rm gw}$. Equation 1.7 can further be decomposed into $h^+(t)$ and $h^\times(t)$, the two polarisation states allowed by general relativity (cf. Figure 1.4), as

$$\begin{aligned} h^+(t) &= \frac{1}{2} h_0^{\rm inspiral}(1+\cos^2\iota)\cos[2\varphi(t)] \\ h^\times(t) &= h_0^{\rm inspiral}\cos\iota\sin[2\varphi(t)] \end{aligned} \tag{1.8}$$

where ι is the inclination between the line of sight and a direction characteristic to the source (often the orbital angular momentum) and $\varphi(t)$ corresponds to the time-dependent phase evolution of the gravitational wave source [207]. As the system is losing energy into emitted gravitational waves the orbit is shrinking, and thus the emitted frequency increases monotonically as

$$\dot{f}_{\rm gw} = \left(\mathcal{M}_c \frac{G}{c^3}\right)^{5/3} \frac{96}{5}\pi^{8/3} f_{\rm gw}^{11/3} \tag{1.9}$$

to leading order (this is usually called a chirp) [56]. Note, therefore, that h_0 must be a function of time as well since ν increases as the binary loses energy when its orbit shrinks. To include higher order terms the right hand side of Equation 1.2 can be expanded as a Taylor series in the dimensionless orbital velocity ν for both the amplitude and the phase of the emitted wave [55]. These post-Newtonian (pN) terms start to include (at increasingly higher order) the mass ratio $q \equiv m_2/m_1 \leq 1$, the components of the compact objects' spin vectors parallel to the orbital angular momentum and later the perpendicular spin components and cross correlations between these physical properties. For systems containing neutron stars, tidal effects caused by the presence of matter will also affect the orbital evolution, most prominently at the end of the inspiral phase [197]. As $f_{\rm gw}$ increases, so does ν and eventually the binary will reach a limit ($\nu \sim 1$) where the pN expansion no longer is valid. To ensure the accuracy of the waveforms, the inspiral phase is commonly terminated at the innermost stable circular orbit (ISCO) after which the two objects initiate the plunge towards the final merger.

The ISCO occurs, to leading order, at a $f_{\rm gw}$ of

$$f_{\rm ISCO} = 4.4{\rm kHz}\left(\frac{M_\odot}{M_{\rm tot}}\right) . \tag{1.10}$$

The length of a chirp is to leading order

$$\tau \simeq 159\,{\rm s}\left(\frac{1.22\,M_\odot}{\mathcal{M}_c}\right)^{5/3}\left(\frac{20{\rm Hz}}{f_{\rm ref}}\right)^{8/3} , \tag{1.11}$$

where $f_{\rm ref}$ is a reference frequency, usually taken as the lower bound of the detector sensitivity.

For analysis purposes, as will be further discussed in section 1.3, it is often useful to represent an inspiral waveform as its Fourier transform in the frequency domain. One commonly used representation is TaylorF2 [63] which for a face-on binary ($\iota = 0$), with its physical parameters described by $\vec{\theta}$, directly overhead a detector describes the waveform through a Taylor expansion in the post-Newtonian parameter ν as

$$\tilde{h}(f,\vec{\theta}) = \frac{1}{r}\sqrt{\frac{5}{24}}\pi^{-2/3}\mathcal{M}_c^{5/6}f^{-7/6}e^{i\Psi(f,\vec{\theta})} , \tag{1.12}$$

assuming no higher-order corrections to the waveform amplitude. Here the phase $\Psi(f,\vec{\theta})$ is given as

$$\Psi(f,\vec{\theta}) = 2\pi f t_c - \phi_c - \frac{\pi}{4} + \frac{3}{128\eta\nu^5}\sum_{k=0}^{7}(\alpha_k + \beta_k\log(\nu))\nu^k \tag{1.13}$$

where t_c and ϕ_c are the time and phase of the waveform at coalescence and the coefficients α_k, β_k are functions of $\vec{\theta}$ for each post-Newtonian order $k/2$.

An alternative expansion of Equation 1.2 comes from the effective-one-body (EOB) formalism where results from the pN approximation are supplemented by strong-field effects from the limit of a test particle inspiraling into a compact object [61, 62, 72, 73, 42, 225, 173]. These results are resummed into a Hamiltonian and then improved by the inclusion of unknown higher order pN terms from numerical relativity. The current EOB waveform models can be constructed to include both generic, precessing, spin effects [180] and also tidal effects [114].

1.2.2.2 Merger

After the ISCO the analytical expressions of the inspiral are in general no longer valid. In the last decade significant breakthroughs in numerical relativity (NR) have presented solutions in general relativity which cover the merger of two (previously) orbiting compact objects [192, 64, 41]. NR waveforms can now be constructed for a variety of binary configurations (as solutions in general relativity are scale free for $\sim Mf$ the free parameters for NR waveforms are the mass ratio and the spins of the two compact objects[1]), and are commonly collected in catalogues and used for both calibration of general waveform models as well as detailed studies of strong-field gravitation [172, 195, 112, 120, 235].

1.2.2.3 Ringdown

The merger phase of a coalescence can be taken to end the peak of the waveform, which for a BBH corresponds to when a common horizon has been formed, the resulting compact object exists in an excited spatial state. As it settles down into a stable final state the compact object radiates the excess potential energy as gravitational waves in form of a superposition of quasi-normal modes (QNMs) [81, 52, 120]. To leading order, the dominant QNM emits a strain

$$h^{\text{ringdown}}(t) \approx 10^{-20}\,\frac{1\text{ Mpc}}{r}\,\frac{M}{M_\odot}\,e^{-t/\mathcal{T}}\,\cos(2\pi f_0 t)\,. \tag{1.14}$$

where $\mathcal{T} = \frac{2}{\pi}\,\frac{1}{f_0}$ and $f_0 \simeq 10\,\text{kHz}\,\frac{M_\odot}{M}$ (see also the discussion around Equation 3.1 and Figure 3.5).

1.2.2.4 Complete CBC waveform

In order to fully characterise the entire coalescence of two compact objects the individual components of the inspiral–merger–ringdown are combined into a hybridised waveform as in Figure 1.6 [176]. This is done by matching the phase and amplitude across the regions overlapping the individual waveform components,

[1] NR waveforms can also include matter effects, for example describing the tidal deformation of neutron stars. These effects would however break the scale freedom and introduce an additional mass parameter [197].

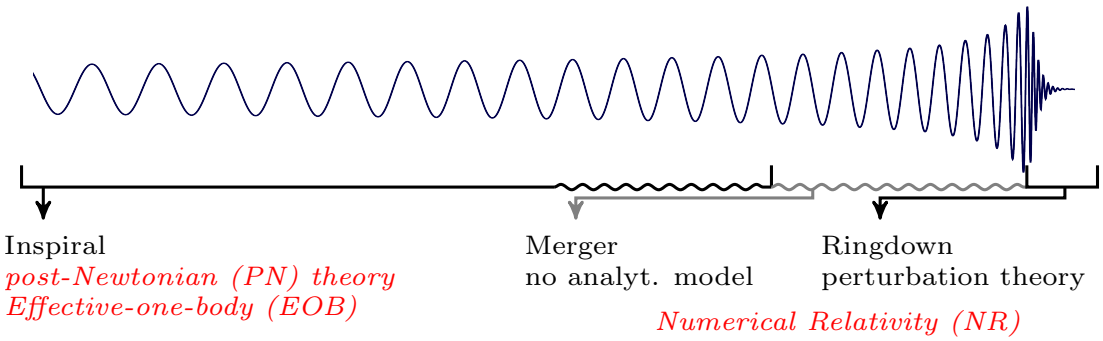

Figure 1.6 Showing an example waveform in the time domain for a BBH system with non-spinnning components. As the analytically described inspiral phase breaks down the waveform is required to be hybridised against a NR solution. After this merger phase, indicated by the wavy line, the emitted waveform can again be explained analytically through a superposition of QNMs. Figure reproduced from [176].

either using a phenomenological model [208, 104, 209, 120, 126] or more directly within the EOB framework [225, 180, 114].

1.3 Gravitational wave data analysis

Although ground-based gravitational wave detectors are sensitive to a wide variety of sources (e.g. unmodelled bursts [14, 4, 15, 10, 18, 231], continuous waves [5, 2, 7, 3, 8] and stochastic signals [24, 16, 9, 6, 20]) this thesis will focus only on the data analysis in use for compact binary coalescence signals.

1.3.1 Searches for CBC

A typical CBC signal detectable in aLIGO can be expected to induce strains of order $h \sim 10^{-23} \sim \delta l/l$, which for the arm lengths of $l \sim$ few km for aLIGO/AdV requires a differential arm length of $\delta l \sim 10^{-20}$ m to be reliably measurable. This can be translated directly into requirements on the stability and sensitivity of the detectors [106]. As it has been demonstrated during the fall of 2015, the aLIGO detectors have achieved a level of sensitivity enough to claim a detection of at least one CBC event [22, 21, 229]. The detector sensitivity is limited in different frequency bands by different noise sources, as shown in Figure 1.7. At low

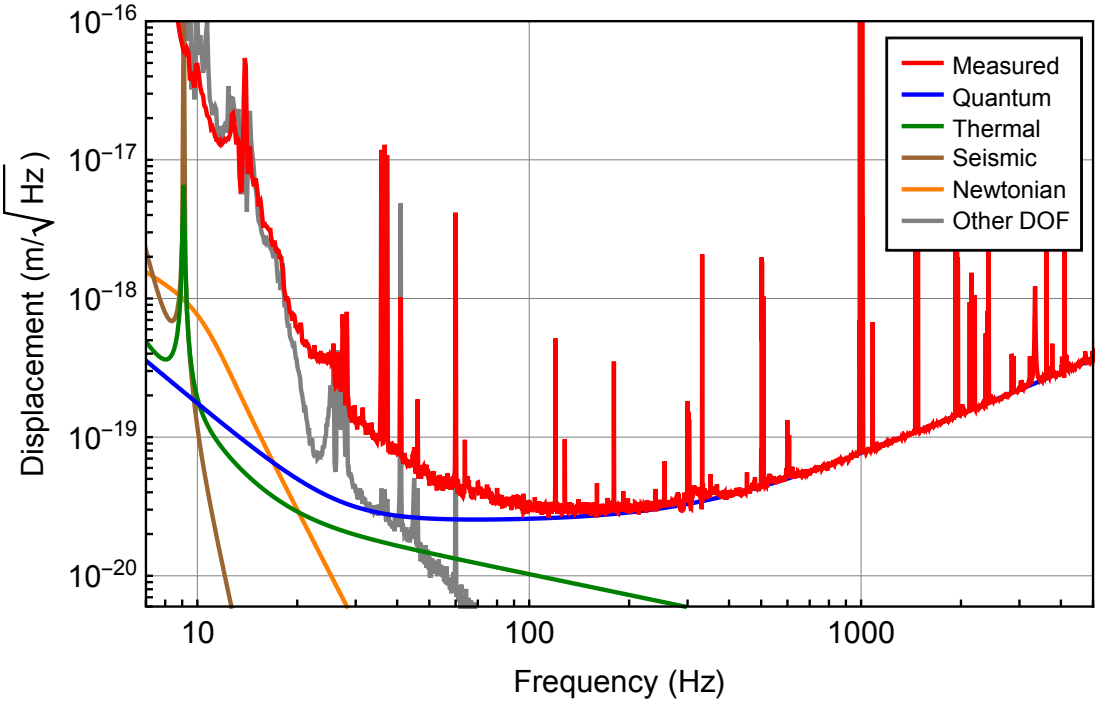

Figure 1.7 Showing in red the measured sensitivity to displacements δl in the Hanford detector during the first observational run of aLIGO. This measured sensitivity is accounted for, as a sum of the individual noise components, for the majority of the sensitive frequency band, apart from between $20 \lesssim f \lesssim 100$ Hz. Figure reproduced from [21].

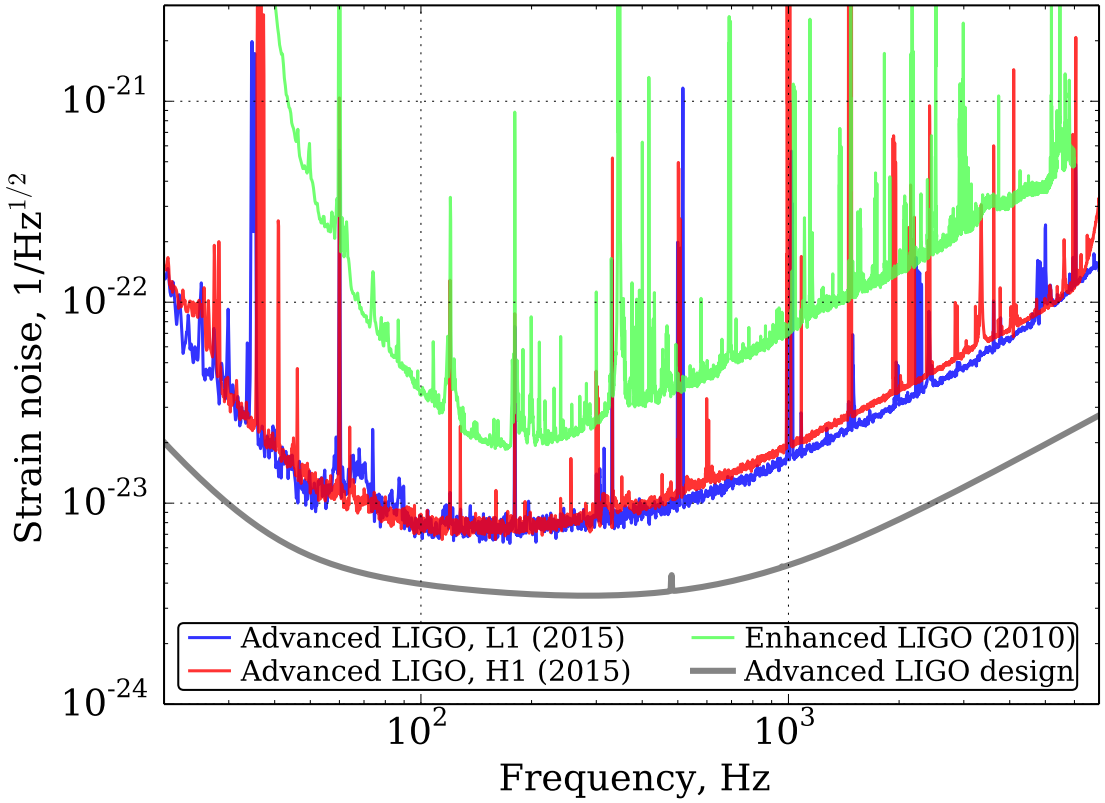

Figure 1.8 The measured noise amplitude spectral density represented as a strain sensitivity for the two aLIGO detectors, H1 and L1, during the first observational run in 2015. Also shown are the final sensitivity of the initial LIGO detectors as well as the predicted design sensitivity for aLIGO. Figure reproduced from [229].

frequencies the noise is dominated by seismic ground motion, thermal (Brownian) noise in the mirror, coatings and suspensions and cross coupled noises originating in the interferometer control system (labeled "other DOF" in Figure 1.7). At higher frequencies the noise budget is instead completely dominated by quantum effects such as shot noise and radiation pressure caused by uncertainties in the photon count inside the interferometer and the photon arrival time at the readout. By dividing the displacement sensitivity by the arm length ($l = 4$ km for aLIGO) a noise amplitude spectral density (ASD) is produced, examples of which is shown in Figure 1.8. This can more easily be compared directly to a CBC strain signal as shown in Figure 1.10 [see 168, for a comprehensive comparison].

In terms of the assumptions made about the noise within the data analysis

pipelines it is considered to be Gaussian and stationary over a timescale of any given CBC signal (∼seconds to minutes). In practice this is not the case, see for example section III.D in [11] and section III.K in [229] for further discussion, and a large effort is put towards towards characterising and mitigating these effects in terms of them limiting the opportunities for detections [30, 31, 53, 54, 139, 230].

The fact that CBC signals are so well modelled, as discussed in subsection 1.2.2, this source group is suitable for a direct matched filtering approach where the data $d(t)$ from a detector can be represented as

$$d(t) = n(t) + h(t) \tag{1.15}$$

consisting of background noise $n(t)$ and a CBC waveform $h(t)$. By comparing $d(t)$ against a set of template waveforms $h(\vec{\theta}, t)$, where $\vec{\theta}$ represent the parameters describing the modelled CBC source, a detection statistic can be constructed which then is maximised for the template with the highest match against $d(t)$. A detection statistic which is often presented is the signal to noise ratio (SNR), ρ, which describes the relative power contained within a proposed gravitational wave against the noise power. For a network of interferometers this is constructed as

$$\rho^2 = \sum_{\text{IFO}} \left(\frac{\langle d | h_{\text{IFO}}(\vec{\theta}) \rangle}{\sqrt{\langle h_{\text{IFO}}(\vec{\theta}) | h_{\text{IFO}}(\vec{\theta}) \rangle}} \right)^2 \tag{1.16}$$

where the quantity in the angle brackets is the noise weighted inner product defined as

$$\langle a | b \rangle = 4\,\text{Re} \int_{f_{\text{Low}}}^{f_{\text{High}}} \frac{\tilde{a}(f)\tilde{b}^*(f)}{S_{\text{n,IFO}}(f)}\,\text{d}f. \tag{1.17}$$

where $\tilde{a}(f), \tilde{b}(f)$ are complex-valued Fourier transforms of the time-domain signals a, b (e.g. $a \equiv a(t)$), the integral is performed over the detector sensitivity band defined for frequencies $f_{\text{Low}} \leq f \leq f_{\text{High}}$ and $S_{\text{n,IFO}}(f)$ is the one-sided power spectral density (PSD = (ASD)^2) for each interferometer (assuming Gaussian and stationary noise). $\tilde{h}_{\text{IFO}}(f, \vec{\theta})$ is the frequency domain representation of the "global" waveform $\tilde{h}^{+,\times}(f, \vec{\theta})$ (defined in Equation 1.8) as projected onto the

detector specific antenna beam patterns $F^{+,\times}$ defined as

$$\begin{aligned} F^{+} =& \frac{1}{2}(1-\cos^2\theta)\cos 2\phi \cos 2\psi - \cos\theta \sin 2\phi \sin 2\psi \\ F^{\times} =& \frac{1}{2}(1-\cos^2\theta)\cos 2\phi \sin 2\psi - \cos\theta \sin 2\phi \cos 2\psi \end{aligned} \tag{1.18}$$

where the angles θ, ϕ are polar and azimuthal angles defined with respect to a plane containing the arms of a detector, as shown in Figure 1.9. The ψ angle corresponds to a rotation of the source in the sky plane with respect to the detector plane. Together, the waveform and antenna pattern gives

$$\tilde{h}_{\mathrm{IFO}}(f,\vec{\theta}) = F^{+}_{\mathrm{IFO}}\tilde{h}^{+}(f,\vec{\theta}) + F^{\times}_{\mathrm{IFO}}\tilde{h}^{\times}(f,\vec{\theta})\,. \tag{1.19}$$

Three example $\tilde{h}(f,\vec{\theta})$ are shown in Figure 1.10 highlighting the different contribution of the inspiral, merger and ringdown for the different source groups. Also compare this figure to Figure 3.8 where signals from more massive sources with more extreme mass ratios are shown.

Apart from ρ, the ability of a given template to describe the signal contained in the data can also be quantified in terms of a match

$$M = \max_{t_c,\phi_c} \frac{\langle d|h(\vec{\theta}))\rangle}{\sqrt{\langle d|d\rangle\langle h(\vec{\theta})|h(\vec{\theta})\rangle}}\,, \tag{1.20}$$

maximizing over time and phase shifts between d and $h(\vec{\theta})$. The match is frequently used in the construction of a search pipeline for the discretisation of the continuous parameter space into a bank of template waveforms. For any gravitational wave signal incident on a detector the template bank used for searches must be densely enough sampled such that the vast majority of possible signals are detectable. This density is quantified in terms of the mismatch, defined as $1-M$, between adjacent waveforms in the template bank. A mismatch of ϵ between a true signal and the closest template would, due to waveform amplitudes having a $1/r$ dependance, be equivalent to only being able to detect this specific template out to a distance $1-\epsilon$ times the "nominal" detection threshold distance. This in turn reduces the available detection volume by a fraction $(1-\epsilon)^3$ and,

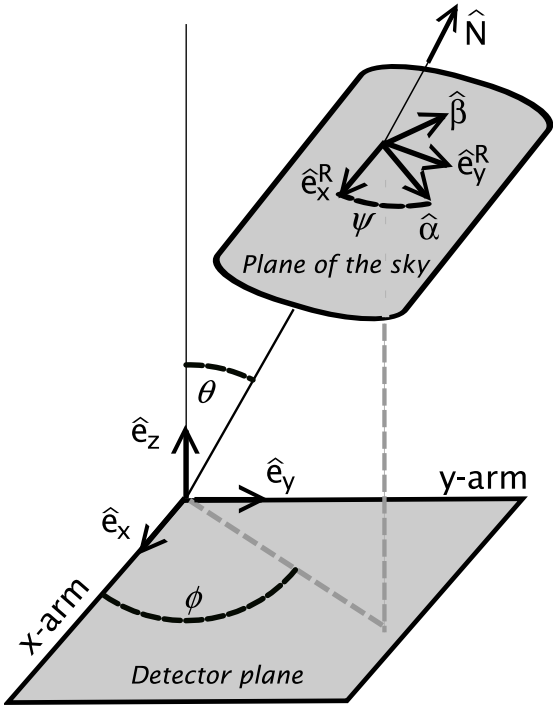

Figure 1.9 The relative orientation of a plane contating the two arms of a detector (described by the detector response tensor $[\hat{e}_x, \hat{e}_y, \hat{e}_z]$) and a plane in the sky contating a gravitational wave source (described by the source radiation tensor $[\hat{e}_x^R, \hat{e}_y^R, \hat{N}]$, where $\hat{N}$ is the line of sight). A rotation of the source in the sky frame (corresponding to a misalignment of the two tensors) is described by the angle ψ. Figure reproduced from [207].

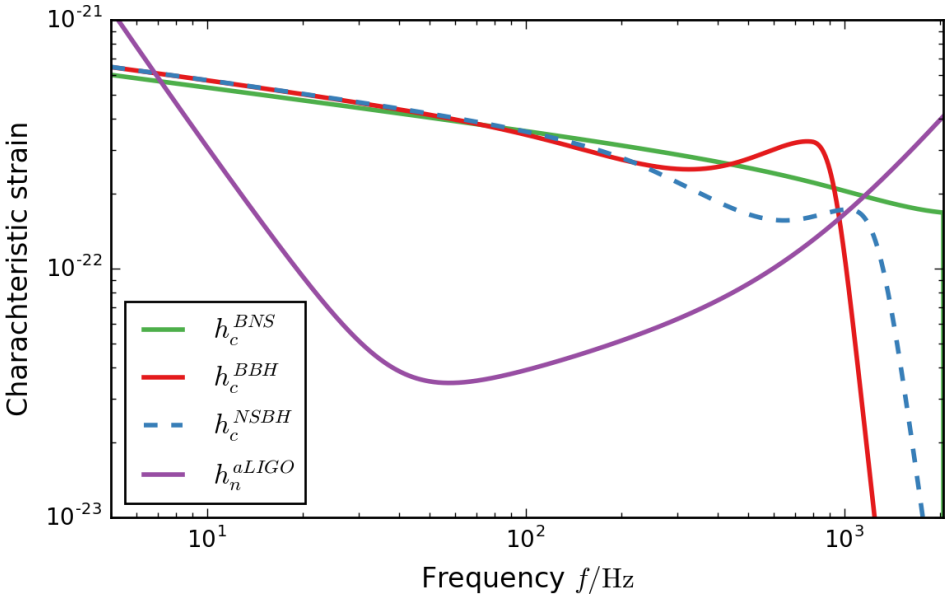

Figure 1.10 Shown here are the characteristic strain $h_c = 2f|\tilde{h}(f,\vec{\theta})|$ for a BNS ($m_1 = m_2 = 1.4M_\odot$), BBH ($m_1 = m_2 = 10M_\odot$) and NSBH ($m_1 = 10M_\odot, m_2 = 1.4M_\odot$) waveform respectively (all sources are taken as non-spinning)[168]. As a comparison the noise amplitude $h_n = \sqrt{fS_n(f)}$ for the Advanced LIGO design sensitivity from Figure 1.8 is also shown. The waveforms all have $\rho = 15$ for a one-IFO detection with the displayed sensitivity.

assuming an isotropic and uniform in volume distribution of sources, a fractional loss in detection rate of $1 - (1 - \epsilon)^3$. A typical template bank is designed for a maximum mismatch between adjacent templates of $\lesssim 0.03$[1], which leads to at most $\sim 10\%$ of incident gravitational wave signals not being detected [234].

Apart from finding detection candidate signals above the predetermined detection threshold, template banks are also sensitive to background events caused by noise in the detectors. This is primarily overcome by the requirement of observing any detection candidate in more than one detector, found with the same template using the same precalculated template bank within a time window following special relativity causality. Additional tests designed to downrank background triggers, such as a χ^2 statistic, can also be implemented [29]. Even so, the inability to perform observations of data *completely* devoid of any possible gravitational wave signals, combined with the observed non-Gaussianity and non-stationarity of the noise produces a stream of background candidate events. This background is characterised by again utilising the maximum inter-detector travel time for a real signal. For example, by shifting the data between the two aLIGO detectors more than 15 ms out of sync any event "detected" in both interferometers is guaranteed to be purely from a background population. These timeshifts are repeated until a significant number of background events have been produced. The distribution of these background events in the chosen detection statistic can then be converted into a false alarm probability, as the fraction of background events louder than a given threshold, or equivalently a false alarm rate reporting how often a background event at a certain threshold is recorded in the observed time period (including the large number of time shifts).

1.3.2 Parameter Estimation

For any candidate event which falls above a detection threshold, the use of a discrete template bank leaves a large uncertainty in the source parameters. This is further enhanced by using template banks with a reduced parameter space which can introduce and shift correlations and biases in the recovered parameters [cf.

[1]Many adjacent templates will have a smaller mismatch due to the commonly used implementation of stochastic placement of templates in a bank.

aligned versus precessing spins, 66, 107]. This uncertainty can in principle be reduced by the use of a more densely sampled template bank, covering a more generic set of parameters, but this quickly becomes impractical due to the high dimensionality and complex structure of the parameter space. To overcome this, primarily computational, hurdle a minimal set of information from the search pipeline output (often only the time of coalescence) is taken as input to a coherent stochastically sampled Bayesian parameter estimation analysis. Where the detection search output can be seen as point estimates for the source parameters, the dedicated parameter estimation analysis produces a full set of posterior probability density functions (PDF) containing information about both various point estimates as well as associated credible intervals [150, 123, 11, 247, 232]. The posterior PDF is given by Bayes' theorem as

$$p(\vec{\theta}|d,H) = \frac{p(\vec{\theta}|H)p(d|\vec{\theta},H)}{P(d|H)} = \frac{L\pi}{Z} \tag{1.21}$$

where $\pi = p(\vec{\theta}|H)$ is the prior distribution of the parameters $\vec{\theta}$ following the signal model H. $L = p(d|\vec{\theta},H)$ is the likelihood of observing a dataset d given $\vec{\theta}$, again under the constraints of H. By assuming Gaussian and stationary noise L is given as

$$L(\vec{\theta}) \equiv p(d|\vec{\theta},H) \propto \prod_{\mathrm{IFO}} \exp\left(-2\int_0^\infty \frac{|d_{\mathrm{IFO}}(f) - h_{\mathrm{IFO}}(f,\vec{\theta})|^2}{S_{n,IFO}(f)}\mathrm{d}f\right) \tag{1.22}$$

or equivalently

$$\begin{aligned} L(\vec{\theta}) &\propto \prod_{\mathrm{IFO}} \exp\left(-\frac{1}{2}\langle d_{\mathrm{IFO}}(f) - h_{\mathrm{IFO}}(f,\vec{\theta})|d_{\mathrm{IFO}}(f) - h_{\mathrm{IFO}}(f,\vec{\theta})\rangle\right) \\ &= \prod_{\mathrm{IFO}} \exp\left(\langle d|h\rangle - \frac{1}{2}(\langle d|d\rangle + \langle h|h\rangle)\right) \end{aligned} \tag{1.23}$$

where the data from each interferometer is represented in the frequency domain as $d_{\mathrm{IFO}}(f)$, defined as the Fourier transform of Equation 1.15. The signal model is represented by the template waveform $h_{\mathrm{IFO}}(f,\vec{\theta})$, again in the frequency domain. For a study of purely parameter estimation, where only information about the

relative probability of certain parameter variations is relevant, the denominator of Equation 1.21 acts as a normalisation constant. However, this constant

$$Z = P(d|H) = \int p(\vec{\theta}|H)p(d|\vec{\theta}, H)d\vec{\theta}\,, \tag{1.24}$$

called the evidence, quantifies the ability of the signal model H to describe the data. By taking ratios of evidences for different models a so called Bayes factor can be constructed, which then directly compares the relative validity of different H [248]. The most commonly used Bayes factor compares a model with an embedded signal, as described by the data in Equation 1.15, to a noise only model acting as a signal null hypothesis. For a well defined and quantifiable noise model, this Bayes factor can be used as a powerful detection statistic.

After defining the posterior PDF and its constituents the mechanics for exploring the parameter space of interest are laid out. While it is possible to explore "all" combinations of parameters, often through a densely sampled grid, this becomes unfeasible for high-dimensional problems. Instead, the parameter space can be explored stochastically, which by construction puts a stronger focus on regions of high posterior probability and reduces the complications caused by the complex structure of the likelihood function and high dimensional parameter spaces.

1.3.2.1 Markov Chain Monte Carlo

One of the most commonly used stochastic sampling methods is Markov Chain Monte Carlo, or MCMC, which is designed to produce a set of samples across a parameter space with a density proportional to that of the resulting posterior PDF [242, 243]. By generating a Markov chain of samples $\vec{\theta_i}$ (within the set $\{\vec{\theta_i} \mid i = 0, 1, 2...\}$), where the individual sample position depends solely on the position of the previous sample, the primary condition for the reliability and stability of the MCMC to sample the posterior probability $p(\vec{\theta})$ correctly falls on the implemented transition probability $P(\vec{\theta}_{i-1} \to \vec{\theta}_i)$. This probability must satisfy the condition of detailed balance

$$p(\vec{\theta}_i)P(\vec{\theta}_i \to \vec{\theta}_{i-1}) = p(\vec{\theta}_{i-1})P(\vec{\theta}_{i-1} \to \vec{\theta}_i) \tag{1.25}$$

which explicitly requires that the probability of a transition between two states in an equilibrium distribution must be equal in either direction. In addition, this also means that a MCMC sampler is more likely to transition to a point of higher $p(\vec{\theta})$ than away from it. Lastly, detailed balance ensures that as long as any given sample is drawn from the posterior PDF, every subsequent sample will also belong to this distribution as well as ensuring that the combined set of samples $\{\vec{\theta}_i \mid i = 0, 1, 2...\}$ asymptotically approaches the true $p(\vec{\theta})$. This is commonly done using the Metropolis-Hastings algorithm [160, 111] where a proposed jump state $\vec{\theta}'$ is drawn from a trial distribution $Q(\vec{\theta}_i \to \vec{\theta}')$ which, as long as it can access the entire parameter space under investigation, can be determined freely. The proposed sample $\vec{\theta}'$ is accepted into the Markov Chain with the probability

$$R(\vec{\theta}_i \to \vec{\theta}') \equiv \min \left\{ 1, \frac{p(\vec{\theta}')Q(\vec{\theta}' \to \vec{\theta}_i)}{p(\vec{\theta}_i)Q(\vec{\theta}_i \to \vec{\theta}')} \right\} , \tag{1.26}$$

if the sample is accepted $\vec{\theta}_{i+1} = \vec{\theta}'$ and otherwise $\vec{\theta}_{i+1} = \vec{\theta}_i$. To minimise any bias in the sampling the initial position of the chain is usually randomised. This leads to a so-called "burn-in" period before the sampler has explored the parameter space such that the regions of high likelihood has been found and any correlation to the starting position has been dissipated. The latter is an example of nearby samples having a non-negligible degree of correlation between their relative positions, primarily due to imperfect jump proposals. To ensure that the final chain contain only statistically independent posterior samples, the autocorrelation length of the "raw" chain is computed after which it is thinned into its final form by selecting samples with a cadence set by this autocorrelation length. In absence of strong prior information on the structure of the posterior, the trial distribution Q is usually defined as a multi-dimensional Gaussian with a mean $\vec{\theta}_i$ and widths for each parameter tuned during the burn-in phase. For highly structured posterior distributions, like a majority of gravitational wave analysis cases which exhibits both complex correlations between parameters and strong multi-modality, this simple Q will be suboptimal. Then more advanced sampling techniques such as differential evolution or parallel tempering can be applied. Differential evolution sidesteps the limitations of a naive Q by the use

of knowledge about previously accepted jump states. This is done by randomly drawing two previous samples $\vec{\theta}_a$ and $\vec{\theta}_b$ and from these propose a new sample $\vec{\theta}'$ according to

$$\vec{\theta}' = \vec{\theta}_i + \gamma(\vec{\theta}_b - \vec{\theta}_a) \tag{1.27}$$

where γ is a free parameter. This can be used both for jumps along known linear correlations (with $0 \leq \gamma < 1$) and for jumps between modes such as where $\vec{\theta}_i$ and $\vec{\theta}_a$ are from the same posterior mode in which case $\vec{\theta}'$ will be drawn from the same mode as $\vec{\theta}_b$ (when $\gamma = 1$). Parallel tempering [247, 250] is implemented by initialising several MCMC's simultaneously, each with a different effective temperature $T \geq 1$ modifying the likelihood function as

$$L_T(\vec{\theta}) \equiv L(\vec{\theta})^{\frac{1}{T}} \, . \tag{1.28}$$

For $T > 1$ this will smooth any sharp features of the original likelihood function and enhance the access for transitions between different modes. If a chain at a higher temperature finds a region of high likelihood this information can be passed down the temperature ladder in a proposed swap of states which are accepted with a probability

$$R_{PT}(\vec{\theta}_j \to \vec{\theta}_i) \equiv \min \left\{ 1, \left(\frac{L(\vec{\theta}_j)}{L(\vec{\theta}_i)} \right)^{\frac{1}{T_i} - \frac{1}{T_j}} \right\} \tag{1.29}$$

where $T_j > T_i$. Together with additional gravitational wave specific jump proposals [247], these techniques makes MCMC both versatile, reliable and efficient in sampling complex and high-dimensional parameter spaces.

1.3.2.2 Nested Sampling

Another approach for exploring such parameter spaces is Nested sampling [219], which instead of sampling a posterior distribution focuses on evaluating the model evidence

$$Z = \int L(\vec{\theta})\pi(\vec{\theta}) d\vec{\theta} = \int L dX \tag{1.30}$$

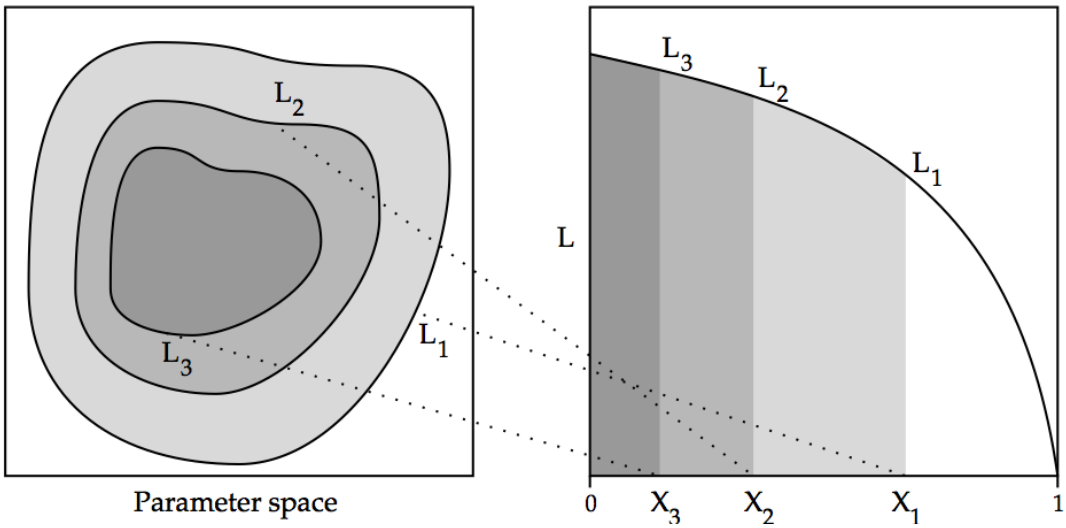

Figure 1.11 For an arbitrary paramteter space samples are sorted by amount of enclosed prior mass X. This by construction also sorts the samples in terms of increasing likelihood. Figure reproduced from [219]

where $dX \equiv \pi(\vec{\theta})d\vec{\theta}$ is a mass element associated with the prior PDF $\pi(\vec{\theta})$. This can in turn be used to evaluate the equivalent mass element for a posterior PDF $p(\vec{\theta})$ as

$$dP = p(\vec{\theta})d\vec{\theta} = \frac{L(\vec{\theta})\pi(\vec{\theta})d\vec{\theta}}{Z} \tag{1.31}$$

For a high-dimensional parameter space the evaluation of the integral in Equation 1.30 will be very computationally expensive, but through the recasting of the integral in terms of dX and defining the cumulative prior mass, containing all likelihood values greater than λ, as

$$X(\lambda) = \int_{L(\vec{\theta})>\lambda} \pi(\vec{\theta})d\vec{\theta} \tag{1.32}$$

it has been reduced to a much simpler monotonically increasing function taking values in the range $X(0) = 1$ to $X(\infty) = 0$. By finding the inverse of Equation 1.32, $L(X(\lambda)) = \lambda$, the evidence as given by Equation 1.30 becomes

$$Z = \int_0^1 L(X)dX \tag{1.33}$$

where as shown in Figure 1.11 the integrand $L(X)$ is always positive and decreasing. Dividing the prior mass X into small elements, as required in the transformation from $\vec{\theta}$, then allows the prior mass to be sorted according to increasing likelihood within each prior mass element which allows for the integral in Equation 1.33 to be represented as a weighted sum over these mass elements. As increasing X by construction gives decreasing $L(X)$ it is then possible to put bounds on the evidence as

$$\sum_{i=0}^{m} L_i(X_i - X_{i+1}) \leq Z \leq \sum_{i=1}^{m} L_i(X_{i-1} - X_i) + L_{max}X_m \tag{1.34}$$

for a set of m prior mass elements and the highest likelihood point in this set given by L_{max}. The highest computational expense within a nested sampling method would be the sorting of the prior mass elements, but through the record of previous samples, and their associated likelihood values, it is possible to sidestep the sorting altogether by only accepting samples with $L(X) > L_{i-1}$.

For the nested sampling implementation used for CBC parameter estimation [248, 11, 247] the algorithm is initialised by stochastically sprinkling a predetermined number of samples called live points, using a MCMC (as described in subsubsection 1.3.2.1), following the defined prior PDF. After sorting the samples according to prior mass, or likelihood, the lowest likelihood sample is removed from the set of live points and a new sample is drawn from the prior distribution. As shown in Figure 1.12 samples are only accepted into the set of live points if their likelihoods are higher than the bound set by the new lowest likelihood. The condition for termination can be either set to a predetermined number of steps or more often when any additional sample would be unable to increase the evidence by a predefined small fraction (given as the width of the bounds from Equation 1.34). After termination the collection of discarded live points are reweighted according to their individual prior and likelihood values, combined with the global evidence, to produce a set of posterior samples. There are also extensions to nested sampling where the prior volumes are divided into smaller regions for improved efficiency for sampling highly multi-modal PDFs [c.f. MultiNest 89, 97].

The main advantage of nested sampling over a "pure" MCMC approach is that

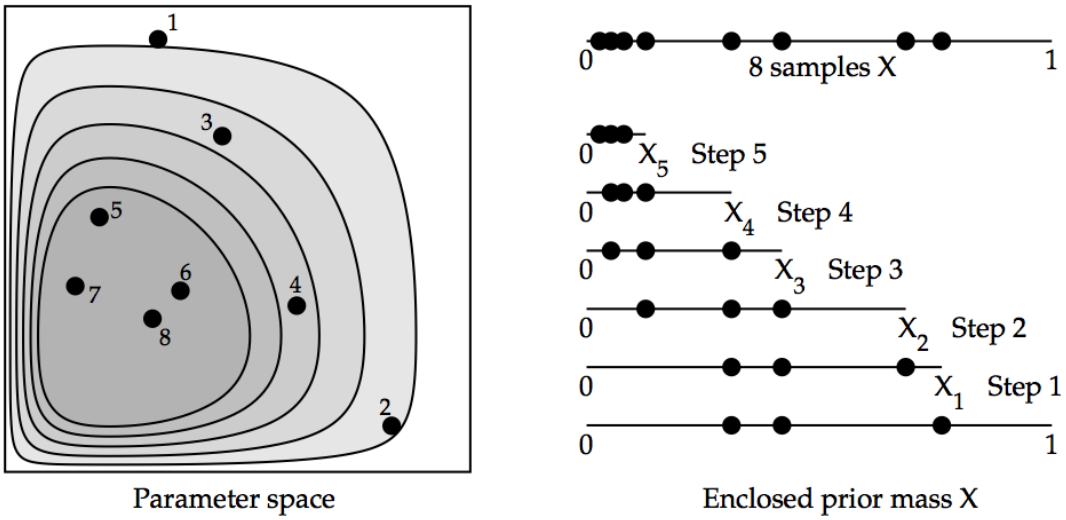

Figure 1.12 For an example analysis containing three live points it is clear how the sample enclosing the highest prior mass X, and representing the lowest likelihood, is replaced in each step by a higher likelihood point. After five steps the nested sampling is terminated, leaving in total eight samples distributed according to the likelihood PDF with a higher sample density at higher likelihoods. Figure reproduced from [219]

by construction an evidence is computed, therefore encouraging use of model selection approaches through Bayes factors. It has however been shown in multiple studies [11, 247, 232] that both samplers show a high level of agreement, and thus are both able to efficiently produce a set of samples which are an accurate representation of the posterior distribution under investigation

1.4 Structure of Thesis

1.4.1 Chapter 2

Chapter 2 focuses on the role of post-Newtonian dynamics in the formation and evolution of compact binary black holes which includes an intermediate mass black hole.

This chapter is adapted from a paper in preparation by *Carl-Johan Haster*, Fabio Antonini, Ilya Mandel and Vicky Kalogera [108]. This paper grew out of a collaboration between the four authors during my pre-doctoral fellowship at the Center for Interdisciplinary Exploration in Astrophysics at Northwestern University. My contribution to this work was *(i)* initialised, ran and post-processed the N-body of the 12 cluster models, *(ii)* lead the analysis of the results of the IMBH–BH dynamics *(iii)* wrote the paper. The remainder of this subsection is adapted from the abstract of this paper.

The intermediate mass-ratio inspiral of a stellar compact remnant into an intermediate mass black hole (IMBH) can produce a gravitational wave (GW) signal that is potentially detectable by current ground-based GW detectors (e.g., Advanced LIGO) as well as by planned space-based interferometers (e.g., eLISA). Here, we present results from direct integration of the post-Newtonian N-body equations of motion describing stellar clusters containing an IMBH and a population of stellar black holes (BHs) and solar mass stars. We take particular care to simulate the dynamics closest to the IMBH, including post-Newtonian effects up to order 2.5. Our simulations show that the IMBH readily forms a binary with a BH companion. This binary is gradually hardened by transient 3-body or 4-body encounters, leading to frequent substitutions of the BH companion, while the binary's eccentricity experiences large amplitude oscillations due to the

Lidov-Kozai resonance. We also demonstrate suppression of these resonances by the relativistic precession of the binary orbit. We find an intermediate mass-ratio inspiral in one of the 12 cluster models we evolved for ~ 100 Myr. This cluster hosts a $100M_{\odot}$ IMBH embedded in a population of 32 $10M_{\odot}$ BH and 32,000 $1M_{\odot}$ stars. At the end of the simulation, after $\sim$ 100 Myr of evolution, the IMBH merges with a BH companion. The IMBH-BH binary inspiral starts in the eLISA frequency window ($\gtrsim$ 1mHz) when the binary reaches an eccentricity $1 - e \simeq 10^{-3}$. After $\simeq 10^5$ years the binary moves into the LIGO frequency band with a negligible eccentricity. We comment on the implications for GW searches, with a possible detection within the next decade.

1.4.2 Chapter 3

Chapter 3 consists of a parameter estimation study on intermediate mass ratio coalescences, like the binary formed in the study described in chapter 2.

This chapter is adapted from a paper by *Carl-Johan Haster*, Zhilu Wang, Christopher P. L. Berry, Simon Stevenson, John Veitch and Ilya Mandel. My contribution to this work was to *(i)* design the initial parameters of this study, *(ii)* aid Zhilu Wang (a summer student in the group) to run the simulations, *(iii)* lead the post-processing and collating of the results, *(iv)* write the paper. This paper is published in MNRAS [110] and has arXiv number 1511.01431. The remainder of this subsection is adapted from the abstract of this paper.

Gravitational waves from coalescences of neutron stars or stellar-mass black holes into intermediate-mass black holes (IMBHs) of $\gtrsim$ 100 solar masses represent one of the exciting possible sources for advanced gravitational-wave detectors. These sources can provide definitive evidence for the existence of IMBHs, probe globular-cluster dynamics, and potentially serve as tests of general relativity. We analyse the accuracy with which we can measure the masses and spins of the IMBH and its companion in intermediate-mass ratio coalescences. We find that we can identify an IMBH with a mass above 100 $M_{\odot}$ with 95% confidence provided the massive body exceeds 130 $M_{\odot}$. For source masses above $\sim$ 200 $M_{\odot}$, the best measured parameter is the frequency of the quasi-normal ringdown. Consequently, the total mass is measured better than the chirp mass for massive

binaries, but the total mass is still partly degenerate with spin, which cannot be accurately measured. Low-frequency detector sensitivity is particularly important for massive sources, since sensitivity to the inspiral phase is critical for measuring the mass of the stellar-mass companion. We show that we can accurately infer source parameters for cosmologically redshifted signals by applying appropriate corrections. We investigate the impact of uncertainty in the model gravitational waveforms and conclude that our main results are likely robust to systematics.

1.4.3 Chapter 4

Chapter 4 presents an accurate and computationally efficient method for parameter estimation of CBC signals.

This chapter is adapted from a paper by *Carl-Johan Haster*, Ilya Mandel and Will M. Farr. My contribution to this work was to *(i)* design and write the software used in this study, *(ii)* run simulations, *(iii)* verify the results, focusing on the accuracy of the recovered credible regions, against alternative methods, *(iv)* write the paper. This paper is published in Classical and Quantum Gravity [109] and has arXiv number 1502.05407. The remainder of this subsection is adapted from the abstract of this paper.

In many previous studies, predictions for the accuracy of inference on gravitational-wave signals relied on computationally inexpensive but often imprecise techniques. Recently, the approach has shifted to actual inference on noisy signals with complex stochastic Bayesian methods, at the expense of significant computational cost. Here, we argue that it is often possible to have the best of both worlds: a Bayesian approach that incorporates prior information and correctly marginalizes over uninteresting parameters, providing accurate posterior probability distribution functions, but carried out on a simple grid at a low computational cost, comparable to the inexpensive predictive techniques.

Chapter 2

$N-$body dynamics of Intermediate mass ratio inspirals

This chapter is adapted from a paper in preparation by *Carl-Johan Haster*, Fabio Antonini, Ilya Mandel and Vicky Kalogera [108]. This paper grew out of a collaboration between the four authors during my pre-doctoral fellowship at the Center for Interdisciplinary Exploration in Astrophysics at Northwestern University. My contribution to this work was *(i)* initialised, ran and post-processed the N-body of the 12 cluster models, *(ii)* lead the analysis of the results of the IMBH–BH dynamics *(iii)* wrote the paper.

2.1 Introduction

Intermediate mass black holes (IMBHs) are conjectured to occupy the mass range between stellar-mass black holes (BHs), with masses $\lesssim 100 M_\odot$, and supermassive black holes with masses $\gtrsim 10^6 M_\odot$ [see 165, for a review]. While the existence of some IMBH candidates in dwarf spheroidal galaxies has been conjectured by extending the M–σ relation [99] [but see 145], dynamical measurements of IMBHs in the few-hundred solar-mass range are extremely challenging [e.g., 183]. The best evidence for such lower mass IMBHs (with mass $\sim 100 M_\odot$) could come from ultraluminous X-ray sources [but see 49]; for example, [182] have claimed a mass of $\sim 400\ M_\odot$ for M82 X-1 from quasi-periodic oscillations, while a mass

around $10^4 M_\odot$ has been suggested for the brightest ultraluminous X-ray source HLX-1 [e.g., 86, 74, 95], but these dynamical measurements alone can not provide conclusive proof for the existence of IMBHs.

If these lower-mass IMBHs reside in globular clusters, they will play an important role in cluster dynamics [e.g. 237, 240, 128, 134, 146]. Of particular interest to our study is the likely tendency of IMBHs to dynamically form compact binaries with other compact remnants [e.g. 224, 163, 166, 32, 58, 151, 35, 156, 155]. Generally, these analyses find that the IMBH readily captures a binary companion. The binary is subsequently hardened through a sequence of 3-body and 4-body interactions, occasionally with substitutions which make a black hole (BH) of a few tens of solar masses the most likely IMBH companion, and possible Lidov-Kozai (LK) resonances [135, 129] if hierarchical triples are formed. Eventually, the IMBH-BH binary merges through the radiation of gravitational waves, emitting a signal that is potentially detectable by the Advanced LIGO ground-based GW detectors [106, 17, 220, 110].

Previous simulations of globular clusters with IMBH coalescences have generally simplified the interactions in order to avoid excessive computational cost. For example, Gültekin et al. [100] considered a series of individual Newtonian interactions interspersed with orbital evolution through GW emission. Mandel et al. [151] carried out analytical estimates of the hardening sequence to obtain the intermediate mass-ratio merger timescale. Leigh et al. [134] simulated the entire cluster with a mixture of analytical and numerical N-body analytical calculations, while MacLeod et al. [146] focused their N-body investigation on tidal disruptions of stars by the IMBH as well as merger events. We note that in the previous literature effects of pN terms are either not accounted for [134], or included only at the 2.5pN level [204, 146]. In this chapter we show a clear example in which lower order pN terms play a fundamental role in the dynamics. More specifically, an essential element that differs between the relativistic and non-relativistic dynamics turns out to be the 1pN precession of the periapsis.

We introduce our numerical method and the simulation setup in section 2.2. We describe our simulation results in section 2.3. We discuss the results, including the detectability of GWs from intermediate mass-ratio coalescences, in section 2.4.

2.2 Simulations

The N-body systems considered here consist of a massive particle, representing an IMBH, and two additional lower-mass species representing $10M_{\odot}$ compact remnants and $1M_{\odot}$ stars. Integrations of the N-body equations of motion were carried out using the direct summation N-body code phiGRAPEch [105]. This code incorporates Mikkola's algorithmic chain regularization scheme including post-Newtonian terms of order 1pN, 2pN and 2.5pN [AR-CHAIN, 162]. Velocity dependent forces were included using the generalized midpoint method described by Mikkola and Merritt [161]. The algorithm produces exact trajectories for Newtonian two-body motion and regular results for strong encounters involving arbitrary numbers of bodies. Particles moving beyond the "chain radius" (r_{chain}) were advanced using a fourth-order integrator with forces computed on GPUs using the Sapporo library [92]. The chain particles were influenced by the global cluster dynamics through the particles in a perturber region, within a radius $r_{perturb}$ from the IMBH. phiGRAPEch is an ideal tool for the study of the dynamics of IMBHs in star clusters because it allows to study with extremely high precision the joint effect of 1pN, 2pN and 2.5pN terms and their interplay with Newtonian perturbations to the motion.

We performed 12 simulations all initialized as a King model with no primordial binaries, containing two mass species (BHs and stars) with a relative mass ratio of $10:1$, and assuming that the total mass in BHs is 1% of the total cluster mass. Finally, an initially stationary IMBH was placed at the center of the cluster. The analytical King model where chosen because, despite of their dynamical simplicity, they provide a good fit to observed surface brightness profiles. King models are defined as approximate iso-thermal spheres (where the velocity of a particle is largely independent of its position in the cluster) with a modified density profile such that the energy, as well as the number density, decreases with radius until it becomes zero at the tidal radius $r_{\rm t}$. Together with the King radius

$$r_0 \equiv \sqrt{\frac{9\sigma^2}{4\pi G\rho_0}} \tag{2.1}$$

where σ is the velocity dispersion of the cluster and ρ_0 is its central density, this

defines the concentration parameter $W_0 \equiv r_t/r_0$ ($W_0 = 7$ for all our simulations). The simulations were performed with number of particles $N \subset \{32768, 65536\}$ IMBH mass, $M \subset \{50, 100, 200\}\, M_\odot$ and cluster virial radius r_v defined as

$$\frac{M_{\rm tot}^2}{r_v} \equiv \sum_{i=0}^{N} \sum_{j \neq i}^{N} \frac{m_i m_j}{|\vec{r}_i - \vec{r}_j|} \tag{2.2}$$

given cluster total mass $M_{\rm tot}$, and particle masses and distances m and $\vec{r}$ summed over all particle pairs i, j. r_v was in these simulations set as 3.5 pc which in turn gave $r_v \sim 5r_0$ for our choice of King models. For $N = 32768$ and all three IMBH masses, simulations with $r_v \subset \{0.35, 1.0\}$ pc were also performed. The inclusion of high-order pN terms fixes the physical scale of the cluster, thus removing the conventional freedom for rescaling simulations in cluster size and density.

We observe the IMBH forming a binary with a BH within $\lesssim$ 20Myr in every simulated cluster. Only in one cluster ($N = 32768, M = 100 M_\odot, r_v = 3.5$pc) we observe a merger within the simulated time ($\simeq$ 100Myr), and in what follows we will focus on describing the detailed dynamics of this cluster. We acknowledge that as the main focus of this study is the dynamical formation and evolution of binaries, and higher order N-tuples, with the IMBH as the primary companion, all cluster particles are solely characterized by their mass and no stellar evolution is included in these simulations.

2.3 Results

The simulated globular cluster was initialised with the IMBH at rest at the center while the remaining stars and BHs follows a King model. Figure 2.1 shows the position of the IMBH and a subset of BH particles, and their subsequent movement within the cluster, relative to the center of mass of the entire cluster. This subset of the BH population were those that were ejected from the cluster during the simulation. Although the IMBH is initially at rest at the cluster center of mass, it quickly experiences significant Brownian motion within a sphere of radius ~ 0.1pc around the center of mass. The typical distance wandered by the IMBH in the core is larger than the radius of influence of the IMBH.

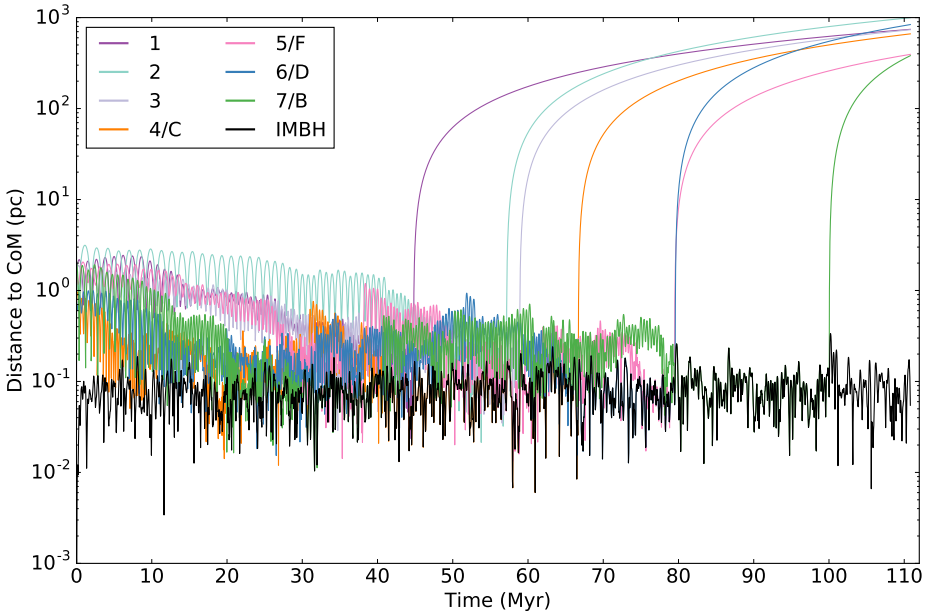

Figure 2.1 Time evolution of the distance of the IMBH (in black) to the center of mass (CoM) of the entire cluster. Note how the IMBH is wandering throughout the simulation within a central region of extent $\lesssim 0.1$pc around the cluster CoM. Also shown (in colour) are the BHs that were ejected from the cluster and the corresponding time of ejection. BHs for which we have assigned both a numerical and alphabetical index were bound to the IMBH before being ejected from the cluster. The evolution of the orbits of these BHs are also shown in Figure 2.2.

Shifting the focus from the global dynamical behaviour within the cluster, Figure 2.2 displays the time evolution of the relative distance to the IMBH of those BHs which experienced close encounters with the IMBH at some point of the simulation. In this figure we see that while the IMBH is interacting only weakly with its surroundings at the start of the simulation, after ~ 3 Myrs it forms a wide binary with a stellar particle, and after ~ 25 Myrs the binary companions are BHs, consistent with the expected mass segregation in this cluster. By comparing the ejected BHs between Figure 2.1 and Figure 2.2 it is clear that after the first few ejected BHs (which were driven by their initially relatively high kinetic energy and interactions with other cluster members) and following the formation of the IMBH-BH binary, all subsequent ejections are driven by interactions with the IMBH-BH binary. These interactions lead to the frequent substitution of the IMBH binary companion, with three out of the five observed substitution events

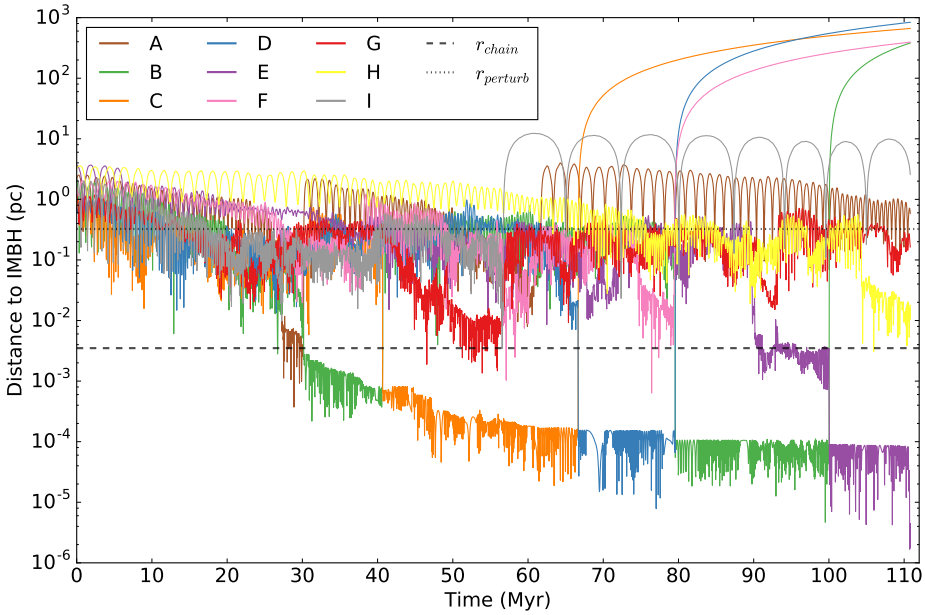

Figure 2.2 Distance to the IMBH versus time for BHs which at any point in the simulation came within a sphere of 4 mpc around the IMBH. Within the first 3 Myrs the IMBH aquires a binary companion, at first a stellar particle which is quickly substituted for a BH companion at $\sim$ 25 Myrs, in this case BH_A, forming a wide binary. Through interactions with other objects embedded in the cluster potential this binary is hardened. The IMBH–BH binary undergoes many companion substitutions, often while in hierarchical N-tuples, resulting in both later recaptures (BH_B) and ejections from the cluster ($\mathrm{BH}_{C,D,B}$). The dashed black line marks the transition distance r_{chain} below which the dynamics are treated by AR-CHAIN under the gravitational influence of all perturbing particles within the region represented by the dotted black line ($r_{perturb}$).

leading to the former companion being ejected from the cluster. The remaining two were returned to the cluster BH population, where one BH (BH_B in Figure 2.1 and Figure 2.2) was later recaptured by the IMBH. Figure 2.2 also shows the transient 3-body interactions, such as the ejection of BH_F, and their effectiveness in the continued hardening of the IMBH-BH binary.

The time evolution of this binary is most clearly visualized in terms of its orbital parameters where Figure 2.3 shows the IMBH-BH binary semi-major axis.[1]

[1]The semi-major axes and eccentricities were computed using the post-Newtonian formalism given in Equation (3.6) of Damour and Deruelle [71].

Once the IMBH captures a stellar-mass BH companion, the IMBH–BH binary is hardened by 3-body interactions. The hardening of the binary is clearly visible in Figure 2.3 as the semi-major axis of the IMBH-BH binary decreases monotonically, with the jumps in semi-major axis being signs of energetic 3-body interactions. While Figure 2.2 only shows the BH interactions, there are also a multitude of close encounters with stars carrying energy away from the IMBHâĂŞBH binary. The majority (~ 150) of these were ejected from the cluster, with moderate to high final velocities ($v \lesssim 250\text{km s}^{-1}$), with the remainder being returned to the cluster stellar population distributing energy throughout the cluster.

The binary hardens through 3-body interactions on the typical timescale [e.g., 196, 151]

$$\tau_{\text{harden}} \simeq 10^8 \left(\frac{10M_\odot}{m_*}\right)\left(\frac{v}{10\text{km s}^{-1}}\right)\left(\frac{10^{5.5}\text{pc}^{-3}}{n}\right)\left(\frac{0.05\text{AU}}{a_i}\right)\text{yr} \,, \tag{2.3}$$

where m_* is the interloper mass, v is the velocity dispersion in the cluster, n is the number density of stars and BHs in the cluster center, and a_i is the binary's semi-major axis.

As the binary hardens, after $\simeq$ 110Myr, the time to the next interaction drops below the GW driven merger timescale which, in the limit of large binary eccentricities, is approximated by [184]

$$\tau_{\text{merge}} \simeq 3 \times 10^7 \left(\frac{10^5 M_\odot^3}{M^2 m}\right)\left(\frac{a_i}{0.05\text{AU}}\right)^4 (1-e_i^2)^{7/2}\text{yr} \,, \tag{2.4}$$

where e_i is the IMBH-BH binary eccentricity, M is the IMBH mass, and m is the mass of its BH companion. The semi-major axis a_{GW} at which the evolution of the binary eccentricity starts to be dominated by GW radiation, and no longer governed by 3-body interactions, can be found by setting

$$\tau_{\text{merge}} = (1-e_i^2)\tau_{\text{harden}} \,. \tag{2.5}$$

where the factor of $(1-e_i^2)$ comes from the fact that it is diffusion of angular momentum, and not energy, which initiates the GW dominated phase [c.f. Eq 62

in 159]. This in turn gives

$$a_{\rm GW} \simeq \frac{0.15}{\sqrt{1-e_i^2}}{\rm AU}\,. \tag{2.6}$$

At separations below $a_{\rm GW}$ the evolution of the binary is dominated by energy loss due to GW emission. Mandel et al. [151] computed the total time to IMBH–BH coalescence by summing the hardening time to the last interaction with the subsequent merger timescale under the assumption that the last interaction is likely to leave the binary with an eccentricity of $\simeq 0.98$ [101]. However, as shown in what follows, even higher eccentricities can be reached during the complex 3-body interactions, possibly reducing the merger timescale [38, 204].

Figure 2.4 shows the evolution of the binary eccentricity where the inclination of outer to inner binary when the binary is part of a triple system (ι_0) is shown in Figure 2.5. The complex dynamical structure of the surroundings of the binary, including both stellar and BH interactions, is evident in Figure 2.4 where large amplitude variations of the IMBH-BH binary eccentricity are observed. The evolution of e_i and ι_0 is driven both by transient passes and by longer duration LK and post-Newtonian effects.

The eccentricity oscillations in hierarchical triple systems can potentially drive up the eccentricity of the inner binary to very high values, possibly leading to faster GW driven mergers [166, 1, 38]. The timescale for a full oscillation in eccentricity is given as

$$\mathrm{T}_{LK} \simeq \frac{P_i}{2\pi}\frac{M+m}{m_o}\left(\frac{a_o}{a_i}\right)^3 (1-e_o^2)^{3/2} \tag{2.7}$$

where a_i, a_o are the semi-major axes of the inner and outer binary respectively (within the hierarchical triple system), e_o is the eccentricity of the outer orbit, m_0 is the mass of the tertiary BH, and $P_i = 2\pi\sqrt{a_i^3/G(M+m)}$ is the orbital period of the inner binary [116]. We also define here a dimensionless angular momentum, as the angular momentum of the binary divided by the angular momentum of a circular orbit with the same semi-major axis: $\ell_i = \sqrt{1-e_i^2}$; this is a useful quantity when discussing LK oscillations, as they do not affect the orbital energy. The timescale over which the inner binary changes the value of

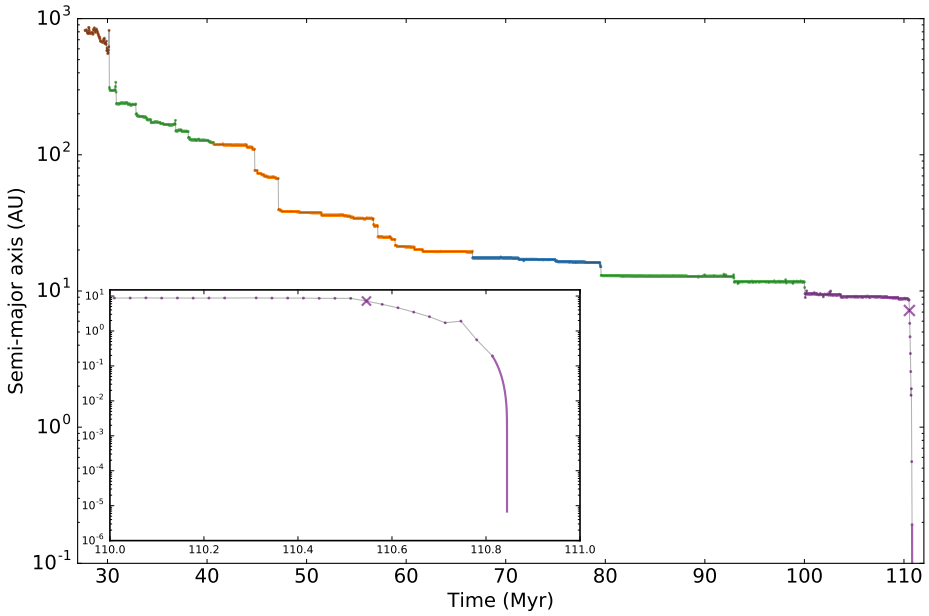

Figure 2.3 A stable binary consisting of an IMBH and another BH will harden over time and lose energy to its surroundings, manifested by the shrinking of the binary's semi-major axis. The colours match Figure 2.2 to highlight the substitution of the binary companions. At the end of the simulation the IMBH, through external perturbation by BH_H, is set on a trajectory towards a merger with its binary companion BH_E while still inside the cluster. The point where GW emission becomes dominant in the orbital evolution (see Equation 2.6) is marked by a purple $\times$. At the end of the simulation the binary orbit is evolved until merger according to Peters [184] marked by the solid purple line, this is further highlighted in the inset figure showing the last Myr of the binary before merger.

its angular momentum by order of itself is then [57, 36]

$$\tau_{LK} \equiv \left| \frac{1}{\ell_i} \frac{d\ell_i}{dt} \right|^{-1}_{LK} \simeq \mathrm{T}_{LK} \sqrt{1 - e_i^2} \tag{2.8}$$

directly related to the period of the LK oscillation.

At the quadrupole level of approximation and in the test particle limit, for an orbit librating around the argument of periapsis $\omega_i = \pi/2$ the maximum (ℓ_+) and minimum (ℓ_-) angular momenta during a LK cycle are related through the

equation [e.g., 158]

$$\ell_+\ell_- = \sqrt{\frac{5}{3}}\ell_z. \tag{2.9}$$

In the previous expression $\ell_z = \ell_i \cos\iota_0$ is a conserved quantity for an initial orbital inclination ι_0 in the quadrupolar limit. From Equation 2.9, and from the conservation of ℓ_z one finds that the maximum eccentricity that can be attained during a LK cycle is simply $e_{max} = \sqrt{1-(5/3)\cos^2\iota_0}$ [121].

Post-Newtonian corrections to the orbital dynamics can affect the binary on similar timescales as τ_{LK}, where the most prominent effect would be the 1pN Schwarzschild precession (SP) of the argument of periapsis ω_i. To lowest order, the timescale associated with SP is

$$\tau_{SP} \equiv \left|\frac{1}{\pi}\frac{d\omega_i}{dt}\right|^{-1}_{SP} \simeq \frac{P_i}{6}\frac{a_i}{r_g}(1-e_i^2) \tag{2.10}$$

with $r_g = G(M+m)/c^2$. When SP is considered, Equation 2.9 becomes [37]:

$$\ell_+^2\ell_-^2 = \frac{5}{3}\ell_z^2 + \frac{k}{3}\left(\frac{\ell_+ - \ell_-}{\ell_+^2 - \ell_-^2}\right)\ell_+\ell_-, \tag{2.11}$$

with

$$k = 8\frac{M}{m}\frac{r_g a_o^3}{a_i^4}\left(1-e_o^2\right)^{3/2} \quad . \tag{2.12}$$

This shows that SP effects can suppress the phase space available for libration for systems with $\tau_{SP} < \tau_{LK}$, reducing the maximum eccentricity attained during a LK cycle. In fact, from Equation 2.11, given that the second term on the right hand side of the equation is always positive, we see that for a given ℓ_+ SP will lead to an increase of ℓ_-.

By setting $\tau_{LK} = \tau_{SP}$ we find the critical angular momentum

$$\ell_{SP} \sim \frac{r_g}{a_i}\frac{M+m}{m_o}\left(\frac{a_o}{a_i}\right)^3 \tag{2.13}$$

which in turn can be represented as an eccentricity boundary $e_{SP} = \sqrt{1-\ell_{SP}^2}$ to the eccentricities within reach of LK oscillations. SP will dominate the orbital evolution of the inner binary at eccentricities larger than e_{SP}, thus quenching the

possibility of eccentricity oscillations caused by LK resonance. When $\ell_{SP} \geq 1$, then SP will dominate over the torque from the outer tertiary BH for any value of e_i and LK oscillations are expected to be fully suppressed. In Figure 2.4 we show when this happens using a solid red line at $\ell_{SP} = 1$. As expected, no LK oscillations occur when $\ell_{SP} \gtrsim 1$. In Figure 2.4 the e_{SP} boundary is shown only when there is a hierarchical triple system present, with the IMBH-BH binary at its center. During the periods of active LK oscillations, for example between $\sim 90 - 100$ Myr, it is clear that the eccentricity of the IMBH-BH binary never exceeds the e_{SP} boundary. This is further evidence that SP plays a fundamental role in the dynamical evolution of the IMBH-BH binary in our simulations. The detailed interaction between LK and SP dynamical effects is also discussed by Naoz et al. [174] who find that, assuming Newtonian dynamics to octupolar order with an added 1pN (only) correction term, SP in hierarchical triples can excite eccentricity rather than suppress it for $\tau_{SP} \sim \tau_{LK}$. While qualitatively similar behaviour can be observed in our simulation, it is difficult to distinguish effects like this from other mechanisms subdominant to the LK oscillations (e.g. the hierarchical mass ratio configuration, stellar interlopers and the perturbing cluster potential) without further investigation.

In addition to LK suppression from relativistic precession, the presence of strong Newtonian precession, induced by the IMBH–BH binary existing within a dynamical cluster, would have similar effects on the binary orbital evolution. We find the classical precession to be negligible compared to SP for the periods when the IMBH–BH binary is in a hierarchical triple, and thus have no effect on the LK suppression caused by precession of the IMBH–BH orbit.

Between $\sim 90 - 93$ Myr we find that the IMBH–BH binary is part of a hierarchical quadruple BH (IMBH, BH_B, BH_E, BH_F), with a resolved two-level LK oscillation. As discussed by Hamers et al. [102], as the individual τ_{LK} for the two LK systems are comparable, this induces complex LK oscillations in the IMBH–BH binary, further enhancing the transfer of angular momentum away from it. This is most clearly exemplified by the eccentricity: the expected maximum eccentricity $e_{max} \simeq 0.3$ from $\iota_0 = 43.1°$ at 90 Myr is substantially smaller than the eccentricities achieved during the existence of the quadruple BH. It is also interesting to note that the two LK timescales associated with the quadruple are

both below the corresponding τ_{SP} for the inner binary as well as the empirical timescale for the precession of ω_i induced by the presence of the quadruple within the stellar cluster. Eventually at $\simeq 93$ Myr the quadruple system is disrupted by the removal of the outermost BH. At $93 - 100$Myr of evolution the eccentricity of the IMBH-BH binary clearly undergoes large-amplitude LK oscillations as expected given the high mutual inclination of the outer to inner orbit ($\iota_0 = 78.5°$) at this time.

While the observed oscillations in eccentricity and inclination of the IMBH triple system show all signs of being caused by the LK mechanism, it is important to keep in mind that "pure" LK oscillations assume an isolated 3-body system. Here we are able to observe (for the first time) this mechanism acting on a triple system embedded in a dynamically evolving stellar cluster while also accounting for relativistic corrections to the motion.

Also interesting are the regions where $e_{SP} = 0$, or equivalently $\ell_{SP} \geq 1$. Here the SP is dominating the IMBH-BH binary to such a degree that no eccentricity oscillations driven by LK are possible. We find that the inclination of the IMBH-BH binary relative to the outer BH orbit evolves stochastically, attaining at times values near 40° which based on Equation 2.9 should lead to LK eccentricity oscillations with a period $\simeq 5 \times 10^6$ years following Equation 2.7.

Contrary to this, during the last ~ 10 Myr the IMBH–BH binary appears to be "frozen" at high e_i with SP suppressing any eccentricity reduction apart from the higher pN-order emission of GWs. After a strong interaction with a stellar interloper, which in turn is ejected from the cluster at ~ 120km s^{-1}, the loss of energy and angular momentum through GWs determines the ultimate fate of the binary, leading to its merger $\sim 300,000$ years later (see Figure 2.6).

During the initial GW-dominated phase the binary experiences a small number of 3-body interactions with stellar interlopers, which are the cause of the "spikes" visible in Figure 2.6. However, these interactions do not disrupt the binary inspiral.

A highly eccentric binary emits a broad spectrum of gravitational radiation during each periapsis passage. We identify the frequency of the harmonic con-

taining the maximal gravitational radiation as [252]:

$$f_{\rm GW} = \frac{\sqrt{G(M+m)}}{\pi} \frac{(1+e_i)^{1.1954}}{[a_i\,(1-e_i^2)]^{1.5}}\ ; \tag{2.14}$$

this is the GW frequency plotted in Figure 2.6.

The binary spends $\simeq 300,000$ years in the eLISA sensitive frequency window, which spans ($0.001{\rm Hz} \lesssim {\rm f_{GW}} \lesssim 1{\rm Hz}$). Meanwhile, the last 6 seconds of the inspiral, followed by the merger and subsequent ringdown of the resulting IMBH, occur in theGW spectrum observable by Advanced LIGO ($f_{\rm GW} \gtrsim 10{\rm Hz}$). As suggested by Amaro-Seoane and Santamaría [35] for IMBH–IMBH binaries and Abbott et al. [19], Sesana [212] for binary BH systems similar to the detected GW150914 [22], this type of IMBH–BH coalescences represents a class of GW sources potentially observable in both space- and ground-based detectors, providing an opportunity for long-term detailed studies of both their formation environments and probes of general relativity itself. We discuss the near-term prospects of detecting such binary mergers with Advanced LIGO in the following section.

To further verify the importance of the inclusion of the pN effects in our models, the simulation was restarted ~ 1 Myr before the merger, removing all pN terms from the equations of motion. As shown by the light green samples in the upper inset of Figure 2.4, removing pN terms results in eccentricity oscillations without, of course, a GW induced merger. During these oscillations the IMBH remains in a bound triple system (IMBH, $\rm BH_{\it E}$, $\rm BH_{\it H}$) in which SP would have been the dominant dynamical factor, completely removing the possibility for LK oscillations.

In addition, we performed one simulation, also started ~ 1 Myr before the merger, where the chain regularization was disabled. In this simulation the surrounding N-body integrator could not accurately follow the very hard IMBH-BH binary; this had the effect of significantly slowing down the simulation while no longer adhering to the conservation of total energy within the cluster. This loss of $\frac{\Delta E}{E} \sim 0.01$ per time-step $\Delta t = 67$kyr accumulates as the simulation progresses, to be compared with $\frac{\Delta E}{E} \sim 10^{-4}$ per time-step when including the chain regulariza-

tion. These results further demonstrate the importance of using a high accuracy integrator like AR-CHAIN in order to study the evolution of IMBHs in cluster simulations.

2.4 Discussion

Gravitational waves from intermediate mass-ratio coalescences are observable with both a future space-based GW detector [84] and the advanced network of ground-based detectors [106, 27]. The SP-induced freezing of the IMBH–BH orbit at high eccentricities will be conducive for the production of a merging binary, as efficient GW emission is then possible for larger binary semi-major axes as compared to a circular system [184, 213]. The observed binary inspiral is in the eLISA sensitivity band throughout the circularizing phase. However, detection and parameter estimation at very high eccentricities could prove problematic without high-accuracy eccentric templates for matched filtering the bursts of radiation expected during the few periapsis passages over the lifetime of a space-borne mission [34, 190, 125, 50]. Both detection and parameter estimation would be more amenable to existing techniques later in the orbital evolution [118, 236, 223, 167, 175], for $e_i \lesssim 0.1$ in Figure 2.6, and with only ten years from $e_i = 0.1$ until merger for this system a co-observing campaign together with ground-based detectors, where the system is effectively fully circularized, would be possible.

As discussed by Sesana [212] and Vitale [249] in relation to binary BHs similar to GW150914, the extended observation in eLISA would provide excellent constraints on the binary masses, sky position and coalescence time with the observational gap of $1\text{Hz} \leq \text{f}_{\text{GW}} \leq 10\text{Hz}$ between eLISA and Advanced LIGO only spanning ~ 1 hour. Note that the exact observational gap depends on the distance to the source, corresponding to its observed signal-to-noise ratio, and therefore determining the frequency band where the signal will be below the detector noise floor. This advance information would however allow for optimization of the ground-based detector network, both in terms of active tuning of the detector sensitivity, operational scheduling and the analysis pipelines, as well as

pre-pointing of electromagnetic follow-up telescopes[1]. For the remainder of this section we will focus on detectability and rates for ground-based detectors alone, primarily motivated by the lack of a space-based detector for at least the next decade.

In Figure 2.7 we show the sensitivity of a network of ground-based detectors to GWs from an IMBH–BH coalescence with non-spinning components with a mass ratio of 10:1, as a function of IMBH mass.

The top panel of Figure 2.7 shows the horizon distance d_H, which is the luminosity distance at which GWs from a face-on overhead binary would be detected at a signal-to-noise ratio of 8 by a single detector with the sensitivity of Advanced LIGO; the corresponding horizon redshift z_H is shown on the right vertical axis. This signal-to-noise ratio is used as an approximation for sensitivity by the full network [17, 23]; the actual sensitivity depends on the network configuration, data quality, and signal duration. We use the noise power spectral density (PSD) of H1 (the LIGO detector in Hanford, WA) during the S6 science run [curve labeled '2010', 137], the measured noise PSD of H1 during the 2015 observing run O1 ['2015–2016', 138], low-end predictions for Advanced LIGO noise PSD for the later stages of detector commissioning ['2017–2018', O3 configuration of 26], and for design sensitivity runs in the zero detuning, high laser power configuration ['2019+', 136]. We use circular effective one-body waveforms calibrated to numerical relativity for signal-to-noise-ratio calculations [225].

The bottom panel of Figure 2.7 shows the surveyed detection-weighted comoving volume $\overline{V}_c$

$$\overline{V}_c = \int_0^\infty \frac{dV_c}{dz} f_d(z) \frac{1}{1+z} dz \,, \tag{2.15}$$

where $\frac{dV_c}{dz}$ is computed using the Planck [186] cosmology, $f_d(z)$ is the probability that a binary with the given source-frame masses at redshift z is louder than the signal-to-noise ratio threshold of 8 (integrated over isotropically distributed sky locations and orientations), and the last factor corrects for the difference in source and observer clocks. With this definition, $\mathcal{R}\overline{V}_c T$ yields the expected number of detections during an observing run with (at least double-coincident) duration T

[1]No electromagnetic counterpart is expected from the merger of an IMBH–BH binary in the standard scenario [e.g., 144], but see Connaughton et al. [69]

assuming a constant merger rate $\mathcal{R}$ per unit comoving volume per unit source time.

Intermediate mass-ratio coalescences can be observed to a horizon distance of ~ 1 Gpc during the O1 science run, and a horizon redshift $z \sim 0.6$ at full design sensitivity. Figure 2.7 assumes a 10:1 mass ratio. It can be roughly rescaled to other mass ratios by noting that, for a fixed IMBH mass, the signal-to-noise ratio at a given distance, and hence the horizon distance, will scale as $\sqrt{m/M}$ when the signal is inspiral-dominated, and as m/M when the signal is ringdown-dominated. The transition between the two regimes occurs at $M + m \sim 200\ M_\odot$ at Advanced LIGO design sensitivity [see Fig. 9 of 110, which also discusses inference on the parameters of coalescences of intermediate mass-ratio binaries]. As a comparison, if the BHs in GW150914 (both BHs in the initial binary and the merger product) had been the lower mass member of a 10:1 mass ratio IMBH–BH binary, all signals would be ringdown-dominated [22]. The same is valid for the marginally astrophysically significant event LVT151012 [23] where only the lower mass BH from the initial binary would produce an inspiral-dominated signal.

The IMBH–BH coalescence rate is highly uncertain. Our simulations suggest that around one IMBH–BH merger per ten globular clusters is probable in the first $\sim$ hundred million years of the lifetime of a cluster hosting a suitable IMBH. The merger product may well be ejected from the cluster by the recoil kick from asymmetric GW emission in the last few pre-merger orbits. Assuming the IMBH is not spinning, the kick velocity for a 10:1 mass ratio coalescence is $\simeq 60\text{km s}^{-1}$ [96], comparable to the typical $\sim 50\text{km s}^{-1}$ escape velocity from a globular cluster. If so, at most $\sim$ one IMBH–BH merger would happen per cluster before the IMBH is ejected.

The remaining 11 simulations followed a similar initial dynamical evolution to the cluster discussed in detail in this chapter, with all IMBHs forming a binary with a BH within $\lesssim 20$Myr. These binaries are hardened by 3-body interactions and at the final time of the simulation the binaries had estimated $\tau_{\rm merge} \sim$ Hubble time. These estimates do not take into account either further 3-body interactions, SP or LK effects and should be seen as upper limits for a time to merger from GW emission. It should however be noted that in two of the clusters with small r_v ($r_v = 0.35\text{pc}, \text{M} = (50, 100)\text{M}_\odot$) the IMBH–BH binary underwent periods

of rapid 3-body interactions which led to the ejection of the IMBH–BH binary (without disrupting it) from the cluster.

Even if the merger product is retained, there is a trivial upper limit on the number of mergers per cluster in the Advanced LIGO sensitive frequency band. By the time the IMBH grows beyond several hundred solar masses (see Figure 2.7), the sensitivity drops significantly; hence, only $\sim$ 30 IMBH–BH per cluster are observable.

Therefore, the IMBH–BH coalescence rate per suitable cluster may vary between 1 and 30 mergers over the cluster's $\sim$ 10 Gyr lifetime, or 0.1–3 mergers Gyr^{-1}. The space density of globular clusters is $\sim 3\ \mathrm{Mpc}^{-3}$ [189]. Following Mandel et al. [151], we will parametrize the fraction of suitable globular clusters (those with the right IMBH mass and central density) by f. Then the total merger rate is in the range $R \in [0.03(f/0.1), (f/0.1)]\ \mathrm{Gpc}^{-3}\ \mathrm{yr}^{-1}$. Multiplying this by the surveyed detection-weighted comoving volume, we may expect $\sim$ 0.1—5 $\times(f/0.1)$ detections per year at full sensitivity. In the near term, 0.01—1 $\times(f/0.1)$ detections may be possible during the upcoming O2 6-month observing run, assuming a $\sim 50\%$ coincident duty cycle.[1]

This calculation may well be optimistic. It assumed a constant merger rate over the cluster lifetime; however, most local globular clusters are old [e.g., 132], and mergers are in general more likely early in the cluster lifetime[2]. Therefore, most mergers may happen at high redshift, where they are unlikely to be detectable. Finally, the fiducial choice $f = 0.1$ is fairly arbitrary; much lower values, including $f = 0$, are possible. On the other hand, if IMBHs are spinning, prograde inspirals could yield higher signal-to-noise ratios, and the detection volume and rate would increase even after averaging over isotropic inspiral orbits [149].

We have also looked for evidence of possible tidal disruptions of stars by the IMBH [see 146, for a recent analysis]. Our problem set up is not ideal for this

[1] These rates should be considered in relation to the upper limits on the rate of binary IMBH coalescences from LIGO–Virgo observations, which are $\geq \mathcal{O}(10^3)$ higher depending on the IMBH masses considered [10].

[2] Keep in mind the non-mergers observed in the 11 simulations performed in preparation for this chapter, but also the fact that each eventual merger carries a non-negligeble probability of ejection of the IMBH.

investigation, since we have only two stellar types in addition to the IMBH: one solar mass "stars" and ten solar mass "black holes". None of the one-solar-mass stars in our simulation approach the IMBH within the tidal disruption radius. However, if we consider the black holes as proxies for evolving stars, we find that a few would approach within the IMBH tidal disruption radius while in the giant phase of their evolution. Given the gradual hardening of the innermost binary, it is likely that the nominal tidal disruption radius would be reached through stellar evolution rather than a dynamically-driven encounter. Hence, rather than transient tidal disruptions, we may expect to see Roche lobe overflows, perhaps leading to ultraluminous X-ray binaries such as ESO 243-49 HLX-1 [86, 95]. In the case of stellar companions additional sources of apsidal precession (for example, precession due to tidal and rotational bulges) may arise and quench LK oscillations similarly to SP as discussed above.

The capability of our simulation tracking both the complex dynamical features and the merger stands in contrast with previous work such as Leigh et al. [134], who did not include any pN effects and were thus unable to observe the quenching of LK oscillations due to SP. This could lead to the production of IMBH-BH binaries with artificially long lifetimes as they were unable to merge by the emission of GWs. This issue was partly addressed by MacLeod et al. [146], who included GW mergers following Peters [184]; however, the interplay of LK effects with SP (and tides in the case of stellar companions) would likely affect their merger rate estimates. Finally, neither the N-body simulations in Leigh et al. [134], MacLeod et al. [146] nor in this work included any population of primordial binaries [but see 113, 239, 238], and while binaries which does not include the IMBH can form these would not be specifically tracked. The presence of primordial binary BHs in combination with an IMBH has been shown to affect the retention of BHs in the cluster as well as the evolution of the fraction of BHs in binaries [185, 239, 134], and would thus require a more careful treatment in future studies.

2.5 Conclusion

We have, in a simulation, observed a merger of a $100M_\odot$ IMBH and a $10M_\odot$ BH within a globular cluster as part of the first simulation campaign accounting for post-Newtonian dynamics in the region around the IMBH. This has provided insight into the competitive interplay between pN effects and LK eccentricity oscillations in hierarchical systems as a mechanism for producing and hardening an IMBH–BH binary. We have observed suppression of LK oscillations caused by the pN Schwarzschild precession of the IMBH–BH binary giving clear evidence for the necessity of including pN dynamics in future simulations of globular clusters to fully capture all relevant dynamical effects leading to the formation, evolution and merger of an IMBH–BH binary. This is especially relevant at the end of our simulation, where fast relativistic precession of the IMBH–BH binary freezes its orbit at high eccentricities, thus facilitating the onset of an inspiraling trajectory towards a merger.

Future extensions to this work will include a larger spectrum of masses (both for the IMBH and the surrounding cluster particles), longer simulation times (requiring further optimization of the code) and additional physical effects (e.g., stellar evolution models, population of primordial binaries and external tidal fields). We have also commented on the detectability of gravitational waves emitted from an IMBH-BH merger by both space-based and ground-based observatories, with a possible detection within the next decade.

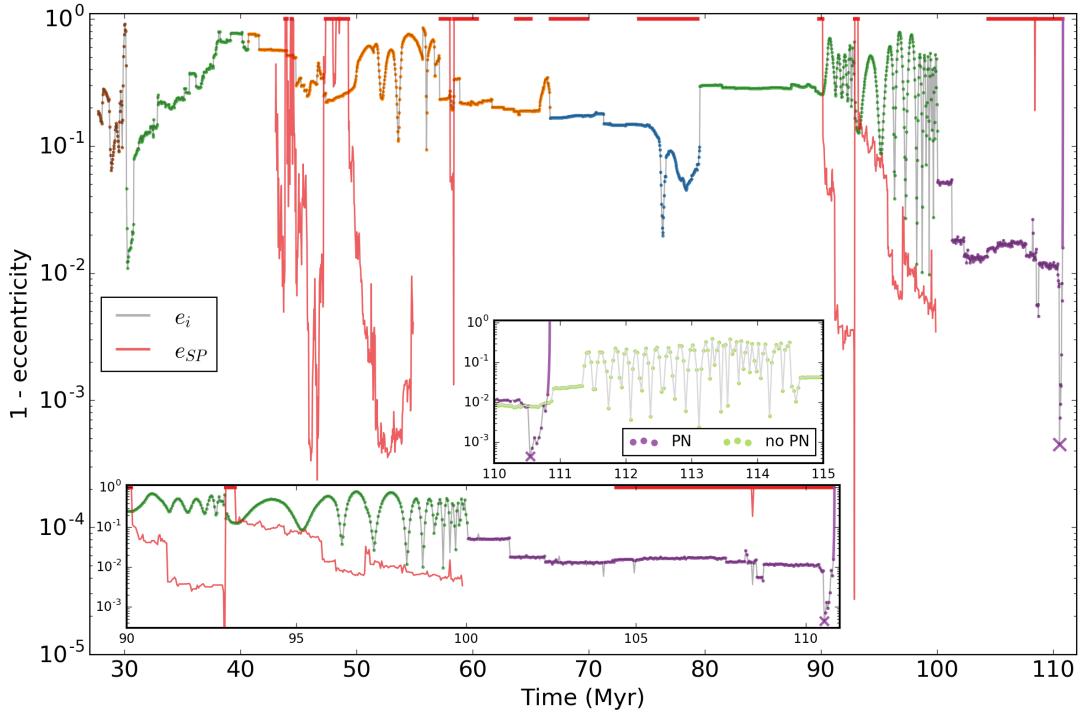

Figure 2.4 Evolution of the IMBH-BH binary eccentricity. The colours of e_i match those of Figure 2.2 to highlight the many substitutions of the binary companions. The figure shows clear evidence for both transient 3-body interactions as well as longer timescale LK oscillations. For the majority of the binary's presence in a hierarchical N-tuple LK effects are suppressed by the SP of the inner binary orbit. The precession is represented here as an effective eccentricity boundary e_{SP} above which LK oscillations are suppressed (corresponding to *below* the e_{SP} line in this figure). The bottom inset shows the last $\sim$ 20 Myr exhibiting LK oscillations, bounded by e_{SP}, in a quadruple and later a triple BH system ended by the substitution of the IMBH binary companion. This last binary configuration is frozen at high e_i, suppressed by SP and later merged. The point where the binary evolution is dominated by GW emission is marked by a purple $\times$. At the end of the simulation the binary orbit is evolved using the formula of Peters [184] marked by the solid purple line. To further highlight the importance of the post-Newtonian dynamics the upper inset also includes a simulation (presented in light green) started at $\sim$ 1 Myr before the observed merger, but using only Newtonian dynamics. This provides evidence for the importance of pN dynamics through the absence of the merger as well as the clear eccentricity oscillations in a triple system where SP would have provided complete LK suppression.

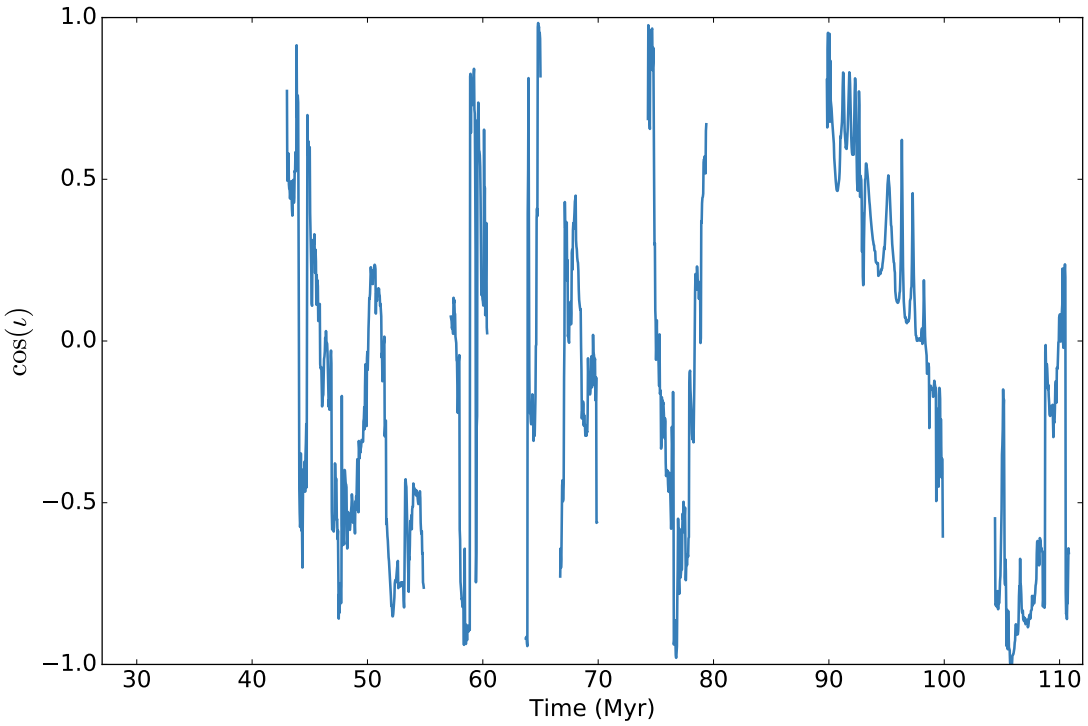

Figure 2.5 Evolution of the inclination ι_0 between the inner (IMBH–BH binary) and outer orbits for the times when the IMBH exists in a bound triple system.

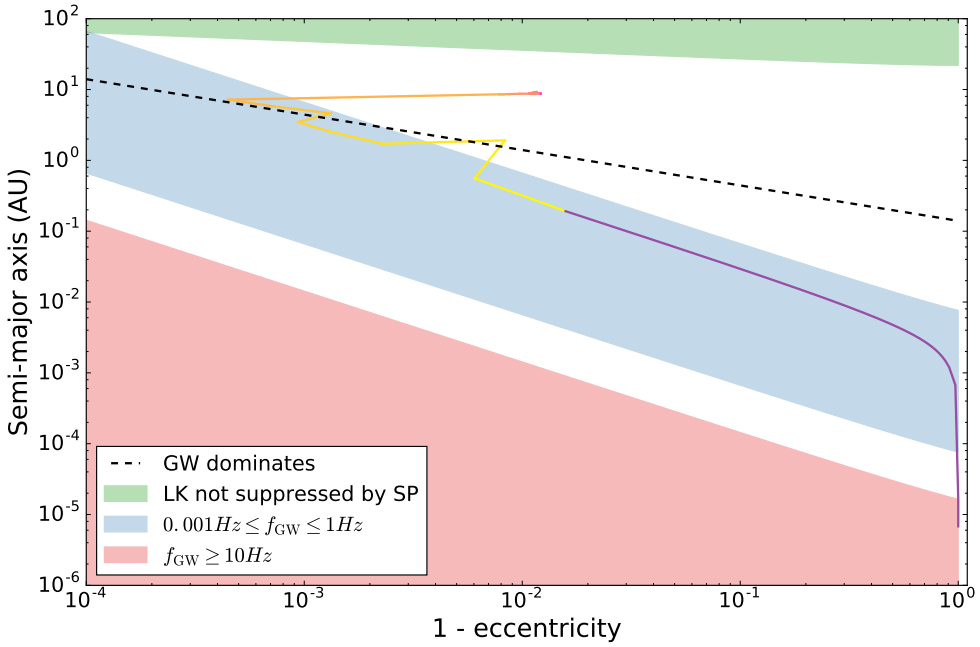

Figure 2.6 As the IMBH–BH binary evolves during its final Myr (time increases from red to yellow) it is frozen at very high eccentricities due to the suppression of LK oscillations by the SP of the IMBH–BH binary. The red region indicates where this suppression would be absent. The presence of a stable triple system, as indicated in Figure 2.2, causes perturbations of the IMBH orbit from both the tertiary BH_H and additional stellar interlopers. One of the stellar perturbations bring the three objects so close together that the IMBH–BH binary orbital evolution becomes dominated by emission of GWs. Additionally, this ejects the stellar interloper at a velocity $\sim$ 120km s^{-1}. GW emission dominates below the dashed black line, given by Equation 2.6; in this regime merger through the emission of GWs will occur before the next 3-body interaction can significantly alter the IMBH–BH binary eccentricity, and thus its evolutionary timescale (c.f. the interloper which initiated the merger trajectory). Much of the GW dominated evolution occurs at GW frequencies observable by eLISA, as indicated by the blue region. As the IMBH–BH binary evolves along its merger trajectory there are still a small number of minor three body encounters with stellar interlopers passing within a few semi-major axes of the binary CoM; these interactions are the cause of the "spikes" visible in the merger trajectory. These interactions are consistent with the timescales given in Equation 2.3 and Equation 2.4, which predict that the last interaction before merger should occur when this system has a semi-major axis of $\sim$ 1 AU. At the end of the simulation the binary's orbit is evolved to merger, within the Advanced LIGO sensitive band (marked by the green region), according to Peters [184], as shown by the purple line.

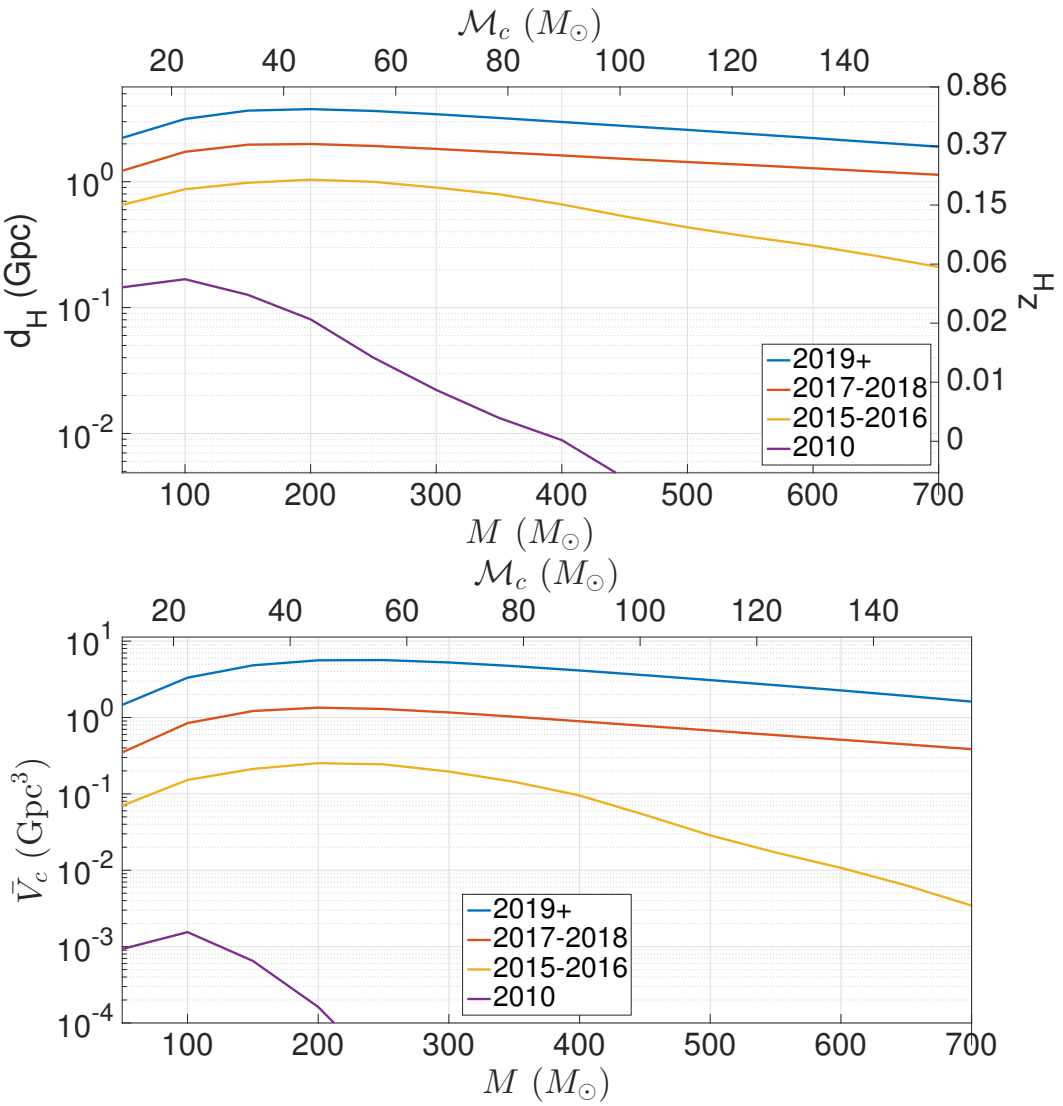

Figure 2.7 Top: Horizon distance (left axis) and horizon redshift (right axis) as a function of IMBH mass for IMBH–BH coalescences with non-spinning components with a 10:1 mass ratio, for different detector sensitivities (see text). Bottom: Detection-weighted sensitive comoving volume, Equation 2.15; when multiplied by a constant merger rate per unit comoving volume per unit source time, this yields a detection rate.

Chapter 3

Inference on gravitational waves from coalescences of stellar-mass compact objects and intermediate-mass black holes

This chapter is adapted from a paper by *Carl-Johan Haster*, Zhilu Wang, Christopher P. L. Berry, Simon Stevenson, John Veitch and Ilya Mandel. My contribution to this work was to *(i)* design the initial parameters of this study, *(ii)* aid Zhilu Wang (a summer student in the group) to run the simulations, *(iii)* lead the post-processing and collating of the results, *(iv)* write the paper. This paper is published in MNRAS [110] and has arXiv number 1511.01431.

3.1 Introduction

The Advanced LIGO [aLIGO; 13] gravitational-wave (GW) detectors began their first observing run on 12 September 2015 as discussed in chapter 1; the Advanced Virgo [AdV; 28] GW detector is expected to commence scientific observation in 2016 [26]. One of the key sources for the advanced-era detectors are compact binary coalescences [CBCs; 17, section 1.1 and subsection 1.2.2], the inspiral and merger of binary systems including both neutron-star (NS) and black-hole (BH)

companions across a large mass spectrum.

As discussed in section 2.1 intermediate mass black holes (IMBHs) fill the gap in the continuum between stellar-mass BHs and supermassive BHs, potentially representing an early stage in the evolution of supermassive BHs [165, 99]. At present, the best evidence for their existence comes from observations of ultraluminous X-ray sources [88, 182].

IMBHs of a few hundred solar masses in a coalescing binary are a potential source of GWs for the advanced generation of ground-based detectors. If the IMBH's companion is another IMBH, the system is referred to as an IMBH binary (IMBHB). If its companion is stellar mass, then the system undergoes an intermediate mass-ratio coalescence (IMRAC). These are often also referred to as intermediate-mass-ratio inspirals (IMRIs);[1] however, we prefer IMRAC to highlight the importance of the entire coalescence, including the merger and ringdown phases in addition to the inspiral, to the detection and analysis of these high-mass systems [220].

IMRACs are most likely to be found in the dense cores of globular clusters [134, 146]. They can form through a range of mechanisms, including hardening of an existing binary, through either three-body interactions or Kozai oscillations as part of a hierarchical system, as well as through direct or tidal capture [151]. As a consequence of mass segregation in globular clusters, the stellar-mass companion to the IMBH will change throughout the evolutionary history of the cluster [146]. Soon after the formation of the cluster, the companion will most likely be a stellar-mass BH, but for older clusters it could be a NS if the stellar-mass BH population has been depleted by mergers and dynamical ejections [94, 240, 170]. Consequently, there is a large variation in the possible mass ratios of detectable binaries.

The resulting IMRACs are estimated to have become largely circularized before entering the sensitivity band of the advanced GW detectors, and any residual eccentricity is expected to have a negligible effect on their detectability [151]. Estimates of the IMRAC detection rate in the advanced-detector era range up to

[1]The inspiral of an IMBH into a supermassive BH is also referred to as an IMRI. GWs from such IMRIs are potential sources for a space-borne detector [33], as are the most massive (redshifted total masses of $\gtrsim 10^3$ $M_\odot$) IMBHBs [90, 164].

tens of events per year, though rates of zero are possible given the absence of confirmed IMBHs in the few-hundred-solar mass range where advanced detectors would be sensitive to emitted GWs [59, 151, 17].[1] The IMBH spin distribution is not strongly constrained from the assumed possible formation channels. If IMRACs are common, and the IMBHs increase their mass by a significant fraction by capturing compact objects from an isotropic distribution of orbital inclinations, IMBHs will on average spin down to dimensionless spin magnitudes $a \lesssim 0.2$ [149]. If IMBHs however increase their mass through runaway collisions of stars, instead of their compact object remnants, in dense stellar environments significantly wider distribution of spins can be assumed [188, 91].

The dividing line between IMBHBs and IMRACs, just like the division between IMBHs and stellar-mass BHs, is arbitrary; however, the evolution of the binary and the emitted GWs vary significantly with the mass ratio $q = m_2/m_1$, where $m_1 > m_2$ are the masses of the binary companions. Systems with more equal masses (IMBHBs with $q \sim 1$) inspiral more quickly than those with unequal masses (IMRACs with $q \ll 1$), and because of the difference in the scales associated with unequal masses, IMRACs are more challenging for numerical relativity to simulate [142, 120].

We perform a systematic parameter-estimation (PE) study for IMRAC signals using full inspiral–merger–ringdown waveforms. Details of our set up, which mirrors the analysis of Veitch et al. [246] for IMBHBs, are described in section 3.2. Results are given in section 3.3 and discussed in section 3.4, where we also examine the sensitivity of our analysis to systematics. Our main conclusions are summarized in section 3.5; in particular, we find that the advanced GW detectors could unambiguously confirm the existence of IMBHs should a suitable IMRAC ($m_1 \gtrsim 130\ \mathrm{M}_\odot$) be detected.

3.2 Study design

To determine how accurately properties of IMRACs could be measured in the advanced-detector era, we analysed a mock set of GW signals observed with

[1] For comparison, $\sim$ 30 coalescences of stellar-mass BH binaries originating in globular clusters could be detected per year [202, and erratum].

aLIGO and AdV. The simulated GW signals (injections) and the detector properties are described in subsection 3.2.1, and the data analysis is detailed in subsection 3.2.2.

3.2.1 Sources and sensitivity

Following Veitch et al. [246], we simulated a set of IMRAC signals which systematically cover the mass range of interest. We explore a range of binaries with total mass $M_{\rm total} = m_1 + m_2$ between 50 $\mathrm{M}_\odot$ and 350 $\mathrm{M}_\odot$, sampled in 25 $\mathrm{M}_\odot$ steps. For each total mass, three mass ratios q of 1/15, 1/30 and 1/50 were used.

Each injection was assigned a sky position isotropically drawn from the celestial sphere, as well as an inclination ι drawn from a distribution uniform in $\cos\iota$. The distance to each source was then selected to yield a signal-to-noise ratio (SNR) of $\rho = 15$, distributed across the detector network, in order to give an indication of typical PE accuracy; the dependence of PE on ρ is investigated in subsection 3.4.2.[1]

The injected signals were generated using a spin-aligned effective-one-body–numerical relativity (SEOBNR) waveform approximant, specifically SEOBNRv2 [226, 225]. These waveforms are constructed via the effective-one-body formalism [61, 62] for the inspiral dynamics, with the merger and ringdown portions calibrated to a suite of numerical relativity simulations [e.g., 172]. The companion spins are assumed to be aligned; including effects of generic spin alignments (such that there is precession) is an area of active development [180]. We only inject signals from non-spinning systems for this first study; we hope to include full spin effects in the future. Additionally, we assume the binaries to be fully circularized before they enter the detectors' sensitive frequency band; as waveform approximants allowing for eccentricity effects become available for PE studies, we hope to include them as well.

The output of GW detectors is the sum of the GW strain and random detector noise. The particular noise realisation present determines which GW template best matches the data. The best matching template may have parameters offset

[1] The median SNR of detected signals, assuming that sources are uniformly distributed in (Euclidean) volume is $\rho_{\rm med} = 2^{1/3}\rho_{\rm det}$, where $\rho_{\rm det}$ is the detection threshold [211]. Taking a detection threshold of $\rho_{\rm det} = 12$ [26], $\rho_{\rm med} \simeq 15$.

from the true value; over many different realisations of the noise, this shift in the parameter estimates should average to zero.[1] However, at a given ρ, the measurement uncertainty should not be significantly influenced by the details of noise realisation. Since we are primarily concerned with PE accuracy, and not the specific effects of different noise realisations, we use zero-noise injections; this simplifies comparison between different simulations as we only need to consider differences in the input parameters and not the noise.

We assume that aLIGO and AdV are operating at their respective design sensitivities [214, 27], which are expected to be realised at the end of the decade [26]. To fully utilise the detectors' sensitivity to IMRAC sources, a lower frequency cut-off of $f_{\text{low}} = 10$ Hz was chosen for all three detectors; the importance of this low-frequency sensitivity is examined in subsection 3.4.1.

3.2.2 Parameter estimation

The data, with injected signals, were analysed using the Bayesian PE pipeline `LALInference` [247].[2] For each event, `LALInference` computes a set of samples drawn from the joint posterior probability distribution spanning the signal parameters. To calculate the posterior, we need a model for the likelihood and prior probability distributions for the parameters.

The likelihood is calculated by matching a template signal to the data [70], as also described in section 1.3. The analysis was performed using the SEOBNRv2_ROM_DoubleSpin waveform approximant [193, 194], a reduced-order model (ROM) surrogate of SEOBNRv2 implemented in the frequency domain and therefore provides a speedup of a factor $\sim$ few hundred compared to the general time-domain waveform. This approximant follows the effective one-body formalism for the inspiral-merger phases, with unknown higher-order terms calibrated to numerical relativity, and a ringdown modelled as a superposition of quasi-normal modes (c.f. subsection 1.2.2). The development of this ROM

[1] The presence of non-stationary noise features (glitches) could impact PE leading to systematic errors. Realistic non-stationary, non-Gaussian noise has been shown not to affect PE performance for binary neutron stars [51]; however, these noise features could be more significant in analysing short-duration, low-frequency IMRAC signals.

[2] A component of the LIGO Scientific Collaboration Algorithm Library (LAL) suite http://www.lsc-group.phys.uwm.edu/lal.

has enabled PE studies previously deemed computationally infeasible, expanding the accessible parameter space for studies of CBC sources [cf. 246]. By using the same approximant for injection and recovery, we remove any systematic error caused by waveform uncertainty (cf. subsection 3.4.3). SEOBNRv2 and its ROM surrogate only include the leading order quadrupolar mode of the GW radiation, but as it has been shown that higher-order modes can significantly improve the PE for IMBHB systems [98], we hope to be able to include them in future IMRAC studies.

For this analysis, we adopted a flat prior distribution on the companion masses m_1, $m_2 \in [0.6, 500]$ $\mathrm{M}_\odot$ with the constraints $M_{\mathrm{total}} > 12$ $\mathrm{M}_\odot$ and $q > 0.01$. While all injections were non-spinning, we do allow for the exploration of dimensionless spin magnitudes $a_1, a_2 \in [-1, 0.99]$, aligned with the orbital angular momentum, with uniform priors. We also assume an isotropic prior on the source position and orientation in the sky as well as a uniform-in-volume prior on the luminosity distance out to 4 Gpc.

GWs are redshifted in an expanding Universe. This corresponds to redshifting all masses from a source at redshift z by a factor of $(1 + z)$, and scaling the GW amplitude with the inverse of the luminosity distance. In this study, we report the injected and recovered masses as redshifted to the detector rest frame, rather than the physical source frame masses, except where otherwise noted. The implications of cosmological effects are discussed in further detail in subsection 3.3.1.

3.3 Key results

We characterize the posterior probability distributions produced by `LALInference` in terms of the innermost 90% credible intervals $\mathrm{CI}_{0.9}$, spanning the 5th to the 95th percentiles, for one-dimensional marginalized parameter distributions [11].

For low-mass systems, where the recovered SNR is dominated by the inspiral part of the coalescence [11], the best constrained parameter is the chirp mass $\mathcal{M} = m_1^{3/5} m_2^{3/5} M_{\mathrm{total}}^{-1/5}$. The uncertainty on the chirp-mass measurement is shown in Figure 3.1. For greater M_{total} the SNR becomes increasingly dominated by the merger and ringdown; the properties of the ringdown depend only on M_{total} and a_{f}, the spin of the final BH [cf. 98, 246]. High-mass systems, $M_{\mathrm{total}} \gtrsim 200$ $\mathrm{M}_\odot$, are

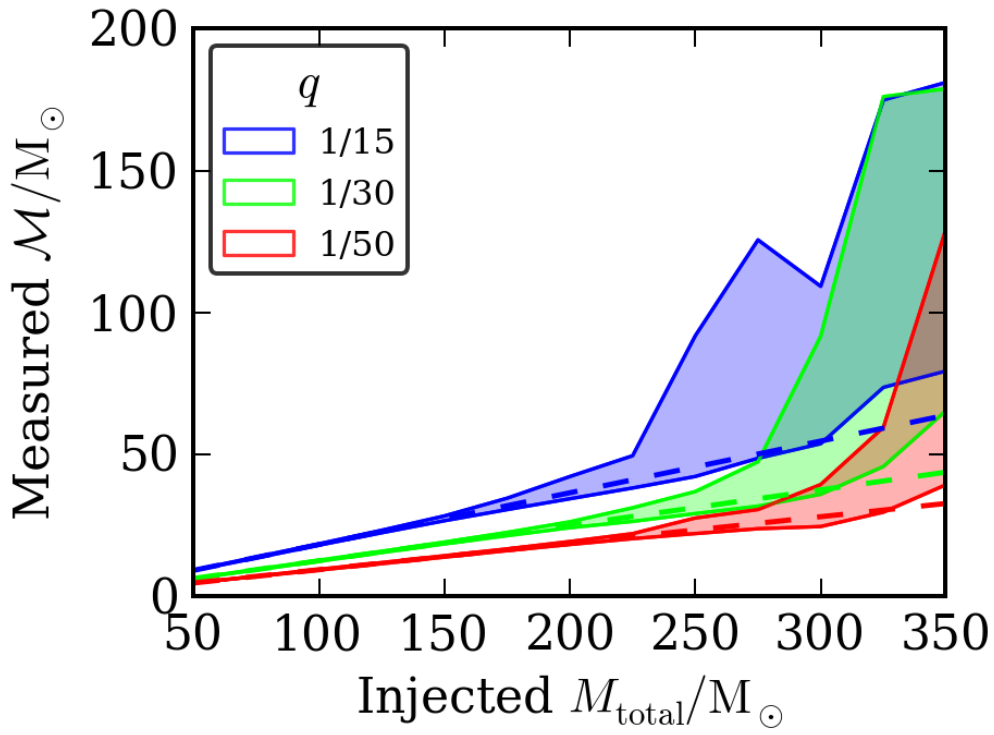

Figure 3.1 The 90% credible interval for the chirp mass $\mathcal{M}$ as a function of M_{total} and q. The true $\mathcal{M}$ values are shown as dashed lines for each q. The $\mathcal{M}$ measurement accuracy gradually worsens as M_{total} increases up to $M_{\mathrm{total}} \sim 200\ \mathrm{M}_\odot$ and then deteriorates markedly in the region where little of inspiral phase falls into the sensitive frequency band of the detectors (cf. Figure 3.3).

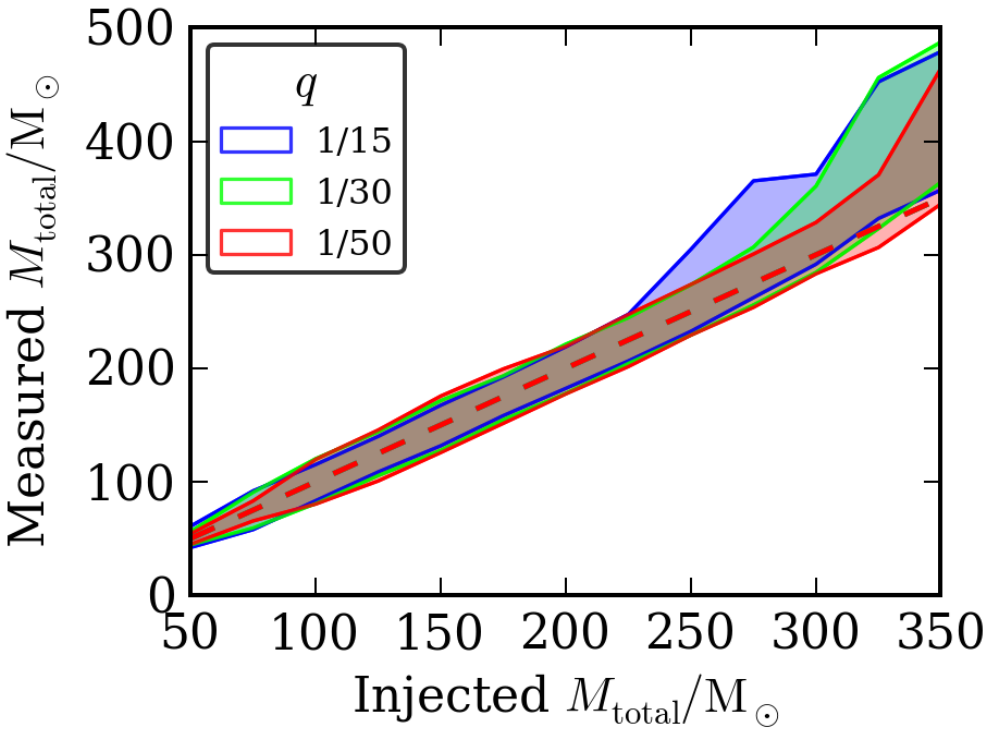

Figure 3.2 The 90% credible interval for $M_{\rm total}$. The true $M_{\rm total}$ values are shown as a dashed line. For higher $M_{\rm total}$ the $\mathrm{CI}_{0.9}$ widens, and is biased above the true value of $M_{\rm total}$ as a result of the strong prior support for systems at higher luminosity distances (cf. Figure 3.4).

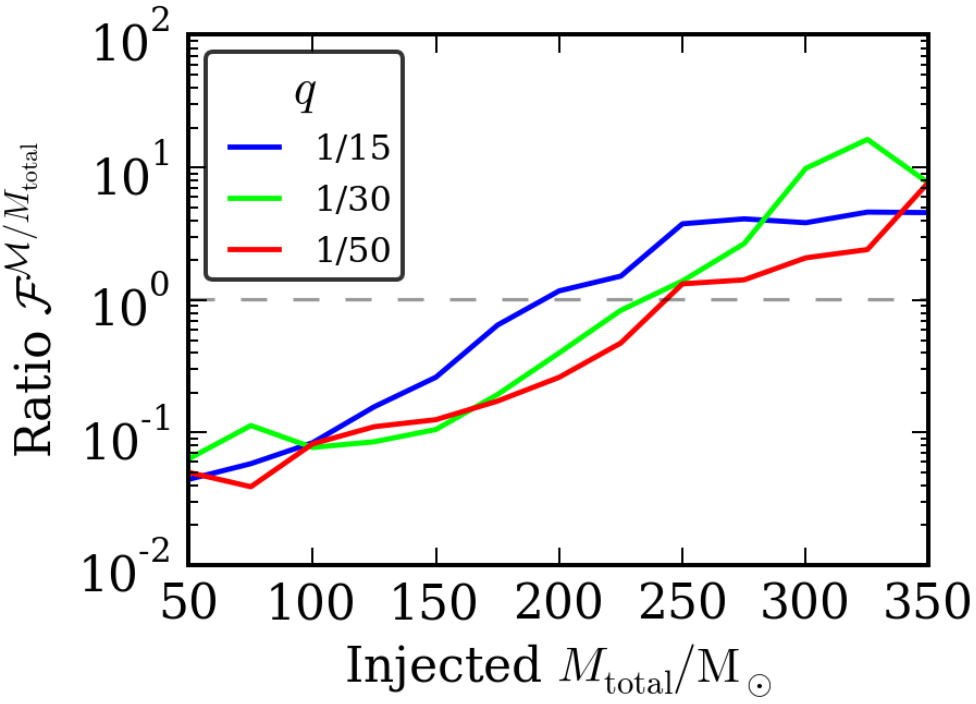

Figure 3.3 The ratio of the widths of the 90% credible intervals (rescaled by injected values) for $\mathcal{M}$ and $M_{\rm total}$, $\mathcal{F}^{\mathcal{M}/M_{\rm total}} = ({\rm CI}^{\mathcal{M}}_{0.9}/\mathcal{M})/({\rm CI}^{M_{\rm total}}_{0.9}/M_{\rm total})$. The chirp mass is the better measured mass parameter for $\mathcal{F}^{\mathcal{M}/M_{\rm total}} < 1$ and the total mass is better measured for $\mathcal{F}^{\mathcal{M}/M_{\rm total}} > 1$; for $M_{\rm total} \gtrsim 200$ M$_\odot$, $M_{\rm total}$ is the better measured mass parameter.

therefore better constrained in terms of their $M_{\rm total}$ (Figure 3.2) than their $\mathcal{M}$, as shown in Figure 3.3. As discussed in subsection 3.4.1, since the measurement accuracy of $\mathcal{M}$ scales inversely with the number of in-band cycles of the inspiral, the specific mass of the $\mathcal{M}$–$M_{\rm total}$ transition depends on the lower limit of the detector's sensitive frequency band $f_{\rm low}$, either set explicitly as part of the analysis or implicitly by either a high noise floor or uncertain low-frequency calibration.

The mass measurements can alternatively be represented by the 90% credible intervals for the companion masses. Figure 3.4 shows that the larger mass m_1 is well constrained due to its near equivalence to $M_{\rm total}$ for these systems. At low $M_{\rm total}$, the mass ratio also provides tight constraints on m_2 compared to more equal mass systems [246]. The strong dependence of the number of waveform cycles (in the detector band) upon the mass ratio means that even a small shift away from the true q value causes a large dephasing between the signal and template waveforms (assuming that $M_{\rm total}$ or $\mathcal{M}$ is well constrained), and therefore a rapid decrease in the measured likelihood. At high $M_{\rm total}$ the detectors are only sensitive to the ringdown of the coalescence, where the mass-ratio dependence is only measured weakly through the final BH spin $a_{\rm f}$.

The remnant spin together with the final mass $M_{\rm f}$ determines the frequency of the quasi-normal modes (QNMs) of the ringdown of the merged BH. Following an approximate model for estimating $M_{\rm f}$ and $a_{\rm f}$ [112, Equations 14 and 16] it is then possible to convert the posterior samples in the space of companion masses and spins into the frequency $f_{\rm RD}$ of the 0th overtone of the dominant $(l, m) = (2, 2)$ QNM as [52, Table VIII],

$$f_{\rm RD} = \frac{c^3}{2\pi G M_{\rm f}} \left[1.5251 - 1.1568(1 - a_{\rm f})^{0.1292}\right]. \tag{3.1}$$

Figure 3.5 compares the inferred $f_{\rm RD}$ to the value of the ringdown frequency of the injected waveform. It is the most accurately measured parameter for high $M_{\rm total}$ systems (cf. Aasi et al. 12 for IMBHB systems), while $M_{\rm total}$ (cf. Figure 3.2) suffers from a partial degeneracy with spin.

For these non-spinning injections, Figure 3.6 shows the recovery of the combined effective spin $\chi \equiv (m_1 a_1 + m_2 a_2)/M_{\rm total}$ [206]; χ encompasses both the relatively well measured spin of the higher mass companion and the unconstrained

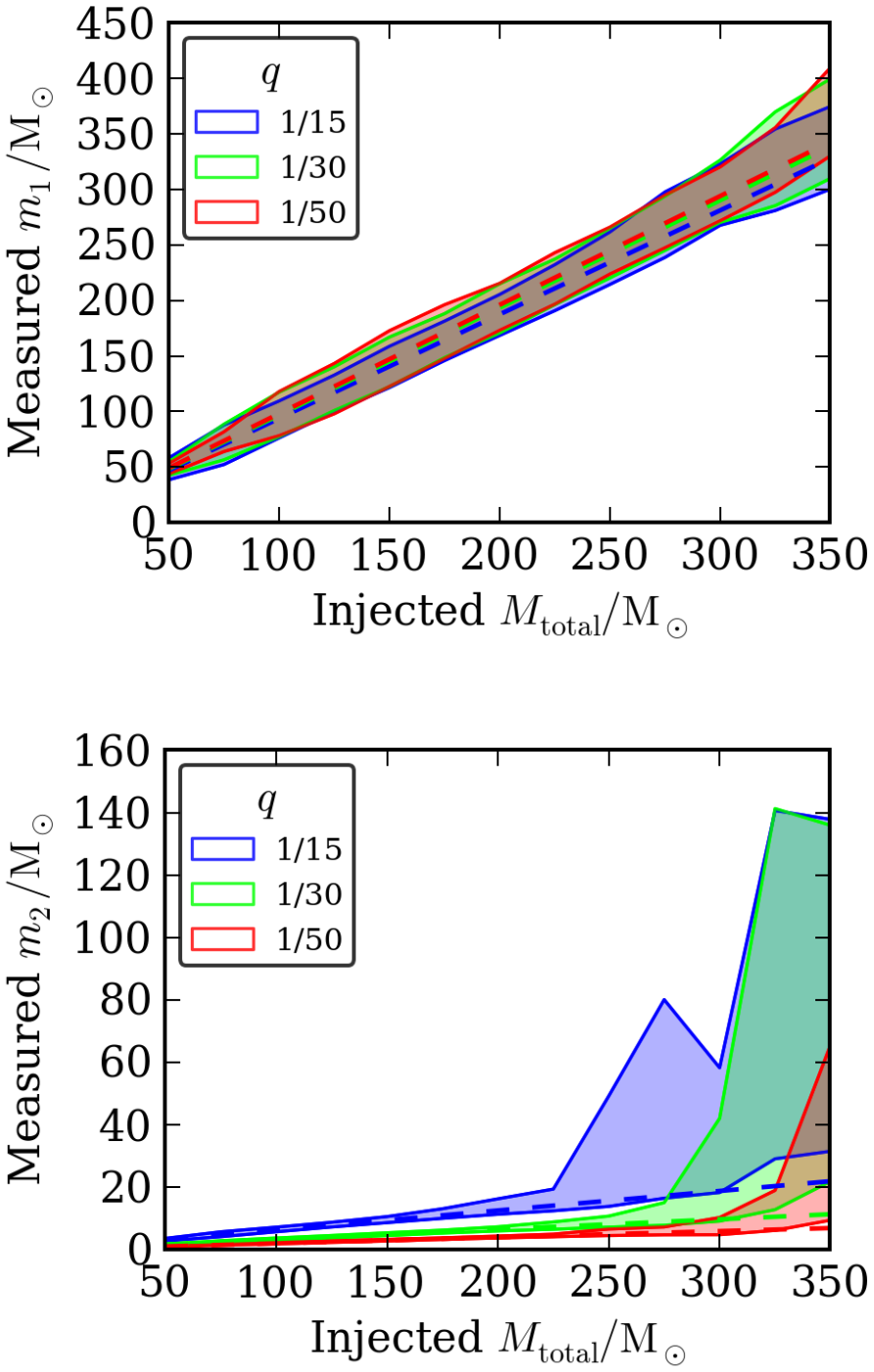

Figure 3.4 The 90% credible intervals for the larger and smaller companion masses, m_1 (top) and m_2 (bottom), respectively. The mass of the secondary m_2 is poorly measured and biased upward (toward stronger signals which can be observed at greater distances) when M_{total} is so large that little of the inspiral falls into the sensitive frequency band.

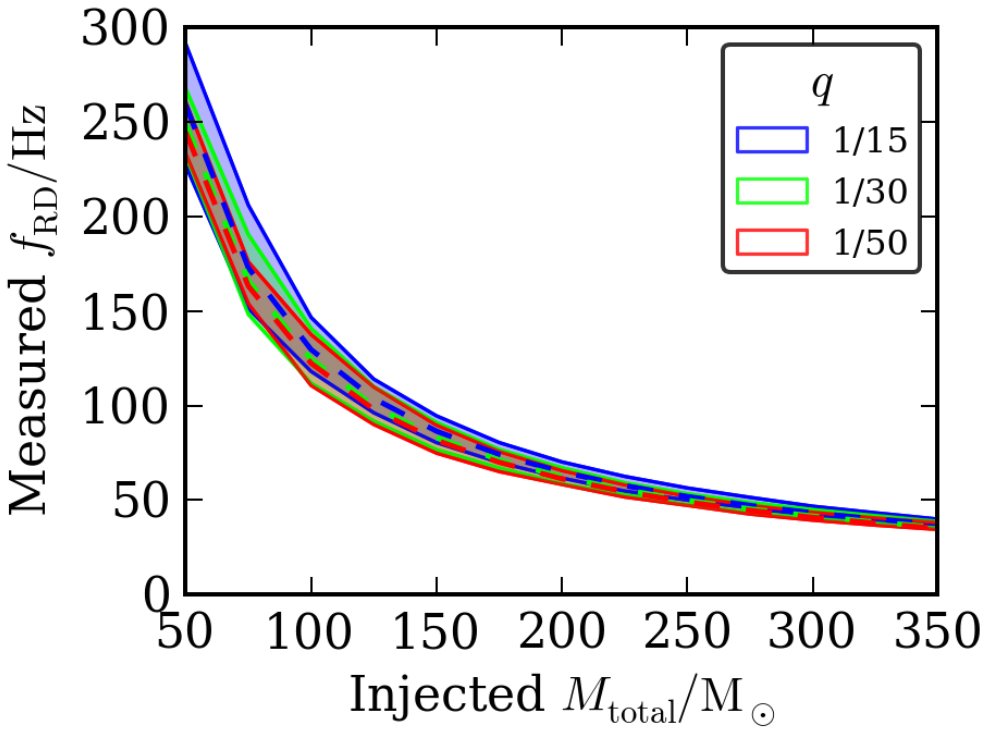

Figure 3.5 The 90% credible interval for $f_{\rm RD}$. The true values are shown as dashed lines for each q. For high $M_{\rm total}$ systems, whose in-band signal is dominated by the ringdown, $f_{\rm RD}$ is better constrained than $M_{\rm total}$.

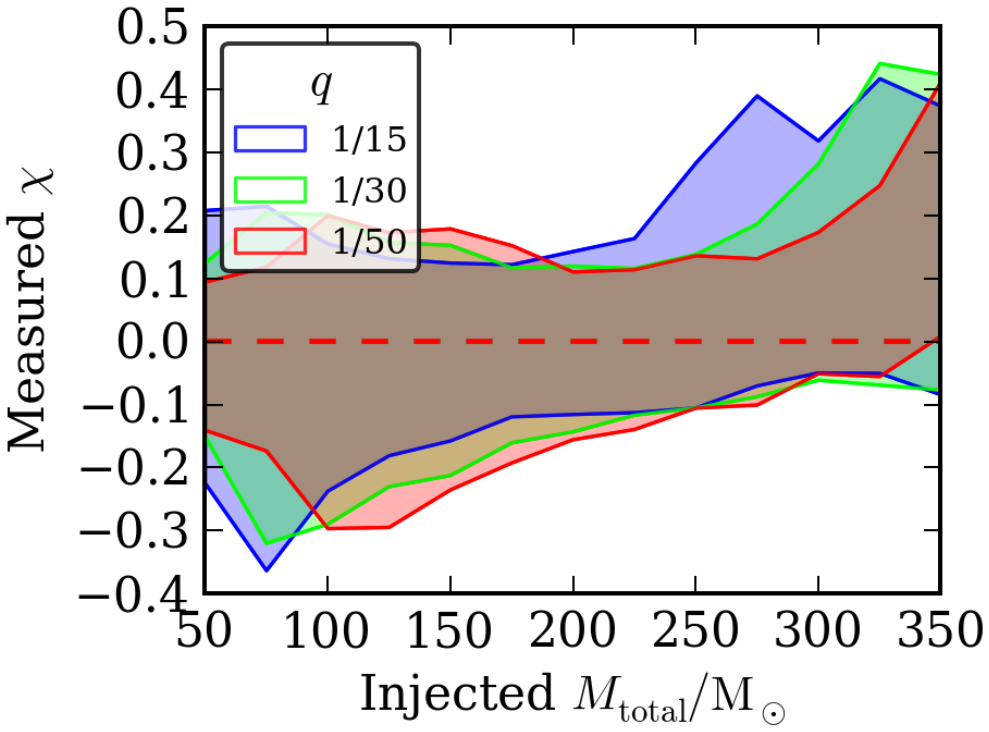

Figure 3.6 The 90% credible interval for the effective dimensionless spin χ, with all injections at $\chi = 0$. Estimates are constrained to $\sim 1/5$ of the prior range for all M_{total} and q.

spin of the lower mass companion. The effective spin can be constrained to $\sim 1/5$ of the prior range, always being consistent with $\chi = 0$. The trend towards larger positive χ for high M_{total} is a consequence of the degeneracy between χ and M_{total}. There is a preference for systems at larger luminosity distances (as a consequence of our assumption of sources being uniformly distributed in volume), which makes signals quieter, but this can be compensated by an overestimation of M_{total}. This, combined with q tending towards equal mass for those systems, forces χ to higher positive values in order to correct for the in-band length of the observed signal, the end of the inspiral, and the well measured ringdown frequency (cf. Equation 3.1).

3.3.1 Effects of cosmology on inferring the presence of an IMBH

GW observations of IMRACs or IMBHBs may provide the first conclusive evidence for the existence of IMBHs. In order to infer the presence of an IMBH in an IMRAC, we need to be able to claim that m_1 is greater than a fiducial threshold $M_{\rm IMBH}$ at a desired confidence level. Here, we follow Veitch et al. [246] and adopt a threshold mass $M_{\rm IMBH} \geq 100\ {\rm M}_\odot$.[1]

To infer the presence of an IMBH we must constrain the *physical* mass of the source. GWs are redshifted due to the expansion of the universe. This corresponds to a redshifting of the companion masses as $m_{1,2} = m_{1,2}^{\rm source}(1+z)$ for a signal at redshift z; thus far in the chapter we have considered the redshifted masses as measured in the detector rest frame. Advanced ground-based detectors can observe IMRACs at maximum redshifts of $z \sim 0.2$–1, depending on the mass ratio [e.g., 43]. A signal detected with $m_1 = 100\ {\rm M}_\odot$ and redshift $z = 0.2$ would correspond to a physical system with $m_1^{\rm source} = 100/(1+0.2) \approx 83\ {\rm M}_\odot$, which would not be an IMBH by our definition. It is thus necessary to fold in redshift information in order to produce robust IMRAC mass measurements.

For each of our systems, we obtain a posterior on the luminosity distance $D_{\rm L}$. The luminosity distance is related to the redshift by [115, section 15.8]

$$D_{\rm L}(z) = \frac{c(1+z)}{H_0} \int_0^z \frac{{\rm d}z'}{\zeta(z')}, \tag{3.2}$$

where, if we assume zero curvature and neglect radiation energy density,

$$\zeta(z) = \sqrt{(1+z)^3 \Omega_{\rm M} + \Omega_\Lambda}. \tag{3.3}$$

We invert Equation 3.2 numerically to find $z(D_{\rm L})$, adopting standard cosmological parameters: $\Omega_{\rm M} = 0.3$, $\Omega_\Lambda = 0.7$ and $H_0 = 70.0\ {\rm km\,s^{-1}\,Mpc^{-1}}$. We then calculate the primary mass in the source frame as

$$m_1^{\rm source} = \frac{m_1}{1+z}. \tag{3.4}$$

[1] Veitch et al. [246] found that $m_1 \gtrsim 130\ {\rm M}_\odot$ was required to infer the presence of an IMBH in an IMBHB at 95% confidence.

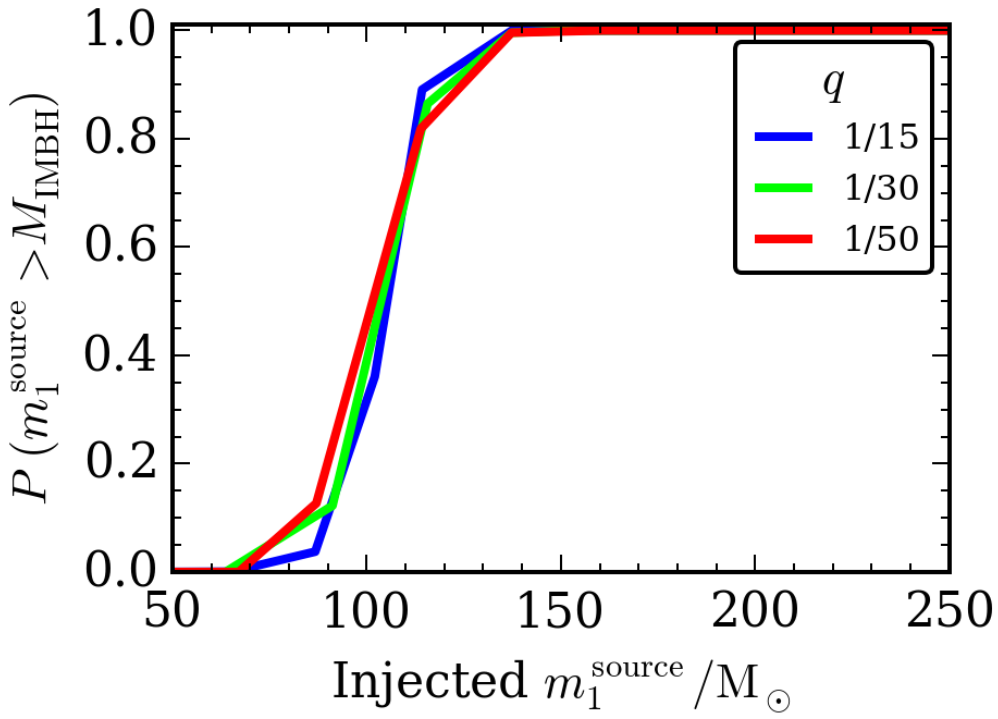

Figure 3.7 Fraction of the posterior distribution for $m_1^{\rm source} > M_{\rm IMBH} \equiv 100\ M_\odot$ as a function of the injected primary source mass. The three curves correspond to the three different mass ratios considered. We find that we can infer the presence of an IMBH at 95% confidence when the system has $m_1^{\rm source} \gtrsim 130$ M$_\odot$.

In Figure 3.7 we show the fraction of the posterior distribution for $m_1^{\rm source} > M_{\rm IMBH}$ as a function of the injected primary source mass. We find that we can infer the presence of an IMBH with mass above 100 M$_\odot$ at 95% confidence when the system has $m_1^{\rm source} \gtrsim 130$ M$_\odot$, matching Veitch et al. [246]. Additionally we can infer the presence of an IMBH at $\sim 100\%$ confidence for systems with $m_1^{\rm source} \gtrsim 150$ M$_\odot$.

3.4 Discussion

Having completed our PE study, validating our ability to measure the mass and spin parameters of IMRAC systems, we now focus on the sensitivity and ro-

bustness of our results to a selection of assumptions adopted in our analysis: the low-frequency sensitivity of the detectors (subsection 3.4.1), the SNR of the signal (subsection 3.4.2) and the accuracy of the waveform model (subsection 3.4.3).

3.4.1 Impact of low-frequency sensitivity

As a consequence of the typical high total masses of IMRACs, the low-frequency sensitivity of the detectors is expected to be crucial for PE. IMRAC parameters are most precisely measured when they are determined by an inspiral with many in-band cycles, ending at the innermost stable circular orbit at a frequency $f_{\rm ISCO}$. The transition in measurement accuracy seen in Figure 3.3 will therefore be shifted to lower masses for decreased low-frequency sensitivity, caused by either a high noise floor or uncertain low-frequency calibration.

Figure 3.8 shows a selection of frequency-domain IMRAC waveforms and the detector noise curves, represented as characteristic strains and noise amplitudes respectively [168]. The randomly chosen sky locations and orientations of our injections mean that for some mock events, the majority of the network SNR is contributed by AdV, with its relatively poorer low-frequency sensitivity, illustrated in Figure 3.9. An example of this effect is seen in the $M_{\rm total} = 275\ {\rm M}_\odot,\ q = 1/15$ event clearly visible in Figure 3.1.

Low-frequency sensitivity is particularly critical for measuring the mass ratio, as the ringdown can only provide information on the total remnant mass and spin. For example, for a $M_{\rm total} = 225\ {\rm M}_\odot,\ q = 1/15$ system which sits at the transition of inspiral detectability with the aLIGO noise spectrum with sensitivity starting at $f_{\rm low} = 10$ Hz, the 90% credible interval is ${\rm CI}^q_{0.9} \lesssim 0.05$ as shown in Figure 3.10. However, if sensitivity below 20 Hz is lost, ${\rm CI}^q_{0.9}$ spans half of the allowed range from 0 to 1, although more than 90% of the SNR is still available for detection (see Figure 3.9). If $f_{\rm low}$ increases to 30 Hz or above, q becomes essentially unconstrained with ${\rm CI}^q_{0.9}$ spanning 3/4 of its allowed range.

3.4.2 Uncertainty versus signal-to-noise ratio

To investigate the effect of the loudness of the detected signal, a series of simulations at a range of SNRs were performed. As evident from Figure 3.11, for high ρ

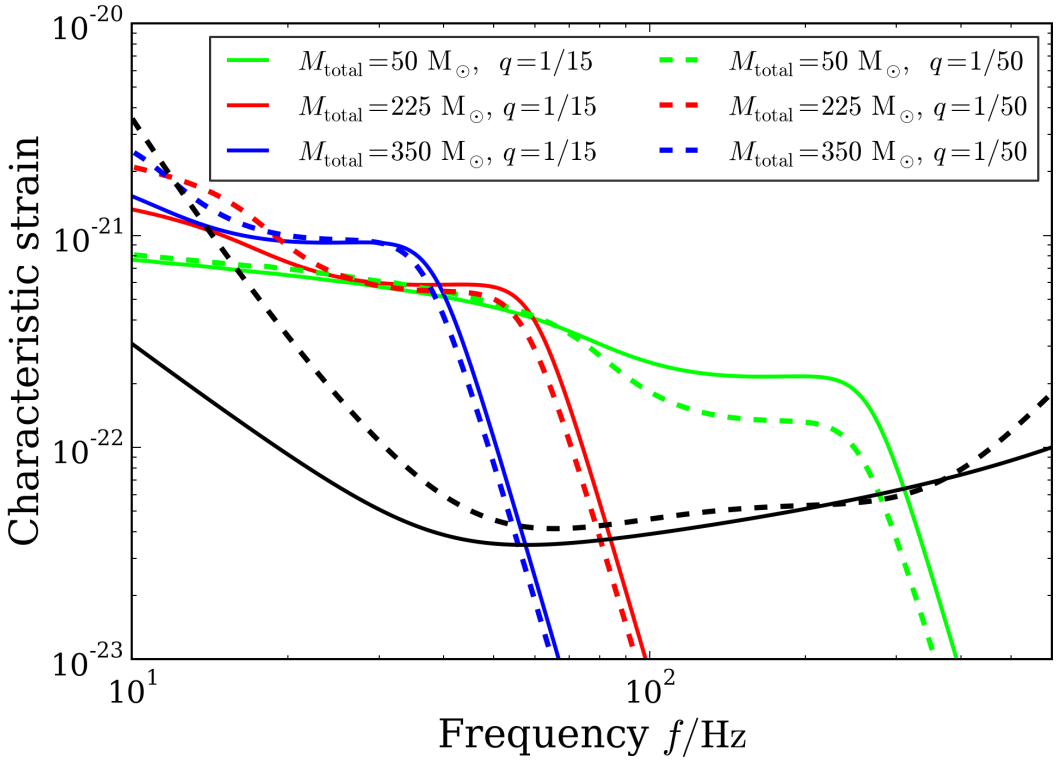

Figure 3.8 Characteristic strain $h_{\rm c} \equiv 2f|\tilde{h}(f)|$ [168] of SEOBNRv2_ROM_DoubleSpin for a range of the injected waveforms used in section 3.3, all at $\rho = 15$. In black, the dimensionless detector noise amplitude h_n [168] of the aLIGO (solid) and AdV (dashed) design noise spectra.

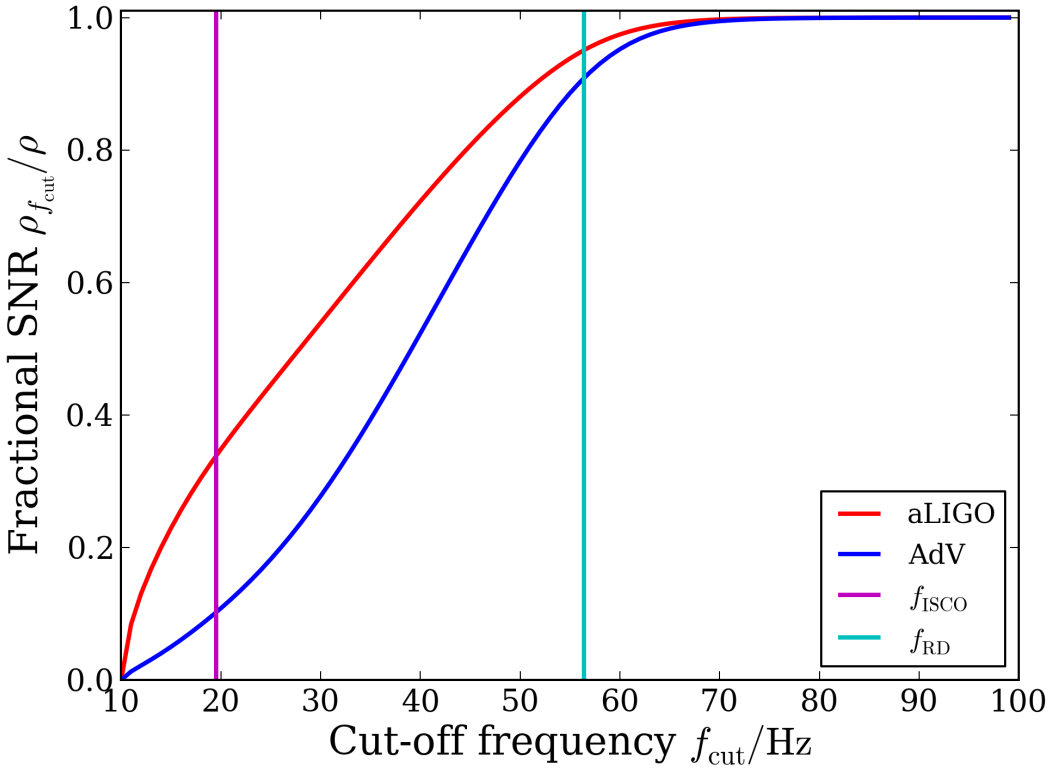

Figure 3.9 The SNR accumulated between 10Hz and $f_{\rm cut}$, $\rho_{f_{\rm cut}}$, as a fraction of the total SNR ρ, for a system with $M_{\rm total} = 225$ $\mathrm{M}_\odot$ and $q = 1/15$ injected at $\rho = 15$. This illustrates the relative low-frequency sensitivity between aLIGO and AdV used in this analysis, cf. Figure 3.8.

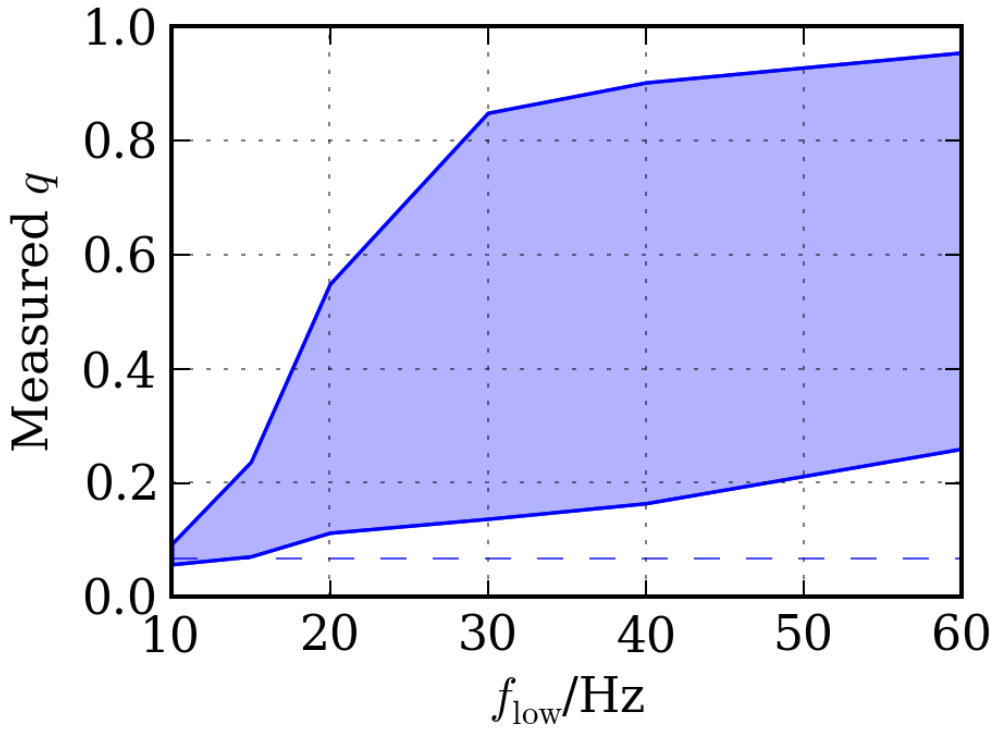

Figure 3.10 The 90% credible interval for the mass ratio q, for PE performed from a lower frequency of $f_{\rm low}$. The injected signal is a $M_{\rm total} = 225$ M$_\odot$, $q = 1/15$ system with the true value of q shown as a dashed line. As more of the low-frequency spectrum is excluded the sensitivity to the inspiral diminishes until only the ringdown remains, here no informative inference can be made as $\mathrm{CI}^{q}_{0.9}$ spans a majority of its allowed range but consistently does not include the true value of q.

the shape of the posterior distribution approaches a multivariate Gaussian, and thus the uncertainties on individual parameters scale as ρ^{-1} [cf. 241]. As shown in Figure 3.12, this behaviour can be observed starting at $\rho \sim 11$. Hence, it should be possible to scale our results to estimate PE ability for other detectable signals.

3.4.3 Systematics

At the high mass ratios of IMRACs, a post-Newtonian expansion of the inspiral alone is insufficient (due to the high masses involved) for detailed PE studies, an extreme-mass-ratio expansion in the mass ratio [the self-force problem; 187] is not yet sufficient [e.g., 153], and numerical-relativity solutions are extremely computationally expensive [e.g., 142, 120]. Therefore, possible model errors and the ensuing systematic bias in parameter recovery are a significant concern [220]. To validate our choice of SEOBNRv2 for this study, a subset of the events shown in section 3.3 were repeated as injections with a different waveform family, but still recovered with SEOBNRv2_ROM_DoubleSpin. The injections were performed with IMRPhenomD [120, 126], a phenomenological waveform model constructed in the frequency domain and calibrated against numerical relativity up to mass ratios $q \geq 1/18$.[1] This calibration limit led to the exclusion of the most extreme mass ratio binaries ($q = 1/50$) from the injection set used to study of waveform systematics. It is however important to note that, assuming each waveform model is trustworthy and self-consistent, test of systematics would be more informative for more extreme mass ratio binaries due to their increasing signal duration for a given M_{total}. There are thus a larger number of waveform cycles which have to occur without relative de-phasing, which can better highlight systematic effects.

The systematic bias in the recovered M_{total} introduced by the difference between IMRPhenomD injections and SEOBNRv2_ROM_DoubleSpin templates is small for all investigated systems, as shown in Figure 3.13, confirming the results shown in Khan et al. [126]. In particular, it is comparable to or, in the majority of cases, much smaller than the statistical uncertainty shown in Figure 3.2. Additionally, the width of the credible interval $\mathrm{CI}_{0.9}^{M_{\mathrm{total}}}$ remains largely unaffected

[1] In IMRPhenomD, IMR refers to inspiral–merger–ringdown, not intermediate mass ratio.

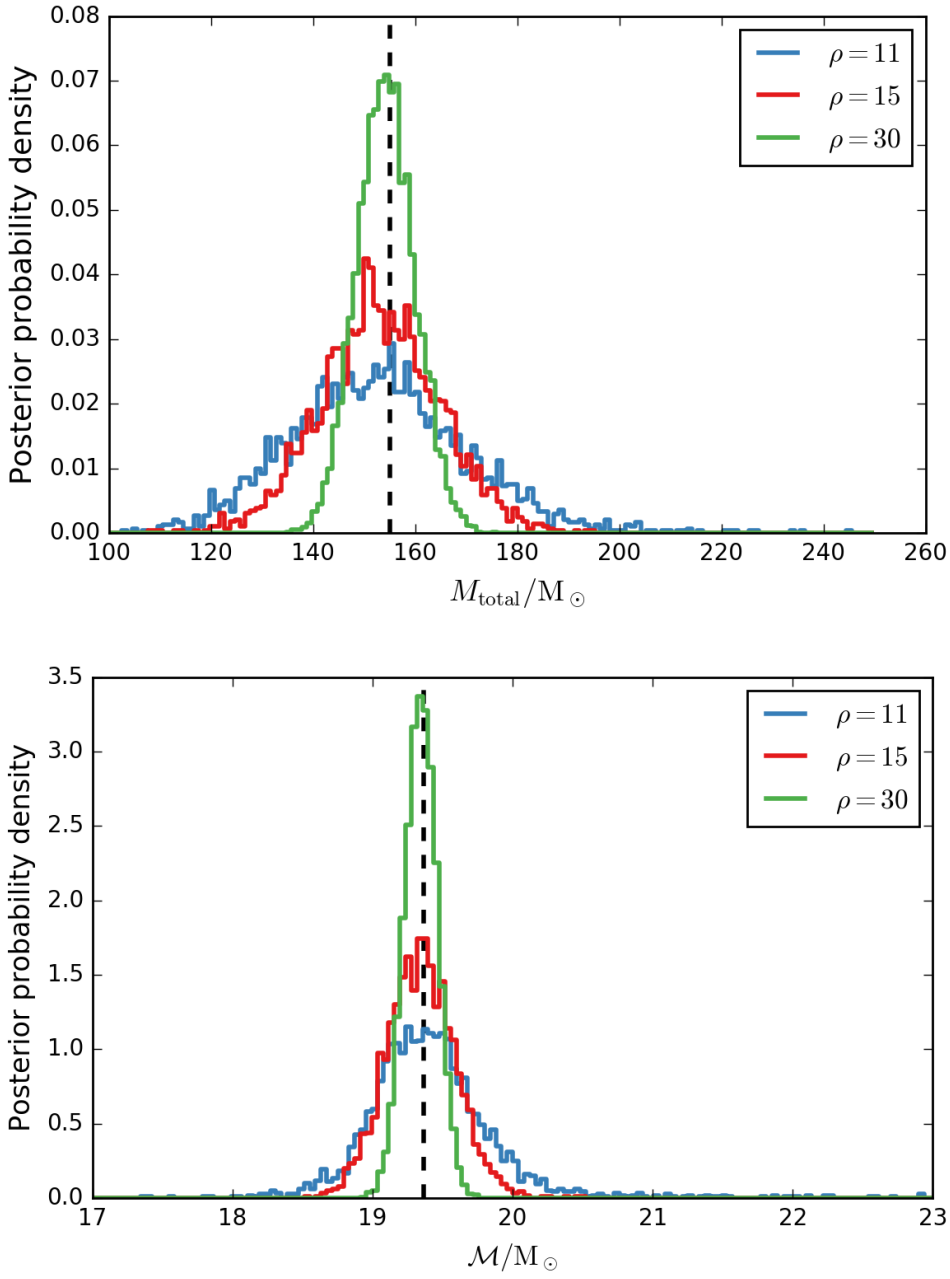

Figure 3.11 For $\rho = 11, 15, 30$ the posterior probability density functions are shown for $M_{\rm total}$ (top) and $\mathcal{M}$ (bottom) for an example system ($M_{\rm total} = 155\ {\rm M}_\odot$, $q = 1/30$). The true values are indicated by the dashed black line. Note that $\mathcal{M}$ always is better constrained than $M_{\rm total}$, as expected from this relatively low-mass system and as shown in Figure 3.3.

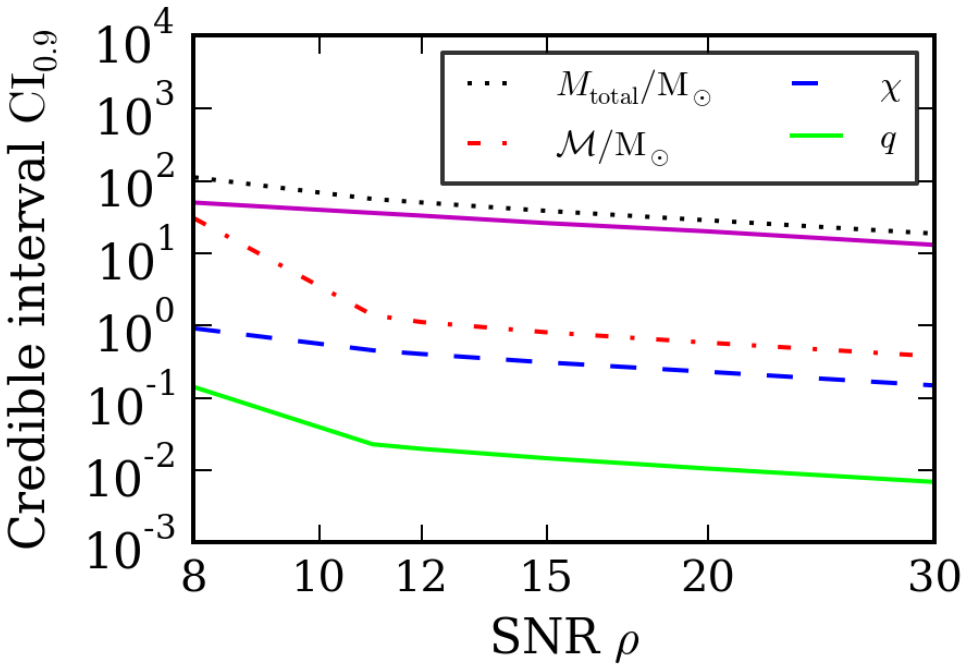

Figure 3.12 The width of the 90% credible intervals as a function of injected network SNR ρ for an example system ($M_{\rm total} = 155$ M$_\odot$, $q = 1/30$), sampled at the indicated ρ. At high ρ this follows a $1/\rho$ trend, the slope of which can be gauged by comparison with the magenta line.

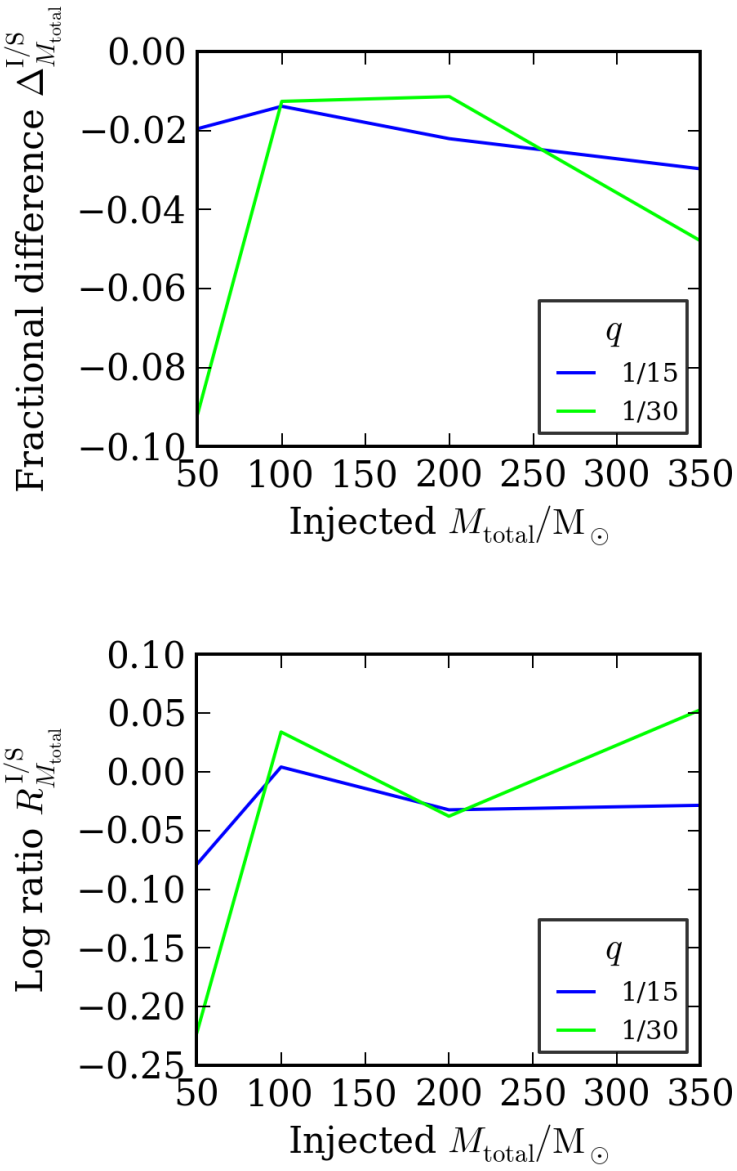

Figure 3.13 Comparison of results recovered for IMRPhenomD (I) and SEOBNRv2 (S) injections. SEOBNRv2_ROM_DoubleSpin templates are used for PE in both cases. The top panel shows the fractional difference in the recovered means of the M_{total} posterior distributions $\Delta^{\mathrm{I/S}}_{M_{\mathrm{total}}} = \left(\langle M_{\mathrm{total}}\rangle^{\mathrm{I}} - \langle M_{\mathrm{total}}\rangle^{\mathrm{S}}\right)/\langle M_{\mathrm{total}}\rangle^{\mathrm{S}}$ as a function of M_{total} and q. If the two injections were recovered with identical posteriors, then $\Delta^{\mathrm{I/S}}_{M_{\mathrm{total}}} = 0$. The bottom panel shows the natural logarithm of the ratio of M_{total} 90% credible intervals $R^{\mathrm{I/S}}_{M_{\mathrm{total}}} = \ln\left(\mathrm{CI}^{M_{\mathrm{total}}}_{0.9,\mathrm{I}}/\mathrm{CI}^{M_{\mathrm{total}}}_{0.9,\mathrm{S}}\right)$. If the posteriors have the same width, then $R^{\mathrm{I/S}}_{M_{\mathrm{total}}} = 0$; $R^{\mathrm{I/S}}_{M_{\mathrm{total}}} < 0$ indicates that the posterior distribution is narrower for the IMRPhenomD injection than for the SEOBNRv2 injection.

by systematics, even outside the region where IMRPhenomD has been calibrated to numerical-relativity waveforms.

Using the same condition as in subsection 3.3.1 for determining the presence of an IMBH, we find that the threshold of $m_1^{\rm source} \gtrsim 130$ M$_\odot$ is robust under this systematic bias. Therefore, we expect that, if the difference between IMRPhenomD and SEOBNRv2 is typical of the waveform model uncertainty in the IMRAC parameter space, then the systematic error introduced from waveform uncertainty should not hinder the identification of IMBHs from IMRAC observations. We evaluated the impact of systematics by comparing posterior probability distributions computed with different models of spin-aligned, circular templates without higher-order modes; the impact of systematics will need to be re-evaluated once waveforms incorporating all of these effects are available.

3.5 Summary

IMBHs may play an important role in the formation of supermassive BHs, and the dynamics of dense stellar environments like globular clusters [e.g., 238, 94, and as dicussed in chapter 2], yet conclusive evidence for their existence remains elusive. A network of advanced GW detectors can observe an IMBH as part of an IMRAC at cosmological distances, out to redshift $z \gtrsim 0.5$. Recent progress in the development of waveforms suitable for IMRAC systems has enabled the first systematic study of the measurement of the masses and spins of IMRACs. Despite the short in-band signal, we find that inference on the emitted GWs can provide interesting measurements of IMRAC systems.

For low mass IMRAC systems, $\mathcal{M}$ is the best constrained parameter. As total mass increases, the inspiral moves out of the sensitive frequency band of the detectors, after which most of the information comes from the ringdown of the merger remnant, so that the ringdown frequency is best constrained. For high-mass systems, $M_{\rm total}$ is measured more precisely than $\mathcal{M}$, but is still partly degenerate with the (poorly constrained) spin.

With a low and stable noise floor at low frequencies, it will be possible to infer the presence of an IMBH with mass ≥ 100 M$_\odot$ at 95% confidence for systems with $m_1^{\rm source} \gtrsim 130$ M$_\odot$. This relies on the assumption of standard cosmology to

infer the source mass from the measured redshifted mass and luminosity distance.

By using different waveform approximants for signal injection and PE, we confirm that our results, including the detectability of an IMBH, are robust against potential waveform errors so long as they fall in the range bracketed by these approximants.

Future investigations of IMRACs will benefit from ongoing waveform development to include spinning and precessing signals, possibly eccentric binaries, and higher-order modes. Building upon improved confidence in parameter estimation with IMRAC waveforms, future studies could focus on using IMRAC observations to enhance our understanding of globular-cluster dynamics, and the suitability of IMRACs for high-precision tests of general relativity in the strong-field regime [e.g., 59, 93, 201].

Chapter 4

Efficient method for measuring the parameters encoded in a gravitational-wave signal

This chapter is adapted from a paper by *Carl-Johan Haster*, Ilya Mandel and Will M. Farr. My contribution to this work was to *(i)* design and write the software used in this study, *(ii)* run simulations, *(iii)* verify the results, focusing on the accuracy of the recovered credible regions, against alternative methods, *(iv)* write the paper. This paper is published in Classical and Quantum Gravity [109] and has arXiv number 1502.05407.

4.1 Introduction

Advanced LIGO gravitational-wave (GW) detectors began their first observing run on 12 September 2015 as discussed in chapter 1, with Advanced Virgo expected to start scientific operations during 2016 [106, 227, 27, 27, 26]. A prime source predicted to be observable by these detectors are compact binary coalescences (CBCs) during which neutron star (NS) or black hole components of the binary are driven by GW emission through an inspiral into a merger (c.f. section 1.1 and subsection 1.2.2). Binary NS (BNS) have already been observed as pulsars in Galactic binary systems evolving due to emission of GWs [251, 130];

extrapolations from these observations yield estimated coalescence rates of BNS systems as detectable by the Advanced LIGO–Virgo network ([17] and references therein).

4.1.1 Binary coalescence model

The information encoded in a GW observation of a circularized CBC event is encoded through the waveform $\vec{h}$, fully described by a 15-dimensional parameter vector $\vec{\theta}$ which in turn can further be divided into two parameter sets. The amplitude and phase evolution of the waveform are governed by the intrinsic parameters which include the masses and spins of the binary components (and tidal deformability parameters where applicable). The extrinsic parameters describe the projection of the gravitational wave emitted by the binary onto the detectors and include the object's position and orientation on the sky, its luminosity distance d_L as well as the time and phase of the waveform at coalescence (t_c and ϕ_c). The level of correlation between the two parameter sets is only marginal, apart for t_c and ϕ_c which are strongly correlated with intrinsic parameters. Therefore we will simplify the analysis by fixing the remaining extrinsic parameters at their true values without significant impact on the recovery of the intrinsic parameters; we return to this point in section 4.4.

In this study we consider as an example a BNS with component masses $m_1 = 1.45M_\odot$ and $m_2 = 1.35M_\odot$. While there is a strong degeneracy between the mass and spin parameters, which affects their measurement uncertainty [60, 218, 51, 87, 103], the BNS components are in this study taken as non-spinning for demonstration purposes, as our focus here is on parameter estimation techniques rather than astrophysical predictions. Therefore, the original 15-dimensional parameter space is reduced to only four parameters, the two masses as well as t_c and ϕ_c, without loss of generality in the method applied. The waveform approximant used is TaylorF2 [63] which is described in subsubsection 1.2.2.1.

As discussed in subsection 1.3.2, the likelihood of observing data $d \equiv h_T + n$, containing the true waveform h_T and stationary, Gaussian instrumental noise n,

given a waveform model $h(\vec{\theta})$ described by parameters $\vec{\theta}$ is

$$L(\vec{\theta}) \propto \exp\left(-\frac{1}{2}\left\langle n + h_T - h(\vec{\theta}) \middle| n + h_T - h(\vec{\theta}) \right\rangle\right). \tag{4.1}$$

The term in the angle brackets is the noise-weighted power in the residuals after subtracting the assumed model from the data, defined in Equation 1.17. The likelihood (Equation 4.1), together with the specification for the waveform model and the noise power spectral density $S_n(f)$, which is chosen to match the Advanced LIGO zero-detuning high-power design sensitivity [214], constitutes the model H.

For this study we will consider a BNS observed directly overhead in one detector at a signal to noise ratio $\rho = 12$, defined as in [25, but c.f. Equation 1.16]:

$$\rho \equiv \max_{\vec{\theta}} \frac{\langle d | h(\vec{\theta}) \rangle}{\sqrt{\left\langle h\left(\vec{\theta}\,|D_{ref}\right) \middle| h\left(\vec{\theta}\,|D_{ref}\right) \right\rangle}}, \tag{4.2}$$

where the waveforms in the denominator are calculated for a reference distance D_{ref}. The injected noise realisation in our example is chosen to be $n \equiv \vec{0}$, which fixes the maximum likelihood waveform to be h_T.

4.1.2 Bayesian inference

Given the model H as described in subsection 4.1.1, Equation 4.1 can be viewed as a probability density function (PDF) $p(d|\vec{\theta}, H)$ for observing data $d \equiv h_T + n$ given parameters $\vec{\theta}$. Together with a PDF on the parameters detailing the prior knowledge and expectation about $\vec{\theta}$ under H, $p(\vec{\theta}|H)$, a posterior PDF can be obtained through Bayes' theorem as in Equation 1.21:

$$p(\vec{\theta}|d, H) = \frac{p(\vec{\theta}|H)p(d|\vec{\theta}, H)}{p(d|H)}. \tag{4.3}$$

The term in the denominator is called the evidence and can be used for comparing the effectiveness of different models' ability to describe the data; for this study, it is a normalizing constant for the posterior PDF. The task of parameter estimation

can therefore be defined as finding accurate and robust methods for evaluating the posterior probability given by Equation 4.3 in order to obtain the accuracy with which different parameters can be recovered. This accuracy is usually quantified in terms of credible regions CR_p containing a fraction p of the total posterior probability. These credible regions are defined as

$$\mathrm{CR}_p \equiv \min\ A \tag{4.4}$$

such that the parameter-space area A satisfies

$$p = \int_A p(\vec{\theta}|d, H)\mathrm{d}\vec{\theta}\,. \tag{4.5}$$

The posterior PDF will have the same dimensionality as $\vec{\theta}$ and a shape strongly dependent on the complexity of H. For the PDFs encountered in CBC data analysis, very intricate structures with high levels of multimodality and parameter degeneracies are common, and their prevalence has spurred the development and use of advanced analysis tools for sampling the posterior PDF.

4.1.3 Stochastic sampling

As part of the publicly available LSC Algorithm Library (LAL) [228], the Bayesian framework in `LALInference` implements several methods to stochastically traverse the parameter space [247, 11], creating a set of individual samples $\vec{\theta}_i$ distributed according to the posterior PDF in Equation 4.3. For this study, we used a parallel-tempered Markov chain Monte Carlo (MCMC) algorithm [160, 111], implemented in `LALInference` as `LALInferenceMCMC`. The number of MCMC samples required to fully describe the posterior PDF scales only weakly with the number of dimensions, allowing for efficient exploration of high-dimensional parameter spaces. However, only a small fraction of the collected samples will be statistically independent, due to imperfect jump proposals in the complex multimodal parameter spaces. In order to accurately represent the posterior PDF for the 4-dimensional parameter vector $\vec{\theta}$ from subsection 4.1.1, $\mathcal{O}(10^3)$ independent samples are necessary [215]. As the typical auto-correlation length between independent samples [247] is $\mathcal{O}(10^3)$, this requires a total of $\mathcal{O}(10^6)$

`LALInferenceMCMC` posterior samples, and therefore $\mathcal{O}(10^7)$ individual likelihood calculations spread across the nine differently tempered parallel chains used in this example.

4.1.4 Chapter organisation

In section 4.2 we present the "cumulative marginalized posterior" method for accurately and efficiently evaluating credible region contours on a grid. We show that credible regions can be computed with a suitable choice of a low-density grid of samples, described in subsection 4.2.2. This makes it possible to produce credible regions with the same accuracy as given by the stochastic samplers, but at a greatly reduced computational cost, as shown in subsection 4.2.3. In section 4.3 we discuss alternative grid-based methods for estimating credible regions, including the iso-match contour technique advocated by Baird *et al.* [40], and show their relative performance against the cumulative marginalized posterior method (subsection 4.3.3). We conclude in section 4.4 with a discussion of these results and a proposal for implementing the cumulative marginalized posterior method in a low-latency parameter estimation framework for GW signals from CBCs.

4.2 Discretizing the credible regions

As an alternative to the stochastic sampling methods we propose a method to evaluate the integral in Equation 4.5 using samples at pre-determined coordinates in parameter space, thus deterministically fixing the number of likelihood calculations required. The simplest implementation places samples into centres of pixels distributed in a uniform rectangular grid and approximates the posterior as constant within a pixel. The choice of the sampling grid is critical to the efficiency of this method, and will be discussed in subsection 4.2.2.

The required number of likelihood calculations, and therefore the required number of pixels, scales exponentially with the number of dimensions in the grid, so in order to minimize the computational requirements a modified version of Equation 4.1 was implemented. We use a likelihood function marginalized over t_c and ϕ_c, thus removing the need for sampling those dimensions without affecting

the PDF in the mass parameters of interest.

The analytical marginalisation over ϕ_c alone is described in [245] and [247] as being performed through a modified Bessel function of the first kind, and from symmetry arguments only the $\langle h_T|h(\vec{\theta})\rangle$ inner product, or equivalently $\langle d|h\rangle$ from Equation 1.23, needs to be taken into consideration as phase and time shifts will be absent elsewhere. Marginalising over time is performed semi-analytically using an inverse Fourier transform giving the final expression as

$$\langle h_T|h(\vec{\theta})\rangle_{marg} = \log\left(\sum_{k=0}^{N_T} I_0\left[N_T\left(\mathcal{F}^{-1}\left[\frac{\tilde{h}_T\tilde{h}(\vec{\theta})^*}{S_n(f)}2\delta_F\right]_k\right)\right]\delta_T\right) - \log(N_T\delta_T) \quad (4.6)$$

where I_0 is the modified Bessel function of the first kind, N_T is the number of samples, each of length δ_T, in the timeseries T obtained through the complex-to-complex inverse Fourier transform $\mathcal{F}^{-1}$. It is also possible to change the length of the prior in t_c by varying the number of samples N_T included in the sum.

4.2.1 Cumulative posterior on a grid

Taking advantage of the natural $[\mathcal{M}_c, \eta]$ parameterization of the waveforms, we constructed a uniformly spaced rectangular grid across these parameters. For each pixel in the grid, the likelihood corresponding to the value of $\vec{\theta}$ at its mid-point was calculated. We assumed a prior PDF on the mass distribution of BNS systems to be uniform in $[m_1, m_2]$ rather than $[\mathcal{M}_c, \eta]$ (transformed appropriately when working in the $[\mathcal{M}_c, \eta]$ space). The product of the likelihood and prior yield the numerator of Equation 4.3. The posterior PDF is obtained by normalizing this quantity by the evidence, the denominator in Equation 4.3, which is approximated as the sum of the likelihood-prior products over all pixels in the grid. The posterior PDF is assumed to be valid not just locally at $\vec{\theta}$ but instead across a whole pixel. Credible regions can then be defined by the set of pixels containing a fraction p of the posterior PDF, accumulated when traversing the pixels in order of decreasing posterior values.

4.2.2 Grid placement

To minimize computational cost and to ensure an accurate representation of the credible regions defined by the integral in Equation 4.5, the grid samples must be placed as sparsely as possible, subject to two constraints: (i) a sufficient fraction of the parameter space with significant posterior support is covered to enable accurate normalization of the posterior; and (ii) the error introduced by approximating the prior-likelihood integral over any pixel as the product of the prior and likelihood at the centre and the pixel area is within desired bounds.

The required extent of the grid can be quantified in terms of the Mahalanobis distance $r(\vec{\theta})$ defined as

$$r = \sqrt{(\vec{\theta} - \vec{\mu})\Sigma^{-1}(\vec{\theta} - \vec{\mu})^T} \tag{4.7}$$

for a set of pixel coordinates $\vec{\theta}$ spanning a multivariate N-dimensional PDF $f(\vec{\theta}) \equiv p(\vec{\theta}|d, H)$ with mean $\vec{\mu}$ and covariance Σ [148]. When $f(\vec{\theta})$ is a bivariate Gaussian, the associated cumulative density function is given by $\Phi(r) = 1 - e^{-r^2/2}$. Hence, for a maximum error $\epsilon = 1 - \Phi(r)$ in the evidence contained within the grid, the grid must minimally contain the pixels bounded by a distance

$$r_b = \sqrt{-2 \ln \epsilon} \tag{4.8}$$

away from the maximum (mean) of the PDF. The main purpose of this analysis is to construct credible regions whose p-value is known to an accuracy no worse than that of a stochastic sampler, which is of order 1% for the $\mathcal{O}(10^3)$ samples we typically have (see subsection 4.2.3). We therefore set $\epsilon = 0.005$, and will correspondingly cover the region $r_b \leq 3.25$ with a grid.

The minimum density of pixels within this bound is set by requiring that the approximate PDF, computed by discretely evaluating the posterior on a grid, is a sufficiently good approximation to the integral Equation 4.5. Here we use a very simple approximation, namely, we evaluate the integral as a Riemann sum over the equal-sized rectangular pixels, setting the contribution of each pixel to the integral equal to the product of the pixel area and the value of the PDF at the centre of the pixel. In this case, a sufficient – but not necessary – condition

for the total error on the PDF integral to be bounded by ϵ is for the fractional error in each pixel to be smaller than ϵ. For an N-dimensional PDF $f(\vec{\theta})$, this fractional difference across a pixel centred at $\vec{\theta}_0$ is

$$\left| \frac{f(\vec{\theta}_0)\Delta^N - \int_{\vec{\theta}_0 - \vec{\Delta}/2}^{\vec{\theta}_0 + \vec{\Delta}/2} f(\vec{\theta})\, \mathrm{d}\vec{\theta}}{f(\vec{\theta}_0)\Delta^N} \right| \leq \epsilon \,, \tag{4.9}$$

where Δ is the pixel width. For a one-dimensional Gaussian distribution $f(\theta) = \exp(-\frac{\theta^2}{2\sigma^2})$ with zero mean and variance σ^2, the integral in Equation 4.9 can be represented as a Taylor series:

$$\begin{aligned} &\int_{\theta_0-\Delta/2}^{\theta_0+\Delta/2} f(\theta)\, \mathrm{d}\theta \\ =& \int_{\theta_0-\Delta/2}^{\theta_0+\Delta/2} f(\theta_0) \left(1 - \frac{\theta_0}{\sigma^2}(\theta-\theta_0) - \frac{1}{2\sigma^2}(\theta-\theta_0)^2 + \frac{\theta_0^2}{2\sigma^4}(\theta-\theta_0)^2 + \mathcal{O}((\theta-\theta_0)^3)\right) \mathrm{d}\theta \\ \approx& f(\theta_0)\left(\Delta - \frac{\Delta^3}{24\sigma^2} + \frac{\theta_0^2\Delta^3}{24\sigma^4}\right) \end{aligned} \tag{4.10}$$

where the first non-zero correction term enters at the second order of the Taylor series since the approximated PDF is evaluated at the centre of the pixel. Note that this Taylor expansion will only be valid for $(\theta - \theta_0) \sim \Delta$ and $(\theta - \theta_0)/\theta_0 \ll 1$, both of which are satisfied by the condition set in Equation 4.9 for $\epsilon \ll 1$. The integral will be dominated by the last term in Equation 4.10 for increasing $|\theta_0|$; hence, the most stringent requirement on the pixel size will come from θ_0 at the bounds of the integration domain. As discussed above, our analysis is restricted to $0 \leq |\theta_0|/\sigma \leq r_b$, so Equation 4.9 becomes

$$\left| \frac{(r_b^2 - 1)}{24} \frac{\Delta^2}{\sigma^2} \right| \leq \epsilon \,, \tag{4.11}$$

Hence, for $\epsilon = 0.005$, the uniform grid size is $\Delta \approx 0.1\sigma$, i.e., a total of ~ 60 pixels are required per parameter-space dimension. Therefore, assuming no correlations between parameters, a grid of ≈ 3500 pixels is required to achieve 99.5% coverage of the posterior region and sub-percent net credible region identification.

For an implementation of this method in a production-level analysis package, the grid size can be significantly reduced in a number of ways. The grid size need not be regular; rather than requiring a fixed fractional error per pixel, we could require a fixed contribution to the absolute error, which would allow us to increase the size of pixels near the bounds of the integration volume that contain a very small fraction of the PDF but set the most stringent requirements if the fractional error criterion is used. More accurate integration can be obtained by higher-order schemes, such as Simpson's rule, lowering the minimum number of grid points necessary to achieve a given accuracy. The grid need not be rectangular, but could be an N-dimensional sphere of dimensionless radius r_b, achieving a significant volume reduction in a high-dimensional space over a cube enclosing such a sphere, as assumed above.

If the assumption of uncorrelated parameters is relaxed, Equation 4.8 and Equation 4.11 will still give the number of pixels required, but their relative placement needs to be altered. A misalignment between the grid and the PDF caused by correlated parameters or a non-ellipsoidal posterior PDF will reduce the validity of the previously given scaling relations. This can be overcome by either *(i)* oversampling the grid; *(ii)* a coordinate rotation to align the grid and the PDF; or *(iii)* a dynamical placement of the pixels, adapting the local pixel density to a preliminary PDF estimated from a coarse grid across the parameter space. A dynamical placement of the grid points would also remove the need for any assumptions on the near-Gaussianity and unimodality of the posterior PDF. These extensions to the analysis will be investigated further in future work.

4.2.3 Key results

For the example BNS system described in subsection 4.1.1, the grid-based cumulative marginalized posterior calculation can determine the credible regions of the posterior PDF to the same accuracy as `LALInferenceMCMC` using only a small fraction ($\sim 0.1\%$) of the computational cost of the stochastic sampler. This is illustrated in Figure 4.1, which shows 2945 independent samples of the posterior PDF produced by `LALInferenceMCMC`, colour coded by the credible region they fall into as given by the grid-based cumulative marginalized posterior. The credi-

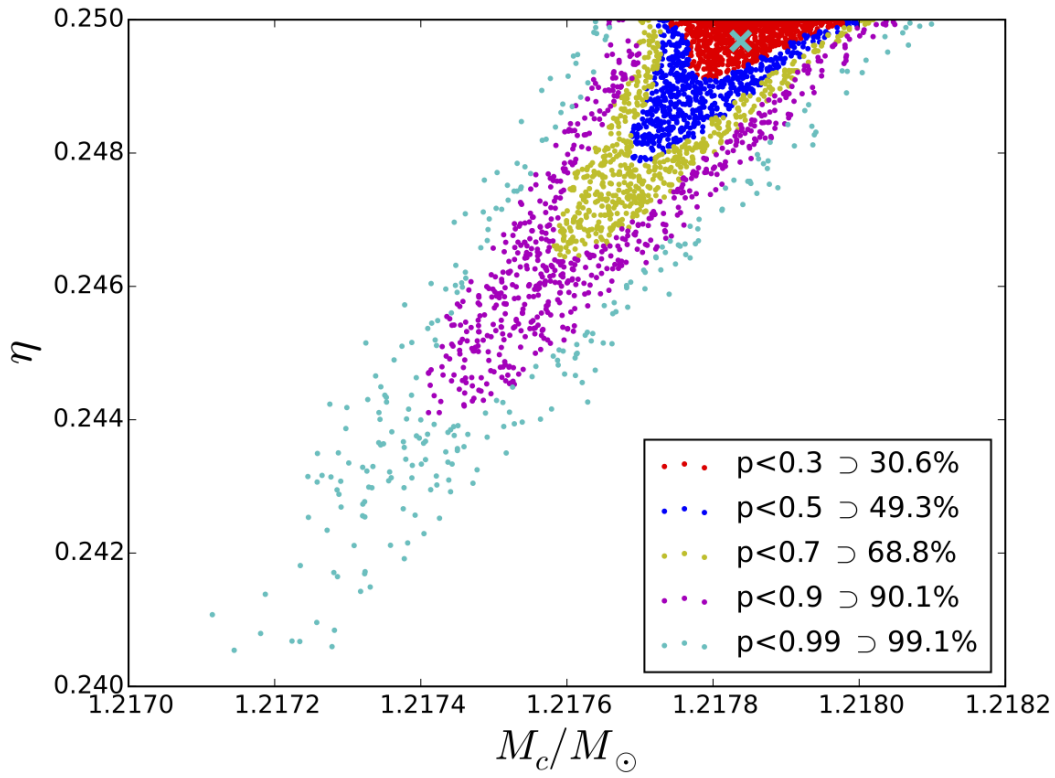

Figure 4.1 MCMC samples (dots) in $[\mathcal{M}_c, \eta]$ space are colour-coded by the *cumulative marginalized posterior* credible region they fall into. The legend compares these credible regions against the fraction of MCMC samples falling into them, which corresponds to the stochastic estimate of the fraction of posterior contained within. The true parameters of the evaluated BNS system are shown at the turquoise cross (corresponding to $m_1 = 1.45M_\odot$ and $m_2 = 1.35M_\odot$).

ble regions are compared to the fraction of MCMC samples falling into the pixels contained within them, i.e., to the credible regions as estimated by the stochastic method. The number of MCMC samples falling within a claimed credible region is governed by a binomial distribution such that the uncertainty in the fraction of samples in CR_p is $\sqrt{p(1-p)/N}$; e.g., for $N = 2945$ and $p = 0.3$, the uncertainty is 0.8% – consistent with the observed fluctuations in Figure 4.1. The credible regions, and associated uncertainties, estimated for all $p \in [0, 1]$ are shown in Figure 4.4 as a complement to the discrete set of credible regions displayed here.

4.3 Comparison with alternative methods: which approximations are warranted?

We have demonstrated that the cumulative marginalized posterior method is both accurate and computationally efficient with respect to stochastic samplers. We now explore which additional approximations can be made to simplify the analysis further; in the process, we investigate the validity of approximate techniques proposed by Baird *et al.* and Hannam *et al.* [40, 103].

4.3.1 Cumulative likelihood

In the Bayesian formalism used here, it is often assumed that the majority of the information about the posterior PDF originates from the likelihood function alone, with only a weak dependance on the prior PDF. To test this assumption, we repeated the analysis performed in section 4.2, but without the inclusion of the prior detailed in subsection 4.2.1. Evaluating the cumulative marginalized likelihood across the same $[\mathcal{M}_c, \eta]$ grid provided only negligible computational savings compared to the cumulative posterior as the overwhelming fraction of the computational cost is due to the likelihood calculations. The removal of the prior radically changed the shape of the credible regions from what was observed for the cumulative marginalized posterior in Figure 4.1 to the more ellipsoidal features shown in Figure 4.2; moreover, the credible regions computed via the cumulative marginalized likelihood method no longer match the posterior PDF as evaluated with the MCMC sampler.

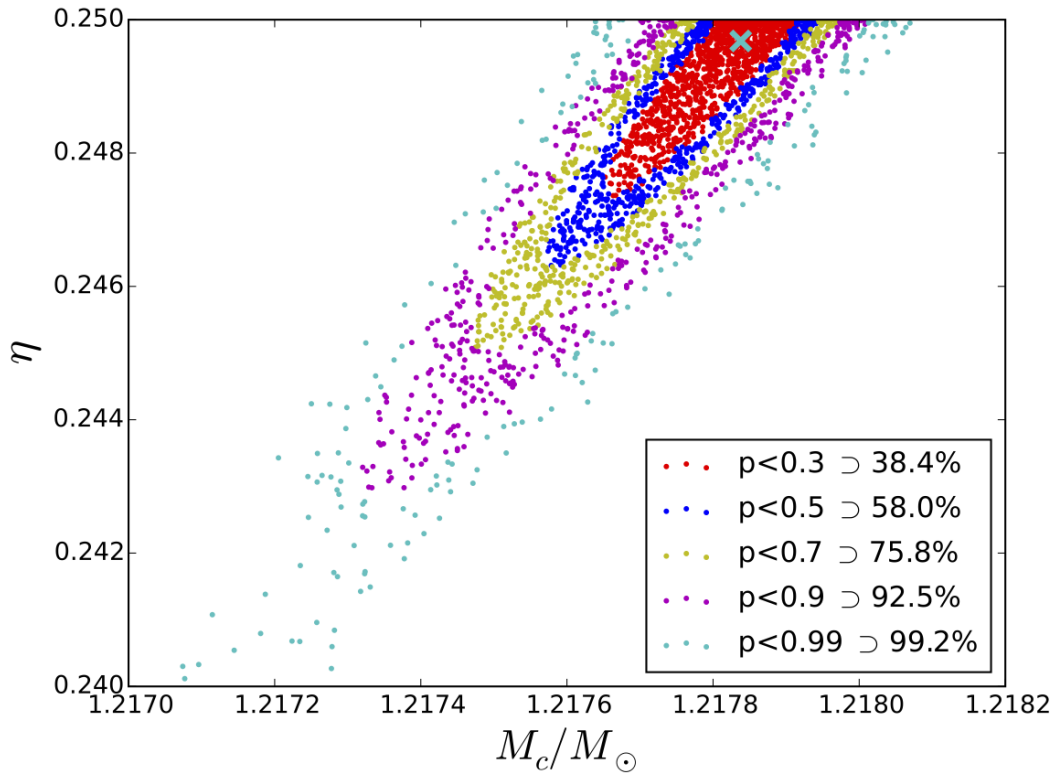

Figure 4.2 MCMC samples (dots) in $[\mathcal{M}_c, \eta]$ space are colour-coded by the *cumulative maximized likelihood* credible region they fall into. The legend compares these credible regions against the fraction of MCMC samples falling into them, which corresponds to the stochastic estimate of the fraction of posterior contained within. The true parameters of the evaluated BNS system are shown at the turquoise cross (corresponding to $m_1 = 1.45M_\odot$ and $m_2 = 1.35M_\odot$).

We next evaluated the effect of marginalization over t_c and ϕ_c by replacing the previously used likelihood function with one which instead maximizes over t_c and ϕ_c, for both the cumulative posterior and likelihood methods. This carries greater computational savings compared to ignoring the prior, as maximizing the likelihood function reduces the computational time by a factor of $\sim 1/3$ compared to marginalizing over t_c and ϕ_c. However, replacing the correct marginalization with the computationally cheaper maximization produces credible regions which are no longer consistent with the posterior PDF estimated from MCMC calculations within the uncertainty discussed in subsection 4.2.3 (cf. Figure 4.4).

While these two simplifications, particularly the use of maximization in lieu of marginalization, can yield reductions in computational complexity, the discrepancies introduced with respect to the credible regions produced by either `LALInferenceMCMC` or the cumulative marginalized posterior, are found to be outside the required tolerance level.

4.3.2 Iso-Match contours and the Linear Signal Approximation

As an alternative approach for estimating credible regions and predicting parameter accuracy, Baird *et al.* [40] introduced a method, later implemented by Hannam *et al.* [103], based on the iso-match contours. This method relies on the validity of the Linear Signal Approximation (LSA) [241, 199]. Under the LSA, waveforms are assumed to vary linearly with parameters, allowing a first-order expansion

$$h(\vec{\theta}) = h_T + h_i \Delta\theta^i \,, \tag{4.12}$$

where h_i is the partial derivative of the waveform with respect to the i^{th} parameter and $\Delta\theta^i = \theta^i - \theta^i_T$. When combined with Equation 4.1, this yields the likelihood function

$$L(\vec{\theta}) \propto \exp\left(-\frac{1}{2}\langle h_i | h_j \rangle \Delta\theta^i \Delta\theta^j\right) \,, \tag{4.13}$$

assuming $n \equiv \vec{0}$, expressed as a multivariate Gaussian centred at the true parameters $\vec{\theta_T}$ with covariance matrix $\langle h_i | h_j \rangle^{-1}$.

The method of Baird *et al.* uses the waveform match M between waveforms

h_T and $h(\vec{\theta})$ defined as

$$M = \max_{t_c,\phi_c} \frac{\langle h_T|h(\vec{\theta})\rangle}{\sqrt{\langle h_T|h_T\rangle\langle h(\vec{\theta})|h(\vec{\theta})\rangle}}\,, \tag{4.14}$$

again maximizing over t_c and ϕ_c, as a proxy for the likelihood function. By assuming that the LSA is valid, Baird *et al.* approximated credible region boundaries as contours of constant match,

$$M_p = 1 - \frac{\chi^2_N(1-p)}{2\rho^2}\,, \tag{4.15}$$

via an N-dimensional χ^2 distribution where N is again the number of dimensions of the parameter space remaining after maximization. In addition to using maximization in lieu of marginalization, the validity of this approximation relies on the Gaussianity of the posterior, and does not include a priori information.

Calculating the matches given for each pixel in the same $[\mathcal{M}_c, \eta]$ grid as used in Figure 4.1 and 4.2, we defined credible regions as the pixels bounded by the iso-match contour in Equation 4.15. Figure 4.3 compares credible regions given by iso-match contours against estimates from the fraction of MCMC samples falling within those contours; the differences between the two are statistically significant.

While the matches used by this method are calculated exactly, the restrictions implied by the LSA will lead the method to fail if the posterior PDF under investigation exhibits even a moderate level of non-Gaussianity. This can originate in the likelihood itself, or from the neglected contribution of the prior. This becomes clear for the BNS system evaluated here from the high degree of similarity between Figures 4.2 and 4.3, indicating the validity of the LSA for this system. In this particular case, the Gaussianity of the likelihood in $[\mathcal{M}_c, \eta]$ space means that the posterior would have been Gaussian if the priors were flat in $[\mathcal{M}_c, \eta]$ space, so the method could have performed relatively well; it does not perform well for flat priors in $[m_1, m_2]$ space, as indicated by Figure 4.4 (see below), because the posterior in this case is no longer Gaussian.

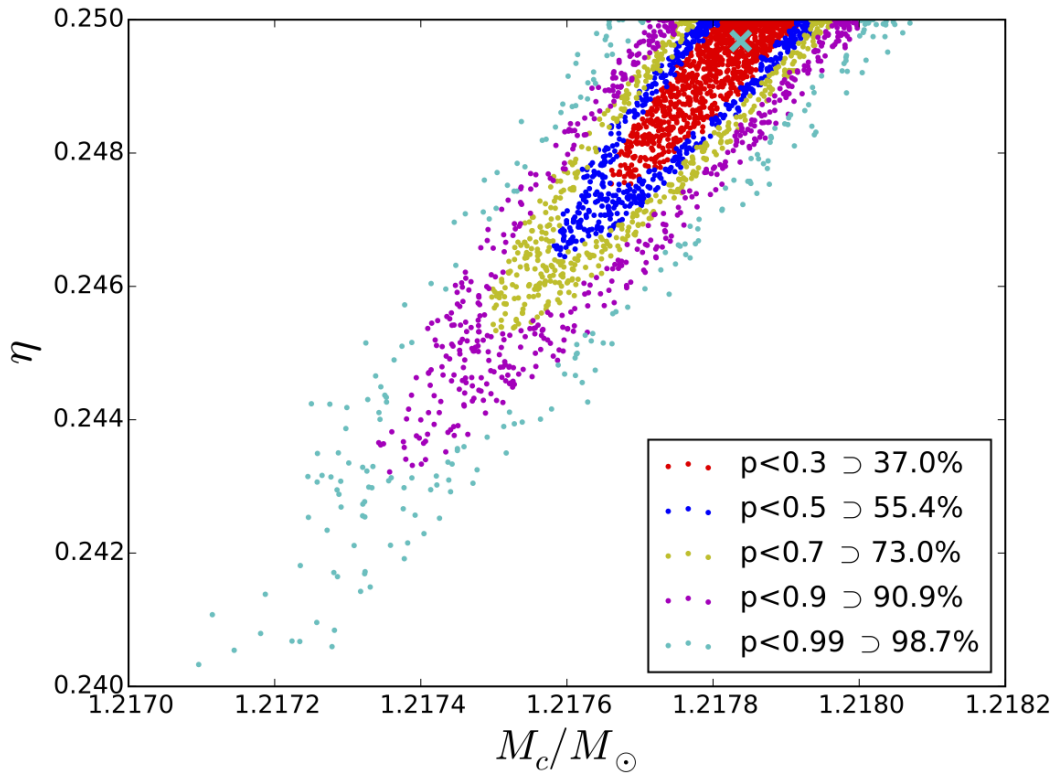

Figure 4.3 MCMC samples (dots) in $[\mathcal{M}_c, \eta]$ space are colour-coded by the credible region they fall into as determined by the *iso-match contour* bounding them. The legend compares these credible regions against the fraction of MCMC samples falling into them, which corresponds to the stochastic estimate of the fraction of posterior contained within. The true parameters of the evaluated BNS system are shown at the turquoise cross (corresponding to $m_1 = 1.45M_\odot$ and $m_2 = 1.35M_\odot$).

4.3.3 Comparasion

We compare all of the grid-based methods described above in Figure 4.4. We show the differences between the fraction of MCMC samples contained within the various methods for estimating credible regions corresponding to credible level p, and the value of p, for $p \in [0, 1]$. Perfect agreement would correspond to a horizontal line at a deviation of zero. However, the finite number of stochastic MCMC samples from `LALInferenceMCMC` leads to statistical fluctuations in the deviation; their expected magnitude is indicated by an error ellipse (see subsection 4.2.3) corresponding to one-σ fluctuations.

The cumulative posterior method, using a likelihood function marginalized over t_c and ϕ_c, successfully estimates credible regions (apparent deviations at $p < 0.3$ could be statistical, or may be due to the need for sub-pixel resolution to resolve such small credible regions). The comparison also further solidifies both the validity of the LSA for this system and the effect of the prior on the ability to recover consistent credible regions with respect to `LALInferenceMCMC`.

4.4 Conclusions and future directions

We have evaluated several grid-based methods for approximating the parameter credible regions for a CBC event, and compared these to regions estimated by the stochastic sampler `LALInferenceMCMC`. We found that evaluating the cumulative posterior on a relatively low-density grid allowed us to estimate credible regions to within the statistical uncertainty of the stochastic sampler at a small fraction of the computational cost ($\sim 0.1\%$), while marginalizing over the time and phase parameters and incorporating an arbitrary prior.

On the other hand, ignoring the prior or maximizing over t_c and ϕ_c instead of marginalizing over them introduces a discrepancy in the recovered credible regions with respect to `LALInferenceMCMC`. In addition, we have demonstrated that the iso-match method proposed by Baird *et al.* is overestimating the credible regions in $[\mathcal{M}_c, \eta]$ space compared to a full Bayesian analysis.

The analysis has been performed on a binary observed in one detector at a fixed overhead and optimally oriented position and at a fixed distance giving $\rho =$

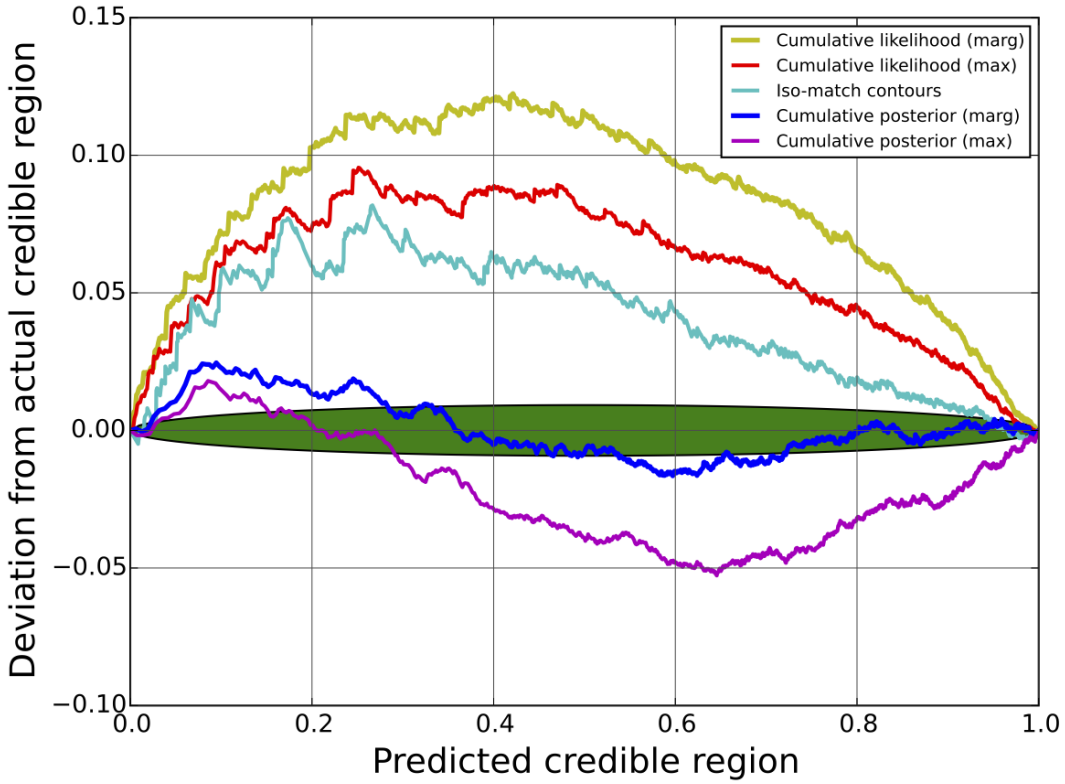

Figure 4.4 Difference between the fraction of MCMC samples from the posterior PDF falling into credible regions predicted by the various methods described above and the expected credible level p, as a function of p. Continuous relations for $p \in [0, 1]$ of the data in Figure 4.1, 4.2 and 4.3 are shown by five curves, corresponding, from the top down, to the cumulative marginalized likelihood, cumulative maximized likelihood, iso-match contours, cumulative marginalized posterior, and cumulative maximized posterior. The filled ellipse indicates the expected 68% level of fluctuation in the fraction of MCMC samples due to the finite number of samples.

12. Compared to an analysis of the same binary using a three-detector observation comprising data from the two LIGO observatories and the Virgo observatory (all operating at the same sensitivity as assumed in subsection 4.1.1), where extrinsic parameters describing sky location, inclination, orientation and distance are allowed to vary, the recovered two-dimensional credible region in $[\mathcal{M}_c, \eta]$ space, is not significantly altered (see Figure 4.5). The analysis is implemented with the same $[\mathcal{M}_c, \eta]$ grid as in previous figures, a grid designed for a two-dimensional analysis as described in subsection 4.2.2. The discrepancy, if any, introduced by allowing for eventual correlation caused by the inclusion of extrinsic parameters is found to be within the statistical uncertainty from the limited number of samples from `LALInferenceMCMC` (c.f. subsection 4.2.3).

The cumulative marginalized posterior method can easily be extended to include other parameters, especially spin [103], but as the computational cost scales exponentially with the number of parameters, the cost quickly approaches and exceeds the computational requirements of the stochastic sampler implemented in `LALInference`. Our simple grid-based sampling implementation would be computationally competitive with the stochastic sampling for parameter spaces with up to *four* non-marginalized dimensions. However, the computational cost of the grid-based sampler could be further reduced through more efficient grid placement and more accurate integration algorithms. Moreover, while standard stochastic samplers such as `LALInferenceMCMC` are serial processes, all pixels in the sampling grid are completely independent, therefore trivially allowing for massive parallelization of the cumulative marginalized posterior analysis.

Through these properties we envision the grid-based sampling method, using a cumulative marginalized posterior, to be implemented as a low-latency parameter estimation tool for the intrinsic parameters of a CBC candidate event, similar to the implementation of BAYESTAR for the extrinsic parameters [218, 216]. In practice, we won't know the true signal parameters which are needed for efficient and accurate grid placement. However, we can take the parameters of the highest-match template from the search pipelines used for the detection of CBC events [39, 65], which by design of the template banks will generally have $M > 0.97$ [178], as the central point of the grid. The size of the grid can be initially estimated by comparing the SNRs reported by adjacent templates in the template

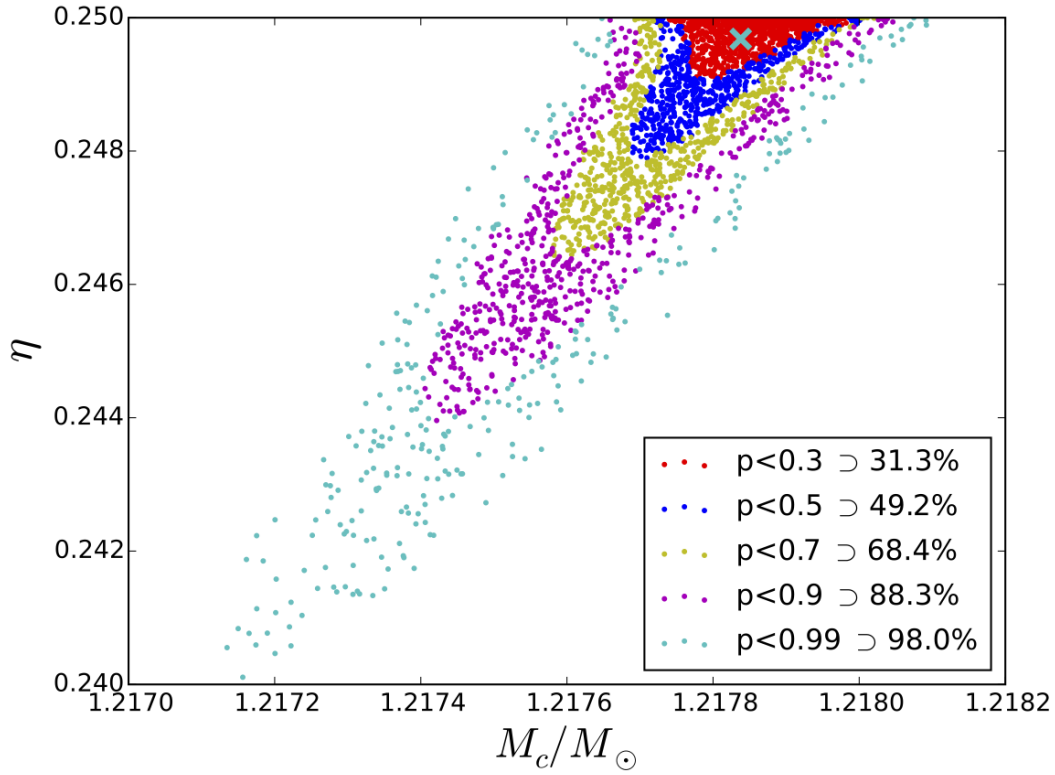

Figure 4.5 MCMC samples (dots), now 2955 independent samples drawn from a 9-dimensional analysis, in $[\mathcal{M}_c, \eta]$ space are colour-coded by the *cumulative marginalized posterior* credible region they fall into, using the same two-dimensional grid as in previous figures. The legend compares these credible regions against the fraction of MCMC samples falling into them, which corresponds to the stochastic estimate of the fraction of posterior contained within, now allowing for effects of correlation against extrinsic parameters. The true parameters of the evaluated BNS system are shown at the turquoise cross (corresponding to $m_1 = 1.45M_\odot$ and $m_2 = 1.35M_\odot$).

bank. Subsequently, the grid can be adaptively refined: while we used a grid with uniformly spaced pixels for this study, the computational cost could be reduced further by implementing a non-uniform grid. The reduction in the absolute number of pixels required within the grid can enable the inclusion of additional non-marginalized dimensions while retaining the computational competitiveness against the stochastic sampling methods. For example, in order to account for systematics associated with waveform model uncertainty, it is possible to introduce additional parameters (e.g., higher post-Newtonian orders with unknown coefficients). Alternatively, one could include the extensions to the likelihood function given by Moore *et al.* [169], analytically marginalizing over model uncertainties modeled by Gaussian processes, without increasing the dimensionality of the grid.

Additionally, a production-level implementation of the cumulative marginalized posterior method would need to address the extrinsic parameters, which were fixed at their true values in the example shown here as a proxy for maximization over these parameters. Although such maximization is adequate for extrinsic parameters which are decoupled from intrinsic ones, which is nearly the case for a non-precessing binary, it is also possible to efficiently marginalize over some of them, e.g., with a mixed analytical and numerical calculation as done in BAYESTAR [217], or implementing a Monte Carlo integral over the extrinsic parameter space (c.f. Pankow *et al.* [181]). While the second approach produces parameter estimates for all the extrinsic parameters, it does so at a much higher computational running time (worst case scenario wall time $\mathcal{O}(1\,\mathrm{hour})$) relative to BAYESTAR (median wall time $\mathcal{O}(10\,\mathrm{s})$ [51]).

Moreover, predictive methods such as the iso-match method [40, 103] or the effective Fisher matrix approach [68, 177] can be used in combination with the grid-based cumulative marginalized posterior technique to provide PDF estimates for dynamically laying out the grid. The cumulative marginalized posterior could also be implemented as a jump proposal for the intrinsic parameters as part of the stochastic samplers in `LALInference`. These possibilities will be explored further in future work.

In addition, it is important to note that even though the method of parameter estimation with the grid-based sampling using a cumulative marginalized poste-

rior has been presented here in the context of gravitational-wave astrophysics, the method itself is completely general and can be effective whenever the dimensionality of the parameter space is sufficiently small to make it competitive with stochastic samplers.

Chapter 5

Conclusion

In this thesis the concepts surrounding binaries of compact objects such as neutron stars and black holes have been considered in many of their aspects. The formation of a binary black hole, containing an intermediate mass black hole (IMBH), was shown in chapter 2 as part of a large N-body simulation of a globular cluster. For the first time, the inclusion of a comprehensive set of post-Newtonian corrections to the orbital dynamics around the IMBH, while it is embedded in a extended globular cluster potential, was presented. These pN effects were shown to play a significant role in the evolution of the IMBH–BH binary orbit, especially the suppression of Lidov-Kozai oscillations caused (when the binary is part of a hierarchical triple system) by the relativistic precession of the IMBH–BH binary orbit. Together with regular three body interactions the IMBH–BH binary is hardened until it is set on a merging trajectory dominated by emission of gravitational waves where it would be potentially observable in both future space-based gravitational wave observatories (e.g. eLISA) and current ground-based observatories (Advanced LIGO and Virgo). Further work would include extending the investigated simulation across a wider set of initial conditions, primarily in the size of the simulated cluster and the additional inclusion of more realistic models for stellar evolution and the cluster particle initial masses. This would also require simulations covering a longer timescale of the evolution of the clusters, which in turn would need further improvements of the computational efficiency of the code.

The work presented in chapter 3 follows the concepts from chapter 2 directly

in showing the capabilities of recovering the physical parameters of the type of compact binary formed in the simulated globular cluster. It was shown for the first time that an analysis of an Intermediate Mass Coalescence (IMRAC) which includes the full coalescence model of the detected waveform is necessary to fully capture the state of the binary during its merger, and that this analysis will be able to put strong constraints on the physical state of both the initial binary and the resulting black hole. Taking cosmological effects into account, it was shown that this analysis would be able to identify an IMBH at a 95% confidence given a source-frame mass of $\geq 130M_{\odot}$, giving the first conclusive evidence for the existence of IMBHs in the universe. This work also showed that uncertainties in the measured parameters were not dominated by uncertainties in the assumed waveform model. Following on the study presented in this chapter would primarily require a greater understanding of the realistic distributions of the parameters of the simulated systems, especially concerning the spins of the IMBH components. Additional simulations of the underlying source population, hopefully informed by detections of gravitational waves from systems like this, should be the main focus.

Finally, chapter 4 presents a new method for parameter estimation, which is demonstrated to have significantly improved computational efficiency without any measured losses in the accuracy of the recovered credible intervals when compared to the currently used stochastic models. By instead sampling the parameter space of interest in a predefined grid and semi-analytically marginalising over uninteresting parameters computational speedups of ~ 1000 were possible. This method was also compared against similar parameter estimation strategies to investigate whether additional computational gains were achievable, but the losses in accuracy brought by the alternative methods were found to be too damaging compared to the marginal computational speedups. The concepts presented in this chapter should be integrated as part of the rapid followup of gravitational wave trigger events, where additional optimisations and cross-talk against the current set of rapid analysis tools can further inform the setup of the required grid. It is also important to note that the method presented here would be applicable not only for gravitational wave parameter estimation, but as a general tool for efficient and accurate analysis of a low-dimensional parameter space.

REFERENCES

[1] Aarseth, S. J. (2012). Mergers and ejections of black holes in globular clusters. *MNRAS*, 422:841–848, 1202.4688.

[2] Aasi, J., Abadie, J., Abbott, B. P., Abbott, R., Abbott, T., Abernathy, M. R., Accadia, T., Acernese, F., Adams, C., Adams, T., and et al. (2013). Directed search for continuous gravitational waves from the Galactic center. *Phys. Rev. D*, 88(10):102002, 1309.6221.

[3] Aasi, J., Abadie, J., Abbott, B. P., Abbott, R., Abbott, T., Abernathy, M. R., Accadia, T., Acernese, F., Adams, C., Adams, T., and et al. (2014a). Application of a Hough search for continuous gravitational waves on data from the fifth LIGO science run. *Classical and Quantum Gravity*, 31(8):085014, 1311.2409.

[4] Aasi, J., Abadie, J., Abbott, B. P., Abbott, R., Abbott, T., Abernathy, M. R., Accadia, T., Acernese, F., Adams, C., Adams, T., and et al. (2014b). Constraints on Cosmic Strings from the LIGO-Virgo Gravitational-Wave Detectors. *Physical Review Letters*, 112(13):131101, 1310.2384.

[5] Aasi, J., Abadie, J., Abbott, B. P., Abbott, R., Abbott, T., Abernathy, M. R., Accadia, T., Acernese, F., Adams, C., Adams, T., and et al. (2014c). Gravitational Waves from Known Pulsars: Results from the Initial Detector Era. *Astrophysical Journal*, 785:119, 1309.4027.

[6] Aasi, J., Abadie, J., Abbott, B. P., Abbott, R., Abbott, T., Abernathy, M. R., Accadia, T., Acernese, F., Adams, C., Adams, T., and et al. (2015). Searching for stochastic gravitational waves using data from the two colocated LIGO Hanford detectors. *Phys. Rev. D*, 91(2):022003, 1410.6211.

[7] Aasi, J., Abbott, B. P., Abbott, R., Abbott, T., Abernathy, M. R., Accadia, T., Acernese, F., Ackley, K., Adams, C., Adams, T., and et al. (2014d). First all-sky search for continuous gravitational waves from unknown sources in binary systems. *Phys. Rev. D*, 90(6):062010, 1405.7904.

[8] Aasi, J., Abbott, B. P., Abbott, R., Abbott, T., Abernathy, M. R., Accadia, T., Acernese, F., Ackley, K., Adams, C., Adams, T., and et al. (2014e). Implementation of an F-statistic all-sky search for continuous gravitational waves in Virgo VSR1 data. *Classical and Quantum Gravity*, 31(16):165014, 1402.4974.

[9] Aasi, J., Abbott, B. P., Abbott, R., Abbott, T., Abernathy, M. R., Accadia, T., Acernese, F., Ackley, K., Adams, C., Adams, T., and et al. (2014f). Improved Upper Limits on the Stochastic Gravitational-Wave Background from 2009-2010 LIGO and Virgo Data. *Physical Review Letters*, 113(23):231101, 1406.4556.

[10] Aasi, J., Abbott, B. P., Abbott, R., Abbott, T., Abernathy, M. R., Accadia, T., Acernese, F., Ackley, K., Adams, C., Adams, T., and et al. (2014g). Search for gravitational radiation from intermediate mass black hole binaries in data from the second LIGO-Virgo joint science run. *Phys. Rev. D*, 89(12):122003, 1404.2199.

[11] Aasi, J. et al. (2013). Parameter estimation for compact binary coalescence signals with the first generation gravitational-wave detector network. *Phys. Rev. D*, 88:062001, 1304.1775.

[12] Aasi, J. et al. (2014). Search for gravitational wave ringdowns from perturbed intermediate mass black holes in LIGO–Virgo data from 2005–2010. *Phys. Rev. D*, 89(10):102006, 1403.5306.

[13] Aasi, J. et al. (2015). Advanced LIGO. *Class. Quant. Grav.*, 32:074001, 1411.4547.

[14] Abadie, J., Abbott, B. P., Abbott, R., Abbott, T. D., Abernathy, M., Accadia, T., Acernese, F., Adams, C., Adhikari, R., Affeldt, C., and et al. (2012a). All-sky search for gravitational-wave bursts in the second joint LIGO-Virgo run. *Phys. Rev. D*, 85(12):122007, 1202.2788.

[15] Abadie, J., Abbott, B. P., Abbott, R., Abbott, T. D., Abernathy, M., Accadia, T., Acernese, F., Adams, C., Adhikari, R., Affeldt, C., and et al. (2012b). Search for gravitational waves from intermediate mass binary black holes. *Phys. Rev. D*, 85(10):102004, 1201.5999.

[16] Abadie, J., Abbott, B. P., Abbott, R., Abernathy, M., Accadia, T., Acernese, F., Adams, C., Adhikari, R., Ajith, P., Allen, B., and et al. (2011). Directional Limits on Persistent Gravitational Waves Using LIGO S5 Science Data. *Physical Review Letters*, 107(27):271102, 1109.1809.

[17] Abadie, J. et al. (2010). Predictions for the rates of compact binary coalescences observable by ground-based gravitational-wave detectors. *Class. Quantum Grav.*, 27:173001.

[18] Abbott, B. P., Abbott, R., Abbott, T. D., Abernathy, M. R., Acernese, F., Ackley, K., Adams, C., Adams, T., Addesso, P., Adhikari, R. X., and et al. (2016a). All-sky search for long-duration gravitational wave transients with initial LIGO. *Phys. Rev. D*, 93(4):042005, 1511.04398.

[19] Abbott, B. P., Abbott, R., Abbott, T. D., Abernathy, M. R., Acernese, F., Ackley, K., Adams, C., Adams, T., Addesso, P., Adhikari, R. X., and et al. (2016b). Astrophysical Implications of the Binary Black-hole Merger GW150914. *Astrophysical Journal*, 818:L22, 1602.03846.

[20] Abbott, B. P., Abbott, R., Abbott, T. D., Abernathy, M. R., Acernese, F., Ackley, K., Adams, C., Adams, T., Addesso, P., Adhikari, R. X., and et al. (2016c). GW150914: Implications for the Stochastic Gravitational-Wave Background from Binary Black Holes. *Physical Review Letters*, 116(13):131102, 1602.03847.

[21] Abbott, B. P., Abbott, R., Abbott, T. D., Abernathy, M. R., Acernese, F., Ackley, K., Adams, C., Adams, T., Addesso, P., Adhikari, R. X., and et al. (2016d). GW150914: The Advanced LIGO Detectors in the Era of First Discoveries. *Physical Review Letters*, 116(13):131103, 1602.03838.

[22] Abbott, B. P., Abbott, R., Abbott, T. D., Abernathy, M. R., Acernese, F., Ackley, K., Adams, C., Adams, T., Addesso, P., Adhikari, R. X., and et al. (2016e). Observation of Gravitational Waves from a Binary Black Hole Merger. *Physical Review Letters*, 116(6):061102, 1602.03837.

[23] Abbott, B. P., Abbott, R., Abbott, T. D., Abernathy, M. R., Acernese, F., Ackley, K., Adams, C., Adams, T., Addesso, P., Adhikari, R. X., and et al. (2016f). The Rate of Binary Black Hole Mergers Inferred from Advanced LIGO Observations Surrounding GW150914. *ArXiv e-prints*, 1602.03842.

[24] Abbott, B. P., Abbott, R., Acernese, F., Adhikari, R., Ajith, P., Allen, B., Allen, G., Alshourbagy, M., Amin, R. S., Anderson, S. B., and et al. (2009a). An upper limit on the stochastic gravitational-wave background of cosmological origin. *Nature*, 460:990–994, 0910.5772.

[25] Abbott, B. P., Abbott, R., Adhikari, R., Ajith, P., Allen, B., Allen, G., Amin, R. S., Anderson, S. B., Anderson, W. G., Arain, M. A., and et al. (2009b). Search for gravitational waves from low mass binary coalescences in the first year of LIGO's S5 data. *Phys. Rev. D*, 79(12):122001, 0901.0302.

[26] Abbott, B. P. et al. (2016). Prospects for Observing and Localizing Gravitational-Wave Transients with Advanced LIGO and Advanced Virgo. *Living Rev. Relat.*, 19:1, 1304.0670.

[27] Acernese, F., Alshourbagy, M., Antonucci, F., et al. (2009). Advanced virgo baseline design. Virgo Technical Report VIR-0027A-09.

[28] Acernese, F. et al. (2015). Advanced Virgo: a second-generation interferometric gravitational wave detector. *Class. Quant. Grav.*, 32(2):024001, 1408.3978.

[29] Allen, B. (2005). χ^2 time-frequency discriminator for gravitational wave detection. *Phys. Rev. D*, 71(6):062001, gr-qc/0405045.

[30] Allen, B., Creighton, J. D., Flanagan, É. É., and Romano, J. D. (2002). Robust statistics for deterministic and stochastic gravitational waves in non-Gaussian noise: Frequentist analyses. *Phys. Rev. D*, 65(12):122002, gr-qc/0105100.

[31] Allen, B., Creighton, J. D., Flanagan, É. É., and Romano, J. D. (2003). Robust statistics for deterministic and stochastic gravitational waves in non-Gaussian noise. II. Bayesian analyses. *Phys. Rev. D*, 67(12):122002, gr-qc/0205015.

[32] Amaro-Seoane, P. and Freitag, M. (2006). Intermediate-Mass Black Holes in Colliding Clusters: Implications for Lower Frequency Gravitational-Wave Astronomy. *Astrophysical Journal*, 653:L53–L56, arXiv:astro-ph/0610478.

[33] Amaro-Seoane, P., Gair, J. R., Freitag, M., Coleman Miller, M., Mandel, I., Cutler, C. J., and Babak, S. (2007). Astrophysics, detection and science applications of intermediate- and extreme mass-ratio inspirals. *Class. Quant. Grav.*, 24:R113–R169, astro-ph/0703495.

[34] Amaro-Seoane, P., Gair, J. R., Freitag, M., Miller, M. C., Mandel, I., Cutler, C. J., and Babak, S. (2007). TOPICAL REVIEW: Intermediate and extreme mass-ratio inspirals–astrophysics, science applications and detection using LISA. *Classical and Quantum Gravity*, 24:R113–R169, astro-ph/0703495.

[35] Amaro-Seoane, P. and Santamaría, L. (2010). Detection of IMBHs with Ground-based Gravitational Wave Observatories: A Biography of a Binary of Black Holes, from Birth to Death. *Astrophysical Journal*, 722:1197–1206, 0910.0254.

[36] Antonini, F., Chatterjee, S., Rodriguez, C. L., Morscher, M., Pattabiraman, B., Kalogera, V., and Rasio, F. A. (2016a). Black Hole Mergers and Blue Stragglers from Hierarchical Triples Formed in Globular Clusters. *Astrophysical Journal*, 816:65, 1509.05080.

[37] Antonini, F., Hamers, A. S., and Lithwick, Y. (2016b). Dynamical constraints on the origin of hot and warm Jupiters with close friends. *ArXiv e-prints*, 1604.01781.

[38] Antonini, F., Murray, N., and Mikkola, S. (2014). Black Hole Triple Dynamics: A Breakdown of the Orbit Average Approximation and Implications for Gravitational Wave Detections. *Astrophysical Journal*, 781:45, 1308.3674.

[39] Babak, S., Biswas, R., Brady, P. R., Brown, D. A., Cannon, K., Capano, C. D., Clayton, J. H., Cokelaer, T., Creighton, J. D. E., Dent, T., Dietz, A.,

Fairhurst, S., Fotopoulos, N., González, G., Hanna, C., Harry, I. W., Jones, G., Keppel, D., McKechan, D. J. A., Pekowsky, L., Privitera, S., Robinson, C., Rodriguez, A. C., Sathyaprakash, B. S., Sengupta, A. S., Vallisneri, M., Vaulin, R., and Weinstein, A. J. (2013). Searching for gravitational waves from binary coalescence. *Phys. Rev. D*, 87(2):024033, 1208.3491.

[40] Baird, E., Fairhurst, S., Hannam, M., and Murphy, P. (2013). Degeneracy between mass and spin in black-hole-binary waveforms. *Phys. Rev. D*, 87:024035.

[41] Baker, J. G., Centrella, J., Choi, D.-I., Koppitz, M., and van Meter, J. (2006). Gravitational-Wave Extraction from an Inspiraling Configuration of Merging Black Holes. *Physical Review Letters*, 96(11):111102, gr-qc/0511103.

[42] Barausse, E. and Buonanno, A. (2010). Improved effective-one-body Hamiltonian for spinning black-hole binaries. *Phys. Rev. D*, 81(8):084024, 0912.3517.

[43] Belczynski, K., Buonanno, A., Cantiello, M., Fryer, C. L., Holz, D. E., Mandel, I., Miller, M. C., and Walczak, M. (2014). The Formation and Gravitational-Wave Detection of Massive Stellar Black-Hole Binaries. *Astrophys. J.*, 789(2):120, 1403.0677.

[44] Belczynski, K., Dominik, M., Bulik, T., O'Shaughnessy, R., Fryer, C., and Holz, D. E. (2010). The Effect of Metallicity on the Detection Prospects for Gravitational Waves. *Astrophysical Journal*, 715:L138–L141, 1004.0386.

[45] Belczynski, K., Holz, D. E., Bulik, T., and O'Shaughnessy, R. (2016a). The origin and evolution of LIGO's first gravitational-wave source. *ArXiv e-prints*, 1602.04531.

[46] Belczynski, K., Kalogera, V., Rasio, F. A., Taam, R. E., Zezas, A., Bulik, T., Maccarone, T. J., and Ivanova, N. (2008). Compact Object Modeling with the StarTrack Population Synthesis Code. *ApJS*, 174:223–260, astro-ph/0511811.

[47] Belczynski, K., Repetto, S., Holz, D. E., O'Shaughnessy, R., Bulik, T., Berti, E., Fryer, C., and Dominik, M. (2016b). Compact Binary Merger Rates: Comparison with LIGO/Virgo Upper Limits. *Astrophysical Journal*, 819:108, 1510.04615.

[48] Belczynski, K., Wiktorowicz, G., Fryer, C. L., Holz, D. E., and Kalogera, V. (2012). Missing Black Holes Unveil the Supernova Explosion Mechanism. *Astrophysical Journal*, 757:91, 1110.1635.

[49] Berghea, C. T., Weaver, K. A., Colbert, E. J. M., and Roberts, T. P. (2008). Testing the Paradigm that Ultraluminous X-Ray Sources as a Class Represent Accreting Intermediate-Mass Black Holes. *Astrophysical Journal*, 687:471–487, 0807.1547.

[50] Berry, C. P. L. and Gair, J. R. (2013). Observing the Galaxy's massive black hole with gravitational wave bursts. *MNRAS*, 429:589–612, 1210.2778.

[51] Berry, C. P. L., Mandel, I., Middleton, H., Singer, L. P., Urban, A. L., Vecchio, A., Vitale, S., Cannon, K., Farr, B., Farr, W. M., Graff, P. B., Hanna, C., Haster, C.-J., Mohapatra, S., Pankow, C., Price, L. R., Sidery, T., and Veitch, J. (2015). Parameter Estimation for Binary Neutron-star Coalescences with Realistic Noise during the Advanced LIGO Era. *Astrophysical Journal*, 804:114, 1411.6934.

[52] Berti, E., Cardoso, V., and Will, C. M. (2006). On gravitational-wave spectroscopy of massive black holes with the space interferometer LISA. *Phys. Rev. D*, 73:064030, gr-qc/0512160.

[53] Biswas, R., Brady, P. R., Burguet-Castell, J., Cannon, K., Clayton, J., Dietz, A., Fotopoulos, N., Goggin, L. M., Keppel, D., Pankow, C., Price, L. R., and Vaulin, R. (2012a). Detecting transient gravitational waves in non-Gaussian noise with partially redundant analysis methods. *Phys. Rev. D*, 85(12):122009, 1201.2964.

[54] Biswas, R., Brady, P. R., Burguet-Castell, J., Cannon, K., Clayton, J., Dietz, A., Fotopoulos, N., Goggin, L. M., Keppel, D., Pankow, C., Price, L. R., and Vaulin, R. (2012b). Likelihood-ratio ranking of gravitational-wave candidates in a non-Gaussian background. *Phys. Rev. D*, 85(12):122008, 1201.2959.

[55] Blanchet, L. (2014). Gravitational Radiation from Post-Newtonian Sources and Inspiralling Compact Binaries. *Living Reviews in Relativity*, 17, 1310.1528.

[56] Blanchet, L., Damour, T., Iyer, B. R., Will, C. M., and Wiseman, A. G. (1995). Gravitational-radiation damping of compact binary systems to second post-newtonian order. *Phys. Rev. Lett.*, 74:3515–3518.

[57] Bode, J. N. and Wegg, C. (2014). Production of EMRIs in supermassive black hole binaries. *MNRAS*, 438:573–589.

[58] Brown, D. A., Brink, J., Fang, H., Gair, J. R., Li, C., Lovelace, G., Mandel, I., and Thorne, K. S. (2007). Prospects for Detection of Gravitational Waves from Intermediate-Mass-Ratio Inspirals. *Physical Review Letters*, 99(20):201102, gr-qc/0612060.

[59] Brown, D. A., Fang, H., Gair, J. R., Li, C., Lovelace, G., Mandel, I., and Thorne, K. S. (2007). Prospects for detection of gravitational waves from intermediate-mass-ratio inspirals. *Phys. Rev. Lett.*, 99:201102, gr-qc/0612060.

[60] Brown, D. A., Harry, I., Lundgren, A., and Nitz, A. H. (2012). Detecting binary neutron star systems with spin in advanced gravitational-wave detectors. *Phys. Rev. D*, 86(8):084017, 1207.6406.

[61] Buonanno, A. and Damour, T. (1999). Effective one-body approach to general relativistic two-body dynamics. *Phys. Rev. D*, 59(8):084006, gr-qc/9811091.

[62] Buonanno, A. and Damour, T. (2000). Transition from inspiral to plunge in binary black hole coalescences. *Phys. Rev. D*, 62(6):064015, gr-qc/0001013.

[63] Buonanno, A., Iyer, B. R., Ochsner, E., Pan, Y., and Sathyaprakash, B. S. (2009). Comparison of post-newtonian templates for compact binary inspiral signals in gravitational-wave detectors. *Phys. Rev. D*, 80:084043.

[64] Campanelli, M., Lousto, C. O., Marronetti, P., and Zlochower, Y. (2006). Accurate Evolutions of Orbiting Black-Hole Binaries without Excision. *Physical Review Letters*, 96(11):111101, gr-qc/0511048.

[65] Cannon, K. et al. (2012). Toward early-warning detection of gravitational waves from compact binary coalescence. *The Astrophysical Journal*, 748(2):136.

[66] Capano, C., Harry, I., Privitera, S., and Buonanno, A. (2016). Implementing a search for gravitational waves from non-precessing, spinning binary black holes. *ArXiv e-prints*, 1602.03509.

[67] Chatterjee, S., Rodriguez, C. L., and Rasio, F. A. (2016). Binary Black Holes in Dense Star Clusters: Exploring the Theoretical Uncertainties. *ArXiv e-prints*, 1603.00884.

[68] Cho, H.-S., Ochsner, E., O'Shaughnessy, R., Kim, C., and Lee, C.-H. (2013). Gravitational waves from black hole-neutron star binaries: Effective fisher matrices and parameter estimation using higher harmonics. *Phys. Rev. D*, 87:024004.

[69] Connaughton, V., Burns, E., Goldstein, A., Briggs, M. S., Zhang, B.-B., Hui, C. M., Jenke, P., Racusin, J., Wilson-Hodge, C. A., Bhat, P. N., Bissaldi, E., Cleveland, W., Fitzpatrick, G., Giles, M. M., Gibby, M. H., Greiner, J., von Kienlin, A., Kippen, R. M., McBreen, S., Mailyan, B., Meegan, C. A., Paciesas, W. S., Preece, R. D., Roberts, O., Sparke, L., Stanbro, M., Toelge, K., Veres, P., Yu, H.-F., and authors, o. (2016). Fermi GBM Observations of LIGO Gravitational Wave event GW150914. *ArXiv e-prints*, 1602.03920.

[70] Cutler, C. and Flanagan, É. E. (1994). Gravitational waves from merging compact binaries: How accurately can one extract the binary's parameters from the inspiral waveform\? *Phys. Rev. D*, 49:2658–2697, gr-qc/9402014.

[71] Damour, T. and Deruelle, N. (1985). General relativistic celestial mechanics of binary systems. I. The post-Newtonian motion. *Ann. Inst. Henri Poincaré Phys. Théor., Vol. 43, No. 1, p. 107 - 132*, 43:107–132.

[72] Damour, T., Jaranowski, P., and Schäfer, G. (2008). Effective one body approach to the dynamics of two spinning black holes with next-to-leading order spin-orbit coupling. *Phys. Rev. D*, 78(2):024009, 0803.0915.

[73] Damour, T. and Nagar, A. (2009). Improved analytical description of inspiralling and coalescing black-hole binaries. *Phys. Rev. D*, 79(8):081503, 0902.0136.

[74] Davis, S. W., Narayan, R., Zhu, Y., Barret, D., Farrell, S. A., Godet, O., Servillat, M., and Webb, N. A. (2011). The Cool Accretion Disk in ESO 243-49 HLX-1: Further Evidence of an Intermediate-mass Black Hole. *Astrophysical Journal*, 734:111, 1104.2614.

[75] de Mink, S. E. and Mandel, I. (2016). The chemically homogeneous evolutionary channel for binary black hole mergers: Rates and Properties of gravitational-wave events detectable by advanced LIGO. *MNRAS*, 1603.02291.

[76] Dominik, M., Belczynski, K., Fryer, C., Holz, D. E., Berti, E., Bulik, T., Mandel, I., and O'Shaughnessy, R. (2012). Double Compact Objects. I. The Significance of the Common Envelope on Merger Rates. *Astrophysical Journal*, 759:52, 1202.4901.

[77] Dominik, M., Belczynski, K., Fryer, C., Holz, D. E., Berti, E., Bulik, T., Mandel, I., and O'Shaughnessy, R. (2013). Double Compact Objects. II. Cosmological Merger Rates. *Astrophysical Journal*, 779:72, 1308.1546.

[78] Dominik, M., Berti, E., O'Shaughnessy, R., Mandel, I., Belczynski, K., Fryer, C., Holz, D. E., Bulik, T., and Pannarale, F. (2015). Double Compact Objects III: Gravitational-wave Detection Rates. *Astrophysical Journal*, 806:263, 1405.7016.

[79] Downing, J. M. B., Benacquista, M. J., Giersz, M., and Spurzem, R. (2010). Compact binaries in star clusters - I. Black hole binaries inside globular clusters. *MNRAS*, 407:1946–1962, 0910.0546.

[80] Downing, J. M. B., Benacquista, M. J., Giersz, M., and Spurzem, R. (2011). Compact binaries in star clusters - II. Escapers and detection rates. *MNRAS*, 416:133–147, 1008.5060.

[81] Echeverria, F. (1989). Gravitational-wave measurements of the mass and angular momentum of a black hole. *Phys. Rev. D*, 40:3194–3203.

[82] Einstein, A. (1916). Approximative Integration of the Field Equations of Gravitation. *Preuss. Akad. Wiss. Berlin*, page 688.

[83] Einstein, A. (1918). Über Gravitationswellen. *Preuss. Akad. Wiss. Berlin*, pages 154–167.

[84] eLISA Consortium (2013). The Gravitational Universe. *ArXiv e-prints*, 1305.5720.

[85] Farr, W. M., Sravan, N., Cantrell, A., Kreidberg, L., Bailyn, C. D., Mandel, I., and Kalogera, V. (2011). The Mass Distribution of Stellar-mass Black Holes. *Astrophysical Journal*, 741:103, 1011.1459.

[86] Farrell, S. A., Webb, N. A., Barret, D., Godet, O., and Rodrigues, J. M. (2009). An intermediate-mass black hole of over 500 solar masses in the galaxy ESO243-49. *Nature*, 460:73–75.

[87] Favata, M. (2014). Systematic Parameter Errors in Inspiraling Neutron Star Binaries. *Physical Review Letters*, 112(10):101101, 1310.8288.

[88] Feng, H. and Soria, R. (2011). Ultraluminous X-ray Sources in the Chandra and XMM-Newton Era. *New Astron. Rev.*, 55:166–183, 1109.1610.

[89] Feroz, F., Gair, J. R., Hobson, M. P., and Porter, E. K. (2009). Use of the MULTINEST algorithm for gravitational wave data analysis. *Classical and Quantum Gravity*, 26(21):215003, 0904.1544.

[90] Fregeau, J. M., Larson, S. L., Miller, M. C., O'Shaughnessy, R. W., and Rasio, F. A. (2006). Observing IMBH-IMBH Binary Coalescences via Gravitational Radiation. *Astrophys. J.*, 646:L135–L138, astro-ph/0605732.

[91] Freitag, M., Rasio, F. A., and Baumgardt, H. (2006). Runaway collisions in young star clusters. 1. Methods and tests. *Mon. Not. Roy. Astron. Soc.*, 368:121–140, astro-ph/0503129.

[92] Gaburov, E., Harfst, S., and Portegies Zwart, S. (2009). SAPPORO: A way to turn your graphics cards into a GRAPE-6. *New Astronomy*, 14:630–637, 0902.4463.

[93] Gair, J. R., Li, C., and Mandel, I. (2008). Observable Properties of Orbits in Exact Bumpy Spacetimes. *Phys. Rev. D*, 77:024035, 0708.0628.

[94] Gill, M., Trenti, M., Miller, M. C., van der Marel, R., Hamilton, D., and Stiavelli, M. (2008). Intermediate Mass Black Hole Induced Quenching of Mass Segregation in Star Clusters. *Astrophys. J.*, 686:303, 0806.4187.

[95] Godet, O., Lombardi, J. C., Antonini, F., Barret, D., Webb, N. A., Vingless, J., and Thomas, M. (2014). Implications of the Delayed 2013 Outburst of ESO 243-49 HLX-1. *Astrophysical Journal*, 793:105, 1408.1819.

[96] González, J. A., Sperhake, U., Brügmann, B., Hannam, M., and Husa, S. (2007). Maximum Kick from Nonspinning Black-Hole Binary Inspiral. *Physical Review Letters*, 98(9):091101, gr-qc/0610154.

[97] Graff, P., Feroz, F., Hobson, M. P., and Lasenby, A. (2012). BAMBI: blind accelerated multimodal Bayesian inference. *MNRAS*, 421:169–180, 1110.2997.

[98] Graff, P. B., Buonanno, A., and Sathyaprakash, B. (2015). Missing Link: Bayesian detection and measurement of intermediate-mass black-hole binaries. *Phys. Rev.*, D92(2):022002, 1504.04766.

[99] Graham, A. W. and Scott, N. (2013). The M $_{BH}$-L $_{spheroid}$ Relation at High and Low Masses, the Quadratic Growth of Black Holes, and Intermediate-mass Black Hole Candidates. *Astrophysical Journal*, 764:151, 1211.3199.

[100] Gültekin, K., Miller, M. C., and Hamilton, D. P. (2004). Growth of Intermediate-Mass Black Holes in Globular Clusters. *Astrophysical Journal*, 616:221–230, arXiv:astro-ph/0402532.

[101] Gültekin, K., Miller, M. C., and Hamilton, D. P. (2006). Three-Body Dynamics with Gravitational Wave Emission. *Astrophysical Journal*, 640:156–166, arXiv:astro-ph/0509885.

[102] Hamers, A. S., Perets, H. B., Antonini, F., and Portegies Zwart, S. F. (2015). Secular dynamics of hierarchical quadruple systems: the case of a triple system orbited by a fourth body. *MNRAS*, 449:4221–4245, 1412.3115.

[103] Hannam, M., Brown, D. A., Fairhurst, S., Fryer, C. L., and Harry, I. W. (2013). When can gravitational-wave observations distinguish between black holes and neutron stars? *The Astrophysical Journal Letters*, 766(1):L14.

[104] Hannam, M., Schmidt, P., Bohé, A., Haegel, L., Husa, S., Ohme, F., Pratten, G., and Pürrer, M. (2014). Simple Model of Complete Precessing Black-Hole-Binary Gravitational Waveforms. *Physical Review Letters*, 113(15):151101, 1308.3271.

[105] Harfst, S., Gualandris, A., Merritt, D., and Mikkola, S. (2008). A hybrid N-body code incorporating algorithmic regularization and post-Newtonian forces. *MNRAS*, 389:2–12, 0803.2310.

[106] Harry, G. M. and the LIGO Scientific Collaboration (2010). Advanced LIGO: the next generation of gravitational wave detectors. *Class. Quantum Gravity*, 27(8):084006, arXiv:1103.2728.

[107] Harry, I., Privitera, S., Bohé, A., and Buonanno, A. (2016). Searching for Gravitational Waves from Compact Binaries with Precessing Spins. *ArXiv e-prints*, 1603.02444.

[108] Haster, C.-J., Antonini, F., Kalogera, V., and Mandel, I. (2016a). N-body dynamics of intermediate mass-ratio inspirals. In preparation.

[109] Haster, C.-J., Mandel, I., and Farr, W. M. (2015). Efficient method for measuring the parameters encoded in a gravitational-wave signal. *Classical and Quantum Gravity*, 32(23):235017, 1502.05407.

[110] Haster, C.-J., Wang, Z., Berry, C. P. L., Stevenson, S., Veitch, J., and Mandel, I. (2016b). Inference on gravitational waves from coalescences of stellar-mass compact objects and intermediate-mass black holes. *MNRAS*, 457:4499–4506, 1511.01431.

[111] Hastings, W. K. (1970). Monte carlo sampling methods using markov chains and their applications. *Biometrika*, 57(1):97–109.

[112] Healy, J., Lousto, C. O., and Zlochower, Y. (2014). Remnant mass, spin, and recoil from spin aligned black-hole binaries. *Phys. Rev. D*, 90(10):104004, 1406.7295.

[113] Heggie, D. C., Trenti, M., and Hut, P. (2006). Star clusters with primordial binaries - I. Dynamical evolution of isolated models. *MNRAS*, 368:677–689, astro-ph/0602408.

[114] Hinderer, T., Taracchini, A., Foucart, F., Buonanno, A., Steinhoff, J., Duez, M., Kidder, L. E., Pfeiffer, H. P., Scheel, M. A., Szilagyi, B., Hotokezaka, K., Kyutoku, K., Shibata, M., and Carpenter, C. W. (2016). Effects of Neutron-Star Dynamic Tides on Gravitational Waveforms within the Effective-One-Body Approach. *Physical Review Letters*, 116(18):181101, 1602.00599.

[115] Hobson, M. P., Efstathiou, G., and Lasenby, A. (2006). *General Relativity: An Introduction for Physicists*. Cambridge University Press, Cambridge.

[116] Holman, M., Touma, J., and Tremaine, S. (1997). Chaotic variations in the eccentricity of the planet orbiting 16 Cygni B. *Nature*, 386:254–256.

[117] Holz, D. E. and Hughes, S. A. (2005). Using Gravitational-Wave Standard Sirens. *Astrophysical Journal*, 629:15–22, astro-ph/0504616.

[118] Huerta, E. A., Kumar, P., McWilliams, S. T., O'Shaughnessy, R., and Yunes, N. (2014). Accurate and efficient waveforms for compact binaries on eccentric orbits. *Phys. Rev. D*, 90(8):084016, 1408.3406.

[119] Hulse, R. A. and Taylor, J. H. (1975). Discovery of a pulsar in a binary system. *Astrophysical Journal*, 195:L51–L53.

[120] Husa, S., Khan, S., Hannam, M., Pürrer, M., Ohme, F., Forteza, X. J., and Bohé, A. (2016). Frequency-domain gravitational waves from nonprecessing black-hole binaries. I. New numerical waveforms and anatomy of the signal. *Phys. Rev. D*, 93(4):044006, 1508.07250.

[121] Innanen, K. A., Zheng, J. Q., Mikkola, S., and Valtonen, M. J. (1997). The Kozai Mechanism and the Stability of Planetary Orbits in Binary Star Systems. *Astronomical Journal*, 113:1915.

[122] Iyer, B., Souradeep, T., Unnikrishnan, C., Dhurandhar, S., Raja, S., Kumar, A., and Sengupta, A. S. (2011). LIGO-India Tech. rep.

[123] Jaranowski, P. and Królak, A. (2012). Gravitational-Wave Data Analysis. Formalism and Sample Applications: The Gaussian Case. *Living Reviews in Relativity*, 15.

[124] Kalogera, V., Belczynski, K., Kim, C., O'Shaughnessy, R., and Willems, B. (2007). Formation of double compact objects. *Physics Reports*, 442:75–108, astro-ph/0612144.

[125] Key, J. S. and Cornish, N. J. (2011). Characterizing spinning black hole binaries in eccentric orbits with LISA. *Phys. Rev. D*, 83(8):083001, 1006.3759.

[126] Khan, S., Husa, S., Hannam, M., Ohme, F., Pürrer, M., Forteza, X. J., and Bohé, A. (2016). Frequency-domain gravitational waves from nonprecessing black-hole binaries. II. A phenomenological model for the advanced detector era. *Phys. Rev. D*, 93(4):044007, 1508.07253.

[127] Kobulnicky, H. A., Kiminki, D. C., Lundquist, M. J., Burke, J., Chapman, J., Keller, E., Lester, K., Rolen, E. K., Topel, E., Bhattacharjee, A., Smullen, R. A., Vargas Álvarez, C. A., Runnoe, J. C., Dale, D. A., and Brotherton, M. M. (2014). Toward Complete Statistics of Massive Binary Stars: Penultimate Results from the Cygnus OB2 Radial Velocity Survey. *ApJS*, 213:34, 1406.6655.

[128] Konstantinidis, S., Amaro-Seoane, P., and Kokkotas, K. D. (2013). Investigating the retention of intermediate-mass black holes in star clusters using N-body simulations. *A&A*, 557:A135, 1108.5175.

[129] Kozai, Y. (1962). Secular perturbations of asteroids with high inclination and eccentricity. *Astronomical Journal*, 67:591.

[130] Kramer, M., Stairs, I. H., Manchester, R. N., McLaughlin, M. A., Lyne, A. G., Ferdman, R. D., Burgay, M., Lorimer, D. R., Possenti, A., D'Amico, N., Sarkissian, J. M., Hobbs, G. B., Reynolds, J. E., Freire, P. C. C., and Camilo, F. (2006). Tests of General Relativity from Timing the Double Pulsar. *Science*, 314:97–102, astro-ph/0609417.

[131] Kreidberg, L., Bailyn, C. D., Farr, W. M., and Kalogera, V. (2012). Mass Measurements of Black Holes in X-Ray Transients: Is There a Mass Gap? *Astrophysical Journal*, 757:36, 1205.1805.

[132] Kruijssen, J. M. D. (2012). On the fraction of star formation occurring in bound stellar clusters. *MNRAS*, 426:3008–3040, 1208.2963.

[133] Lattimer, J. M. (2012). The Nuclear Equation of State and Neutron Star Masses. *Annual Review of Nuclear and Particle Science*, 62:485–515, 1305.3510.

[134] Leigh, N. W. C., Lützgendorf, N., Geller, A. M., Maccarone, T. J., Heinke, C., and Sesana, A. (2014). On the coexistence of stellar-mass and intermediate-mass black holes in globular clusters. *MNRAS*, 444:29–42, 1407.4459.

[135] Lidov, M. L. (1962). The evolution of orbits of artificial satellites of planets under the action of gravitational perturbations of external bodies. *Planetary and Space Science*, 9:719–759.

[136] LIGO Scientific Collaboration (2010a). Advanced LIGO anticipated sensitivity curves. https://dcc.ligo.org/cgi-bin/DocDB/ShowDocument?docid=2974.

[137] LIGO Scientific Collaboration (2010b). H1 Sensitivity, 15 May 2010. http://labcit.ligo.caltech.edu/~jzweizig/distribution/LSC_Data/S6/.

[138] LIGO Scientific Collaboration (2015). H1 Calibrated Sensitivity Spectra Oct 1 2015 (Representative for Start of O1). Document number G1501223-v3 https://dcc.ligo.org/LIGO-G1501223/public.

[139] Littenberg, T. B. and Cornish, N. J. (2015). Bayesian inference for spectral estimation of gravitational wave detector noise. *Phys. Rev. D*, 91(8):084034, 1410.3852.

[140] Littenberg, T. B., Farr, B., Coughlin, S., Kalogera, V., and Holz, D. E. (2015). Neutron Stars versus Black Holes: Probing the Mass Gap with LIGO/Virgo. *Astrophysical Journal*, 807:L24, 1503.03179.

[141] Liu, Q. Z., van Paradijs, J., and van den Heuvel, E. P. J. (2007). A catalogue of low-mass X-ray binaries in the Galaxy, LMC, and SMC (Fourth edition). *A&A*, 469:807–810, 0707.0544.

[142] Lousto, C. O., Nakano, H., Zlochower, Y., and Campanelli, M. (2010). Intermediate Mass Ratio Black Hole Binaries: Numerical Relativity meets Perturbation Theory. *Phys. Rev. Lett.*, 104:211101, 1001.2316.

[143] Lyon, R. J., Stappers, B. W., Cooper, S., Brooke, J. M., and Knowles, J. D. (2016). Fifty Years of Pulsar Candidate Selection: From simple filters to a new principled real-time classification approach. *Accepted for publication in MNRAS*, astro-ph.IM.

[144] Lyutikov, M. (2016). Fermi GBM signal contemporaneous with GW150914 - an unlikely association. *ArXiv e-prints*, 1602.07352.

[145] Maccarone, T. J. and Servillat, M. (2008). Radio observations of NGC 2808 and other globular clusters: constraints on intermediate-mass black holes. *MNRAS*, 389:379–384, 0806.2387.

[146] MacLeod, M., Trenti, M., and Ramirez-Ruiz, E. (2016). The Close Stellar Companions to Intermediate-mass Black Holes. *Astrophysical Journal*, 819:70, 1508.07000.

[147] Maggiore, M. (2008). *Gravitational Waves Volume 1: Theory and Experiments*. Oxford University Press.

[148] Mahalanobis, P. C. (1936). On the generalised distance in statistics. *Proceedings of the National Institute of Sciences of India*, 2(1):49–55.

[149] Mandel, I. (2007). Spin distribution following minor mergers and the effect of spin on the detection range for low-mass-ratio inspirals. *ArXiv e-prints*, 0707.0711.

[150] Mandel, I. (2010). Parameter estimation on gravitational waves from multiple coalescing binaries. *Phys. Rev. D*, 81(8):084029, 0912.5531.

[151] Mandel, I., Brown, D. A., Gair, J. R., and Miller, M. C. (2008). Rates and Characteristics of Intermediate Mass Ratio Inspirals Detectable by Advanced LIGO. *Astrophysical Journal*, 681:1431–1447, 0705.0285.

[152] Mandel, I. and de Mink, S. E. (2016). Merging binary black holes formed through chemically homogeneous evolution in short-period stellar binaries. *MNRAS*, 458:2634–2647, 1601.00007.

[153] Mandel, I. and Gair, J. R. (2009). Can we Detect Intermediate Mass Ratio Inspirals? *Class. Quant. Grav.*, 26:094036, 0811.0138.

[154] Mandel, I., Haster, C.-J., Dominik, M., and Belczynski, K. (2015). Distinguishing types of compact-object binaries using the gravitational-wave signatures of their mergers. *MNRAS*, 450:L85–L89, 1503.03172.

[155] Mapelli, M. (2016). Massive black hole binaries from runaway collisions: the impact of metallicity. *MNRAS*, 1604.03559.

[156] Mapelli, M., Huwyler, C., Mayer, L., Jetzer, P., and Vecchio, A. (2010). Gravitational Waves from Intermediate-mass Black Holes in Young Clusters. *Astrophysical Journal*, 719:987–995, 1006.1664.

[157] Marchant, P., Langer, N., Podsiadlowski, P., Tauris, T. M., and Moriya, T. J. (2016). A new route towards merging massive black holes. *A&A*, 588:A50, 1601.03718.

[158] Merritt, D. (2013). *Dynamics and Evolution of Galactic Nuclei*.

[159] Merritt, D., Alexander, T., Mikkola, S., and Will, C. M. (2011). Stellar dynamics of extreme-mass-ratio inspirals. *Phys. Rev. D*, 84(4):044024, 1102.3180.

[160] Metropolis, N., Rosenbluth, A. W., Rosenbluth, M. N., Teller, A. H., and Teller, E. (1953). Equation of state calculations by fast computing machines. *J. Chem. Phys.*, 21:1087–1092.

[161] Mikkola, S. and Merritt, D. (2006). Algorithmic regularization with velocity-dependent forces. *MNRAS*, 372:219–223, astro-ph/0605054.

[162] Mikkola, S. and Merritt, D. (2008). Implementing Few-Body Algorithmic Regularization with Post-Newtonian Terms. *Astronomical Journal*, 135:2398–2405, 0709.3367.

[163] Miller, M. C. (2002). Gravitational Radiation from Intermediate-Mass Black Holes. *Astrophysical Journal*, 581:438–450, astro-ph/0206404.

[164] Miller, M. C. (2009). Intermediate-Mass Black Holes as LISA Sources. *Class. Quant. Grav.*, 26:094031, 0812.3028.

[165] Miller, M. C. and Colbert, E. J. M. (2004). Intermediate-Mass Black Holes. *International Journal of Modern Physics D*, 13:1–64, arXiv:astro-ph/0308402.

[166] Miller, M. C. and Hamilton, D. P. (2002). Production of intermediate-mass black holes in globular clusters. *MNRAS*, 330:232–240, arXiv:astro-ph/0106188.

[167] Moore, B., Favata, M., Arun, K. G., and Kant Mishra, C. (2016). Gravitational-wave phasing for low-eccentricity inspiralling compact binaries to 3PN order. *ArXiv e-prints*, 1605.00304.

[168] Moore, C. J., Cole, R. H., and Berry, C. P. L. (2015). Gravitational-wave sensitivity curves. *Class. Quant. Grav.*, 32(1):015014, 1408.0740.

[169] Moore, C. J. and Gair, J. R. (2014). Novel Method for Incorporating Model Uncertainties into Gravitational Wave Parameter Estimates. *Physical Review Letters*, 113(25):251101, 1412.3657.

[170] Morscher, M., Pattabiraman, B., Rodriguez, C., Rasio, F. A., and Umbreit, S. (2015). The Dynamical Evolution of Stellar Black Holes in Globular Clusters. *Astrophysical Journal*, 800:9, 1409.0866.

[171] Morscher, M., Umbreit, S., Farr, W. M., and Rasio, F. A. (2013). Retention of Stellar-mass Black Holes in Globular Clusters. *Astrophysical Journal*, 763:L15, 1211.3372.

[172] Mroué, A. H., Scheel, M. A., Szilágyi, B., Pfeiffer, H. P., Boyle, M., Hemberger, D. A., Kidder, L. E., Lovelace, G., Ossokine, S., Taylor, N. W., Zenginoğlu, A., Buchman, L. T., Chu, T., Foley, E., Giesler, M., Owen, R., and Teukolsky, S. A. (2013). Catalog of 174 Binary Black Hole Simulations for Gravitational Wave Astronomy. *Physical Review Letters*, 111(24):241104, 1304.6077.

[173] Nagar, A., Damour, T., Reisswig, C., and Pollney, D. (2016). Energetics and phasing of nonprecessing spinning coalescing black hole binaries. *Phys. Rev. D*, 93(4):044046, 1506.08457.

[174] Naoz, S., Kocsis, B., Loeb, A., and Yunes, N. (2013). Resonant Post-Newtonian Eccentricity Excitation in Hierarchical Three-body Systems. *Astrophysical Journal*, 773:187, 1206.4316.

[175] Nishizawa, A., Berti, E., Klein, A., and Sesana, A. (2016). eLISA eccentricity measurements as tracers of binary black hole formation. *ArXiv e-prints*, 1605.01341.

[176] Ohme, F. (2012). Analytical meets numerical relativity: status of complete gravitational waveform models for binary black holes. *Classical and Quantum Gravity*, 29(12):124002, 1111.3737.

[177] O'Shaughnessy, R., Farr, B., Ochsner, E., Cho, H.-S., Kim, C., and Lee, C.-H. (2014). Parameter estimation of gravitational waves from nonprecessing black hole-neutron star inspirals with higher harmonics: Comparing markov-chain monte carlo posteriors to an effective fisher matrix. *Phys. Rev. D*, 89:064048.

[178] Owen, B. J. and Sathyaprakash, B. S. (1999). Matched filtering of gravitational waves from inspiraling compact binaries: Computational cost and template placement. *Phys. Rev. D*, 60(2):022002, gr-qc/9808076.

[179] Özel, F., Psaltis, D., Narayan, R., and McClintock, J. E. (2010). The Black Hole Mass Distribution in the Galaxy. *Astrophysical Journal*, 725:1918–1927, 1006.2834.

[180] Pan, Y., Buonanno, A., Taracchini, A., Kidder, L. E., Mroué, A. H., Pfeiffer, H. P., Scheel, M. A., and Szilágyi, B. (2014). Inspiral-merger-ringdown waveforms of spinning, precessing black-hole binaries in the effective-one-body formalism. *Phys. Rev. D*, 89(8):084006, 1307.6232.

[181] Pankow, C., Brady, P., Ochsner, E., and O'Shaughnessy, R. (2015). Novel scheme for rapid parallel parameter estimation of gravitational waves from compact binary coalescences. *Phys. Rev. D*, 92(2):023002, 1502.04370.

[182] Pasham, D. R., Strohmayer, T. E., and Mushotzky, R. F. (2015). A 400 solar mass black hole in the Ultraluminous X-ray source M82 X-1 accreting close to its Eddington limit. *Nat.*, 513(7516):74–76, 1501.03180.

[183] Pasquato, M., Miocchi, P., Sohn, B. W., and Lee, Y.-W. (2016). Globular clusters hosting intermediate-mass black-holes: no mass-segregation based candidates. *ArXiv e-prints*, 1604.03554.

[184] Peters, P. C. (1964). Gravitational Radiation and the Motion of Two Point Masses. *Physical Review*, 136:1224–1232.

[185] Pfahl, E. (2005). Binary Disruption by Massive Black Holes in Globular Clusters. *Astrophysical Journal*, 626:849–852, astro-ph/0501326.

[186] Planck Collaboration, Ade, P. A. R., Aghanim, N., Arnaud, M., Ashdown, M., Aumont, J., Baccigalupi, C., Banday, A. J., Barreiro, R. B., Bartlett, J. G., and et al. (2015). Planck 2015 results. XIII. Cosmological parameters. *ArXiv e-prints*, 1502.01589.

[187] Poisson, E., Pound, A., and Vega, I. (2011). The Motion of point particles in curved spacetime. *Living Rev. Rel.*, 14:7, 1102.0529.

[188] Portegies Zwart, S. F., Baumgardt, H., Hut, P., Makino, J., and McMillan, S. L. W. (2004). The Formation of massive black holes through collision runaway in dense young star clusters. *Nature*, 428:724, astro-ph/0402622.

[189] Portegies Zwart, S. F. and McMillan, S. L. W. (2000). Black hole mergers in the universe. *Astrophysical Journal*, 528:L17.

[190] Porter, E. K. and Sesana, A. (2010). Eccentric Massive Black Hole Binaries in LISA I : The Detection Capabilities of Circular Templates. *ArXiv e-prints*, 1005.5296.

[191] Postnov, K. A. and Yungelson, L. R. (2014). The Evolution of Compact Binary Star Systems. *Living Reviews in Relativity*, 17, 1403.4754.

[192] Pretorius, F. (2005). Evolution of Binary Black-Hole Spacetimes. *Physical Review Letters*, 95(12):121101, gr-qc/0507014.

[193] Pürrer, M. (2014). Frequency domain reduced order models for gravitational waves from aligned-spin compact binaries. *Class. Quant. Grav.*, 31(19):195010, 1402.4146.

[194] Pürrer, M. (2016). Frequency domain reduced order model of aligned-spin effective-one-body waveforms with generic mass ratios and spins. *Phys. Rev. D*, 93(6):064041, 1512.02248.

[195] Pürrer, M., Hannam, M., Ajith, P., and Husa, S. (2013). Testing the validity of the single-spin approximation in inspiral-merger-ringdown waveforms. *Phys. Rev. D*, 88(6):064007, 1306.2320.

[196] Quinlan, G. D. (1996). The dynamical evolution of massive black hole binaries I. Hardening in a fixed stellar background. *New Astronomy*, 1:35–56, arXiv:astro-ph/9601092.

[197] Read, J. S., Baiotti, L., Creighton, J. D. E., Friedman, J. L., Giacomazzo, B., Kyutoku, K., Markakis, C., Rezzolla, L., Shibata, M., and Taniguchi, K. (2013). Matter effects on binary neutron star waveforms. *Phys. Rev. D*, 88(4):044042, 1306.4065.

[198] Rodriguez, C. L., Chatterjee, S., and Rasio, F. A. (2016a). Binary black hole mergers from globular clusters: Masses, merger rates, and the impact of stellar evolution. *Phys. Rev. D*, 93(8):084029, 1602.02444.

[199] Rodriguez, C. L., Farr, B., Farr, W. M., and Mandel, I. (2013). Inadequacies of the Fisher information matrix in gravitational-wave parameter estimation. *Phys. Rev. D*, 88(8):084013, 1308.1397.

[200] Rodriguez, C. L., Haster, C.-J., Chatterjee, S., Kalogera, V., and Rasio, F. A. (2016b). Dynamical Formation of the GW150914 Binary Black Hole. *ArXiv e-prints*, 1604.04254.

[201] Rodriguez, C. L., Mandel, I., and Gair, J. R. (2012). Verifying the no-hair property of massive compact objects with intermediate-mass-ratio inspirals in advanced gravitational-wave detectors. *Phys. Rev. D*, 85:062002, 1112.1404.

[202] Rodriguez, C. L., Morscher, M., Pattabiraman, B., Chatterjee, S., Haster, C.-J., and Rasio, F. A. (2015). Binary Black Hole Mergers from Globular Clusters: Implications for Advanced LIGO. *Phys. Rev. Lett.*, 115(5):051101, 1505.00792v3. Erratum in arXiv:1505.00792v3.

[203] Rodriguez, C. L., Morscher, M., Wang, L., Chatterjee, S., Rasio, F. A., and Spurzem, R. (2016c). Million-Body Star Cluster Simulations: Comparisons between Monte Carlo and Direct N-body. *ArXiv e-prints*, 1601.04227.

[204] Samsing, J., MacLeod, M., and Ramirez-Ruiz, E. (2014). The Formation of Eccentric Compact Binary Inspirals and the Role of Gravitational Wave Emission in Binary-Single Stellar Encounters. *Astrophysical Journal*, 784:71, 1308.2964.

[205] Sana, H., de Mink, S. E., de Koter, A., Langer, N., Evans, C. J., Gieles, M., Gosset, E., Izzard, R. G., Le Bouquin, J.-B., and Schneider, F. R. N. (2012). Binary Interaction Dominates the Evolution of Massive Stars. *Science*, 337:444, 1207.6397.

[206] Santamaria, L. et al. (2010). Matching post-Newtonian and numerical relativity waveforms: systematic errors and a new phenomenological model for non-precessing black hole binaries. *Phys. Rev. D*, 82:064016, 1005.3306.

[207] Sathyaprakash, B. S. and Schutz, B. F. (2009). Physics, Astrophysics and Cosmology with Gravitational Waves. *Living Reviews in Relativity*, 12, 0903.0338.

[208] Schmidt, P., Hannam, M., and Husa, S. (2012). Towards models of gravitational waveforms from generic binaries: A simple approximate mapping between precessing and nonprecessing inspiral signals. *Phys. Rev. D*, 86(10):104063, 1207.3088.

[209] Schmidt, P., Ohme, F., and Hannam, M. (2015). Towards models of gravitational waveforms from generic binaries: II. Modelling precession effects with a single effective precession parameter. *Phys. Rev. D*, 91(2):024043, 1408.1810.

[210] Schutz, B. F. (1984). Gravitational waves on the back of an envelope. *American Journal of Physics*, 52(5):412–419.

[211] Schutz, B. F. (2011). Networks of gravitational wave detectors and three figures of merit. *Class. Quant. Grav.*, 28:125023, 1102.5421.

[212] Sesana, A. (2016). The promise of multi-band gravitational wave astronomy. *ArXiv e-prints*, 1602.06951.

[213] Sesana, A. and Khan, F. M. (2015). Scattering experiments meet N-body - I. A practical recipe for the evolution of massive black hole binaries in stellar environments. *MNRAS*, 454:L66–L70, 1505.02062.

[214] Shoemaker, D. (2010). Advanced ligo anticipated sensitivity curves. LIGO Document LIGO-T0900288-v3.

[215] Sidery, T., Aylott, B., Christensen, N., Farr, B., Farr, W., Feroz, F., Gair, J., Grover, K., Graff, P., Hanna, C., Kalogera, V., Mandel, I., O'Shaughnessy, R., Pitkin, M., Price, L., Raymond, V., Röver, C., Singer, L., van der Sluys, M., Smith, R. J. E., Vecchio, A., Veitch, J., and Vitale, S. (2014). Reconstructing the sky location of gravitational-wave detected compact binary systems: Methodology for testing and comparison. *Phys. Rev. D*, 89(8):084060, 1312.6013.

[216] Singer, L. P. (2015). *The needle in the hundred square degree haystack: The hunt for binary neutron star mergers with LIGO and Palomar Transient Factory*. PhD thesis, California Institute of Technology. http://resolver.caltech.edu/CaltechTHESIS:12102014-223122387.

[217] Singer, L. P. and Price, L. R. (2016). Rapid Bayesian position reconstruction for gravitational-wave transients. *Phys. Rev. D*, 93(2):024013, 1508.03634.

[218] Singer, L. P., Price, L. R., Farr, B., Urban, A. L., Pankow, C., Vitale, S., Veitch, J., Farr, W. M., Hanna, C., Cannon, K., Downes, T., Graff, P., Haster, C.-J., Mandel, I., Sidery, T., and Vecchio, A. (2014). The first two years of

electromagnetic follow-up with advanced ligo and virgo. *The Astrophysical Journal*, 795(2):105.

[219] Skilling, J. and Sivia, D. (2006). Data analysis - a bayesian tutorial - second edition.

[220] Smith, R. J. E., Mandel, I., and Vechhio, A. (2013). Studies of waveform requirements for intermediate mass-ratio coalescence searches with advanced gravitational-wave detectors. *Phys. Rev. D*, 88(4):044010, 1302.6049.

[221] Somiya, K. (2012). Detector configuration of KAGRA the Japanese cryogenic gravitational-wave detector. *Classical and Quantum Gravity*, 29:124007.

[222] Spera, M., Mapelli, M., and Bressan, A. (2015). The mass spectrum of compact remnants from the PARSEC stellar evolution tracks. *MNRAS*, 451:4086–4103, 1505.05201.

[223] Tanay, S., Haney, M., and Gopakumar, A. (2016). Frequency and time-domain inspiral templates for comparable mass compact binaries in eccentric orbits. *Phys. Rev. D*, 93(6):064031, 1602.03081.

[224] Taniguchi, Y., Shioya, Y., Tsuru, T. G., and Ikeuchi, S. (2000). Formation of Intermediate-Mass Black Holes in Circumnuclear Regions of Galaxies. *PASJ*, 52:533–537, arXiv:astro-ph/0002389.

[225] Taracchini, A., Buonanno, A., Pan, Y., Hinderer, T., Boyle, M., Hemberger, D. A., Kidder, L. E., Lovelace, G., Mroué, A. H., Pfeiffer, H. P., Scheel, M. A., Szilágyi, B., Taylor, N. W., and Zenginoglu, A. (2014). Effective-one-body model for black-hole binaries with generic mass ratios and spins. *Phys. Rev. D*, 89(6):061502, 1311.2544.

[226] Taracchini, A., Pan, Y., Buonanno, A., Barausse, E., Boyle, M., Chu, T., Lovelace, G., Pfeiffer, H. P., and Scheel, M. A. (2012). Prototype effective-one-body model for nonprecessing spinning inspiral-merger-ringdown waveforms. *Phys. Rev. D*, 86:024011, 1202.0790.

[227] The LIGO Scientific Collaboration (2014). Advanced LIGO. *ArXiv e-prints*, 1411.4547.

[228] The LIGO Scientific Collaboration (2016). LSC Algorithm Library software packages LAL, LALWRAPPER, and LALAPPS. http://www.lsc-group.phys.uwm.edu/lal.

[229] The LIGO Scientific Collaboration, Martynov, D. V., Hall, E. D., Abbott, B. P., Abbott, R., Abbott, T. D., Abernathy, M. R., Ackley, K., Adams, C., Addesso, P., and et al. (2016a). The Sensitivity of the Advanced LIGO Detectors at the Beginning of Gravitational Wave Astronomy. *ArXiv e-prints*, 1604.00439.

[230] The LIGO Scientific Collaboration and the Virgo Collaboration (2016a). Characterization of transient noise in Advanced LIGO relevant to gravitational wave signal GW150914. *ArXiv e-prints*, 1602.03844.

[231] The LIGO Scientific Collaboration and the Virgo Collaboration (2016b). Observing gravitational-wave transient GW150914 with minimal assumptions. *ArXiv e-prints*, 1602.03843.

[232] The LIGO Scientific Collaboration and the Virgo Collaboration (2016c). Properties of the binary black hole merger GW150914. *ArXiv e-prints*, 1602.03840.

[233] The LIGO Scientific Collaboration and the Virgo Collaboration (2016d). Tests of general relativity with GW150914. *ArXiv e-prints*, 1602.03841.

[234] The LIGO Scientific Collaboration, the Virgo Collaboration, Abbott, B. P., Abbott, R., Abbott, T. D., Abernathy, M. R., Acernese, F., Ackley, K., Adams, C., Adams, T., and et al. (2016b). GW150914: First results from the search for binary black hole coalescence with Advanced LIGO. *ArXiv e-prints*, 1602.03839.

[235] The SXS Collaboration (2016). The SXS catalogue of numerical relativity waveforms. http://www.black-holes.org/waveforms.

[236] Tiwari, V., Klimenko, S., Christensen, N., Huerta, E. A., Mohapatra, S. R. P., Gopakumar, A., Haney, M., Ajith, P., McWilliams, S. T., Vedovato, G., Drago, M., Salemi, F., Prodi, G. A., Lazzaro, C., Tiwari, S., Mitselmakher, G., and Da Silva, F. (2016). Proposed search for the detection of gravitational waves from eccentric binary black holes. *Phys. Rev. D*, 93(4):043007, 1511.09240.

[237] Trenti, M. (2006). Dynamical evidence for intermediate mass black holes in old globular clusters. *ArXiv Astrophysics e-prints*, arXiv:astro-ph/0612040. arXiv:astro-ph/0612040.

[238] Trenti, M., Ardi, E., Mineshige, S., and Hut, P. (2007a). Star clusters with primordial binaries - III. Dynamical interaction between binaries and an intermediate-mass black hole. *MNRAS*, 374:857–866, astro-ph/0610342.

[239] Trenti, M., Heggie, D. C., and Hut, P. (2007b). Star clusters with primordial binaries - II. Dynamical evolution of models in a tidal field. *MNRAS*, 374:344–356, astro-ph/0602409.

[240] Umbreit, S. and Rasio, F. A. (2013). Constraining Intermediate-mass Black Holes in Globular Clusters. *Astrophysical Journal*, 768:26, 1207.2497.

[241] Vallisneri, M. (2008). Use and abuse of the Fisher information matrix in the assessment of gravitational-wave parameter-estimation prospects. *Phys. Rev. D*, 77:042001, gr-qc/0703086.

[242] van der Sluys, M., Raymond, V., Mandel, I., Röver, C., Christensen, N., Kalogera, V., Meyer, R., and Vecchio, A. (2008a). Parameter estimation of spinning binary inspirals using Markov chain Monte Carlo. *Classical and Quantum Gravity*, 25(18):184011, 0805.1689.

[243] van der Sluys, M. V., Röver, C., Stroeer, A., Raymond, V., Mandel, I., Christensen, N., Kalogera, V., Meyer, R., and Vecchio, A. (2008b). Gravitational-Wave Astronomy with Inspiral Signals of Spinning Compact-Object Binaries. *The Astrophysical Journal Lettersl*, 688:L61–L64, 0710.1897.

[244] Vanbeveren, D. (2009). The evolution of massive and very massive stars in clusters. *New Astronomy Reviews*, 53:27–35, 0810.4781.

[245] Veitch, J. and del Pozzo, W. (2013). Analytic marginalisation of phase parameter. Technical Report LIGO-T1300326.

[246] Veitch, J., Pürrer, M., and Mandel, I. (2015a). Measuring intermediate mass black hole binaries with advanced gravitational wave detectors. *Phys. Rev. Lett.*, 115(14):141101, 1503.05953.

[247] Veitch, J., Raymond, V., Farr, B., Farr, W., Graff, P., Vitale, S., Aylott, B., Blackburn, K., Christensen, N., Coughlin, M., Del Pozzo, W., Feroz, F., Gair, J., Haster, C.-J., Kalogera, V., Littenberg, T., Mandel, I., O'Shaughnessy, R., Pitkin, M., Rodriguez, C., Röver, C., Sidery, T., Smith, R., Van Der Sluys, M., Vecchio, A., Vousden, W., and Wade, L. (2015b). Parameter estimation for compact binaries with ground-based gravitational-wave observations using the lalinference software library. *Phys. Rev. D*, 91:042003.

[248] Veitch, J. and Vecchio, A. (2010). Bayesian coherent analysis of in-spiral gravitational wave signals with a detector network. *Phys. Rev. D*, 81(6):062003, 0911.3820.

[249] Vitale, S. (2016). Multi-band gravitational-wave astronomy: parameter estimation and tests of general relativity with space and ground-based detectors. *ArXiv e-prints*, 1605.01037.

[250] Vousden, W. D., Farr, W. M., and Mandel, I. (2016). Dynamic temperature selection for parallel tempering in Markov chain Monte Carlo simulations. *MNRAS*, 455:1919–1937, 1501.05823.

[251] Weisberg, J. M. and Taylor, J. H. (2005). The Relativistic Binary Pulsar B1913+16: Thirty Years of Observations and Analysis. In Rasio, F. A. and Stairs, I. H., editors, *Binary Radio Pulsars*, volume 328 of *Astronomical Society of the Pacific Conference Series*, page 25. astro-ph/0407149.

[252] Wen, L. (2003). On the Eccentricity Distribution of Coalescing Black Hole Binaries Driven by the Kozai Mechanism in Globular Clusters. *Astrophysical Journal*, 598:419–430, arXiv:astro-ph/0211492.

[253] Will, C. M. (2006). The Confrontation between General Relativity and Experiment. *Living Reviews in Relativity*, 9, gr-qc/0510072.